Phase behaviour and ordering in hard core lattice gas models

By

Trisha Nath

PHYS10201104002

The Institute of Mathematical Sciences, Chennai

A thesis submitted to the

Board of Studies in Physical Sciences

In partial fulfillment of requirements

for the Degree of

DOCTOR OF PHILOSOPHY

of

HOMI BHABHA NATIONAL INSTITUTE

June, 2016

Homi Bhabha National Institute

Recommendations of the Viva Voce Board

As members of the Viva Voce Board, we certify that we have read the dissertation prepared by Trisha Nath entitled “Phase behaviour and ordering in hard core lattice gas models" and recommend that it maybe accepted as fulfilling the dissertation requirement for the Degree of Doctor of Philosophy.

_____ Date:

Chair - Purusattam Ray

_____ Date:

Guide/Convener - Rajesh Ravindran

_____ Date:

Member 1 - Sanatan Digal

_____ Date:

Member 2 - Gautam I. Menon

_____ Date:

External Examiner - Sanjib Sabhapandit

Final approval and acceptance of this dissertation is contingent upon the candidate’s submission of the final copies of the dissertation to HBNI.

I hereby certify that I have read this dissertation prepared under my direction and recommend that it may be accepted as fulfilling the dissertation requirement.

Date:

Place: Guide

STATEMENT BY AUTHOR

This dissertation has been submitted in partial fulfillment of requirements for an advanced degree at Homi Bhabha National Institute (HBNI) and is deposited in the Library to be made available to borrowers under rules of the HBNI.

Brief quotations from this dissertation are allowable without special permission, provided that accurate acknowledgement of source is made. Requests for permission for extended quotation from or reproduction of this manuscript in whole or in part may be granted by the Competent Authority of HBNI when in his or her judgement the proposed use of the material is in the interests of scholarship. In all other instances, however, permission must be obtained from the author.

Trisha Nath

DECLARATION

I, hereby declare that the investigation presented in the thesis has been carried out by me. The work is original and has not been submitted earlier as a whole or in part for a degree / diploma at this or any other Institution / University.

Trisha Nath

List of publications arising from the thesis

- **Journal**

1. **The high density phase of the k-NN hard core lattice gas model**

   Trisha Nath and R. Rajesh

   J. Stat. Mech. **2016**, *7*, 073203

2. **Stability of columnar order in assemblies of hard rectangles or squares**

   Trisha Nath, Deepak Dhar and R. Rajesh

   Europhys. Lett. **2016**, *114*, 10003

3. **High-activity expansion for the columnar phase of the hard rectangle gas**

   Trisha Nath, Joyjit Kundu and R. Rajesh

   J. Stat. Phys. **2015**, *160*, 1173

4. **Multiple phase transitions in extended hard-core lattice gas models in two dimensions**

   Trisha Nath and R. Rajesh

   Phys. Rev. E, **2014**, *90*, 012120

List of conferences attended

1. **APS March Meeting**, Baltimore, Maryland, USA, March, 2016
2. **Indian Statistical Physics Community Meeting**, IISc, Bangalore, India, February, 2015
3. **STATPHYS-Kolkata VIII**, SNBNCBS, Kolkata, India, November, 2014
4. **Indian Statistical Physics Community Meeting**, IISc, Bangalore, India, February, 2014
5. **Diversity & Complexity: Realm of Today's Statistical Physics**, SINP, Kolkata, India, January, 2013
6. **Bayes by the Bay - A Pedagogical Workshop on Bayesian Methods in Science**, Pondicherry, India, January, 2013
7. **Fracture & Flow in Porous Media**, IMSc, Chennai, India, January, 2012

ACKNOWLEDGEMENTS

First I would like to thank my supervisor Prof. R. Rajesh for his continuous support, guidance and encouragement over the last five years. I thank him for being approachable with any confusion or the utmost trivial questions. His innovative ideas and innumerable suggestions have helped me build up the thesis. It has been a real pleasure learning Statistical Mechanics and working with him.

I would like to thank my collaborators Prof. Deepak Dhar, Joyjit Kundu and Dipanjan Mandal. Prof. Deepak Dhar has provided indispensable advice and valuable comments during my doctoral research. I would also like to thank my doctoral committee members Prof. Gautam Menon, Prof. Purusattam Ray and Prof. Sanatan Digal for insightful discussions. Special thanks to Prof. Gautam Menon for giving me the opportunity to discuss with him on many occasions. I also thank Prof. Satyavani Vemparala and Dr. Pinaki Chaudhuri for their occasional help.

I would like to thank members of IMSc administration, especially Vasan, Gopi, Jahir, Prema, R Indra and Vishnu Prasad for providing a peaceful research-friendly environment at IMSc. I would like to thank IMSc for the High-Performance computing facilities and library. Most of the numerical simulations in this thesis have been carried out on the supercomputing machines Annapurna and Nandadevi, and other clusters.

I thank my friends Abhra, Sunando, Bose, Chandrasekhar and Sima for all the fun times we have shared which are almost always closely related to food. I would like to thank my parents, brother and sister-in-law for their constant support and faith in me.

Lastly, I would like to thank Jahanur and my office (F-6) members – Anish, Aritra, Shilpa, and my husband Upayan. Life at IMSc would not have been so much fun without all the gossips, messy desks, occasional trips, debates and discussions. To Upayan, I would like to thank for always having confidence in me.

Abstract

Systems of particles that interact only through excluded volume interactions are minimal models to study entropy-driven phase transitions. In this thesis we study in detail two hard core lattice gas models on the square lattice, (1) The k-NN model which is the discrete version of the hard disc system in two dimensions and (2) hard rectangles and squares.

In the k-NN model the first k nearest neighboring lattice points of a particle are excluded from being occupied by another particle. In the 4-NN model, using Monte Carlo simulations we find the existence of two continuous transitions with increasing density – the first from disordered to sublattice-ordered phase and the second from sublattice-ordered to columnar-ordered phase. We further analytically rationalize the existence of multiple transitions by high-activity series expansion. Extending the argument, we conjecture that if the model satisfies (i) the high density phase is columnar and (ii) sliding instability is present in only a fraction of the sublattices, then the system will show multiple transitions. We verify the same in k-NN models with k=6, 7, 8, 9, 10, 11 using Monte Carlo simulations. The conjecture reduces to determining, for a given k greater than 5, whether the high density phase has columnar order at close packing. Finding out close packing structure for k-NN with k up to 820302, we show that there are only eighteen values of k, all less than $k = 4134$, that show columnar order, while the others show sublattice order.

We further analytically study the columnar phase in classical hard-square lattice gas and mxd hard rectangles on square lattice. By deriving the exact expression for the first d + 2 terms in the free energy expansion, we obtain lower bounds for the critical density and activity for nematic-columnar transition. To obtain a better estimate of the critical parameters, we estimate the interfacial tension between two phases with different columnar order in a system of 2xd hard rectangles. Setting the interfacial tension to zero, we obtain a condition for the limit of stability of the columnar ordered phase. For all values of d, the critical parameters obtained are in good agreement with numerical data.

Contents

Synopsis

Entropy being a measure of disorder, a disordered state often has more entropy than an ordered state. A phase transition to such an ordered phase is driven by a gain in energy that outweighs the loss in entropy. Examples include the paramagnetic-ferromagnetic and gas-liquid transitions. However, there are many systems where the ordered state has counter-intuitively larger entropy than the disordered state with no significant difference in internal energy. Such transitions are driven by a gain in entropy and are called entropy driven transitions. Examples of such transitions include the liquid-solid freezing transition in athermal systems [1, 2], isotropic-nematic transition in liquid crystals [3] and ordering transitions in adsorbed monolayers of gas particles on metal surfaces [4].

Systems of particles that interact only through excluded volume interactions are minimal models to study entropy-driven phase transitions [5]. Though simple, these hard core models can reproduce the phases and phase transitions in more complex systems with additional interactions. For example, a system of long thin cylinders is able to reproduce the isotropic-nematic transition in liquid crystals which has additional interactions [6]. Likewise the discontinuous fluid-crystal phase transition experimentally observed in suspension of colloidal polymethyl methacrylate may be reproduced by the hard sphere system in continuum [2]. Phase diagram of adsorbed gas particles on metal surfaces may be explained by models of hard core particles of different shapes on lattices [4].

Though extensively studied, the dependence of the phase diagram and the nature of the phases observed in such entropy driven transitions on the shape of the particles is not very clear. Despite sustained interest, there are only very few exactly solvable models. Only known solutions are for the hard hexagon on triangular lattice and related models [7, 8] and a special limiting case of thin long cylinders in three dimensional continuum [6]. Thus, it is important to study differently shaped particles to see whether a pattern may be deciphered. In this thesis we study in detail two hard core lattice gas (HCLG) models

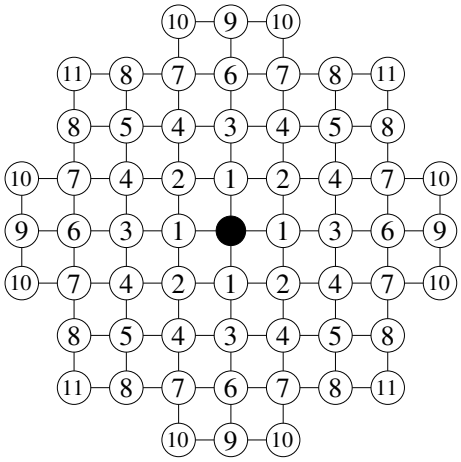

Figure 1: The lattices sites that are excluded by a particle (black filled circle) in the k-NN model. The labels denote the sites that are the k^{th} next nearest neighbors. For k-NN HCLG, all sites with labels less than or equal to k are excluded from being occupied by another particle.

on the square lattice. (1) The k-NN model which is the discrete version of the hard disc system in two dimensions and (2) hard rectangles and squares.

k-NN model: The k-NN HCLG is the lattice version of the hard-sphere problem [2] in the continuum, where larger k corresponds to smaller lattice spacing. In the k-NN model the first k nearest neighboring lattice points of a particle are excluded from being occupied by another particle. In Fig. 1, the sites excluded by a particle are shown for $k = 1, 2, \ldots, 11$. For a given k, all sites with labels less than or equal to k are excluded.

Known results: The k-NN model for $k \leq 5$ is known to exhibit only one transition with increasing density [9]. The 1-NN model undergoes a continuous phase transition of the Ising universality class from a low density disordered phase to a high density sublattice ordered phase [10, 11]. The high density ordered phase of the 2-NN (2×2 hard square) model is columnar. The columnar phase has translational order along either rows or columns but not along both. Monte Carlo simulations show that the disorder–columnar transition in the 2-NN model is continuous and belongs to the two color Ashkin Teller universality class [12, 13]. For higher values of k, the number of symmetric high density ordered states are 10 (3-NN), 8 (4-NN) and 6 (5-NN). By analogy with the q-state Potts model, it is expected that the transitions to an ordered state in these models are first order.

Indeed, all evidence shows that the 3-NN model undergoes a first order phase transition from a low density disordered phase into a sublattice phase with increasing density [9,11]. The 5-NN model is equivalent to the 3×3 hard square problem and the high density phase is columnar as in the 2-NN model [9, 14]. The transition in the 5-NN model has been numerically shown to be first order [9]. However, Monte Carlo simulations of the 4-NN model find a continuous disorder-sublattice transition belonging to the Ising Universality class [9]. Although, an analysis based on cluster integrals excludes the possibility of the transition belonging to the Ising universality class [15]. Not much is known for $k \geq 6$. It becomes increasingly difficult to equilibrate systems with large k in Monte Carlo simulations that use only local evaporation, deposition and diffusion moves as at high densities, the system tends to get stuck in long-lived metastable states.

Results: We implement an efficient Monte Carlo algorithm allowing us to equilibrate and study the k-NN model for $k \geq 4$. We first resolve the ambiguity about the phase diagram of the 4-NN model. Using large scale Monte Carlo simulations we find the existence of two continuous transitions with increasing density of particles – the first from low-density disordered to sublattice-ordered phase and the second from sublattice-ordered to columnar-ordered phase.

In Fig. 2, we show typical snapshots of the equilibrated system at low, intermediate and high densities. Each lattice site belongs to a diagonal oriented in the $\pi/4$ direction and to a diagonal oriented in the $3\pi/4$ direction. All sites that belong to a diagonal with orientation $\pi/4$ are assigned a label from 0 to 3. Similarly, all sites that belong to a diagonal with orientation $3\pi/4$ are assigned a label from 4 to 7 [see Fig. 2(a)]. In the left panels of Fig. 2(b)-(d), all particles belonging to sublattice i ($i = 0, 1, 2, 3$) have the same color. Similarly, in the right panels, all particles belonging to sublattice i ($i = 4, 5, 6, 7$) have the same color. At low densities [see Fig. 2(b)], all four colors are present (roughly equal) in both the left and right panels. This is the disordered phase. At intermediate densities [see Fig. 2(c)], we find that majority of particles preferably occupy either the even sublat-

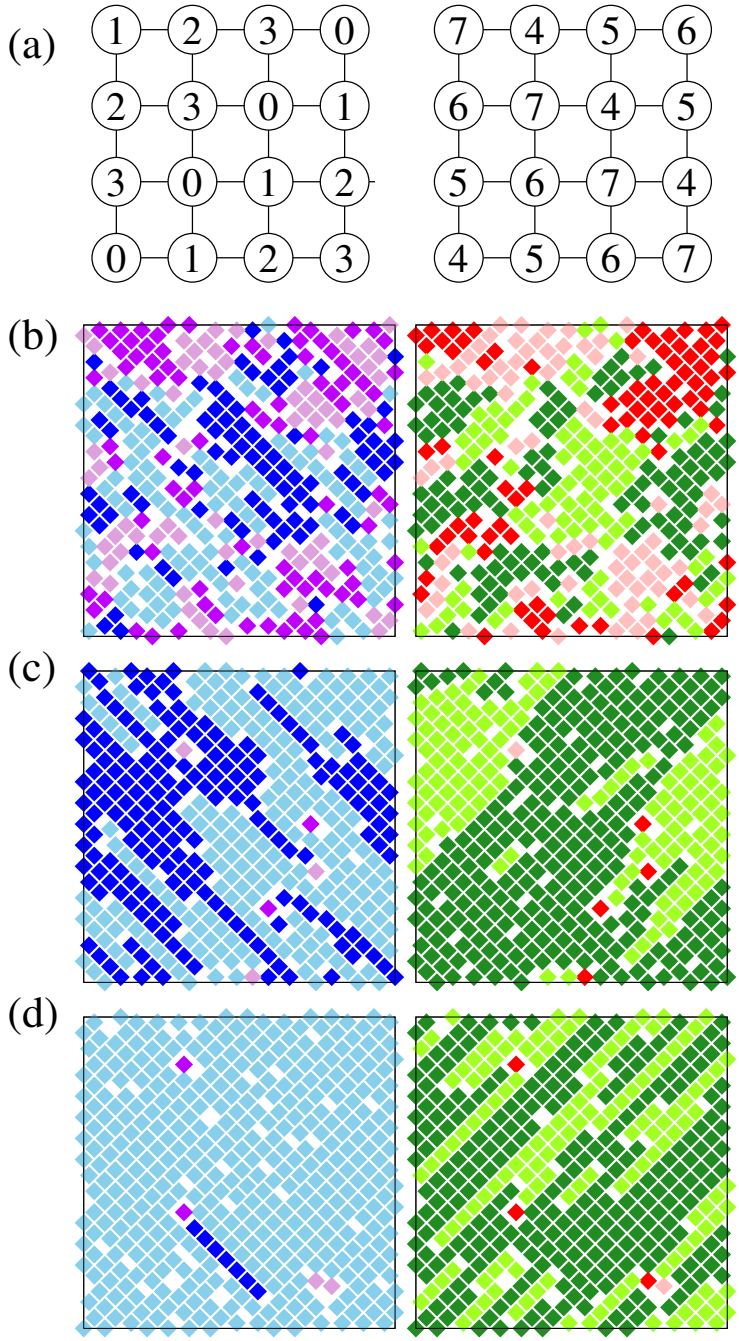

Figure 2: Snapshots of typical configurations of the 4-NN model. (a) All sites belonging to a diagonal oriented in the $\pi/4$ direction have same label. If the site has coordinates (x, y), then the label is $[(x - y) \mod 4]$. All sites belonging to a diagonal oriented in the $3\pi/4$ direction have same label. If the site has coordinates (x, y), then the label is $[(x + y) \mod 4 + 4]$. (b)-(d) The particles are colored according to the sublattice it belongs to. In the left panel, the colors are light blue for 0, dark magenta for 1, deep blue for 2 and plum for 3. In the right panel, the colors are dark green for 4, red for 5, light green for 6 and pink for 7. (b) Low density disordered phase where all four colors are present in both panels. (c) Intermediate density sublattice phase, where even or odd sublattices are preferentially occupied. (d) High density columnar phase, where one sublattice in one of the panels (left in figure) and two sublattices in the other panel are preferentially occupied.

tices or the odd sublattices. We call this phase a sublattice phase. At high densities [see Fig. 2(d)], we find that the particles occupy one of the four sublattices from 0–3 or 4–7, but not from both. In the example shown in Fig. 2(d), in the left panel, particles preferentially occupy sublattice 0. However, in the right panel, particles occupy mostly two sublattices (4 and 6). This phase is identical to the high density phase of the hard square model (2-NN) where there is positional order in one direction but no positional order in the perpendicular direction due to a sliding instability. We call this phase the columnar phase. There are 8 such states, corresponding to the number of sublattices. From finite size scaling analysis near critical point, we establish that the first transition belongs to Ising class and the second to Ashkin-Teller universality class.

We further analytically rationalize the existence of the intermediate sublattice-ordered phase by high-activity series expansion about a perfectly columnar state in terms of rod-like defects. We show that the high density phase (say all particles in mostly sublattice 0) has a sliding instability only for defects in sublattice 2 and not for defects in sublattices 1 and 3. This results in the densities of defects in the different sublattices being different at large z. We argue that this sliding instability could be the origin of the two phase transitions in the 4-NN model. The presence of two transitions resolves the existing puzzle as to why the system had a continuous transition when analogy with the Potts model predicts a first order transition. We show that the eight-fold symmetry is broken in two steps leading to two continuous transitions rather than a single first order transition.

Hard discs in two dimensions are known to undergo two phase transitions with increasing density: first from liquid to hexatic and second from hexatic to solid [16]. However, the k-NN model has been known to show only phase transition [9]. We showed that the 4-NN model undergoes two transitions raising the possibility that for larger k, multiple transitions may be possible in the k-NN model. Extending the argument for the existence of an intermediate sublattice-ordered phase obtained in the 4-NN model, we conjecture that if the model satisfies (i) the high density phase is columnar and (ii) the sliding instability

Table 1: The nature of the ordered phases and the transitions for $k \leq 11$. More than one entry for a given value of k indicates that multiple transitions occur with increasing density with the phases appearing in the order it is listed. Question marks denote that the result is not known.

k	Ordered phases	Nature of transition
1	Sublattice	Continuous (Ising)
2	Columnar	Continuous (Ashkin-Teller)
3	Sublattice	Discontinuous
4	Sublattice	Continuous (Ising)
	Columnar	Continuous (Ashkin-Teller)
5	Columnar	Discontinuous
6	Sublattice	Discontinuous
7	Sublattice	Discontinuous
8	Sublattice	Discontinuous
9	Sublattice	Discontinuous
10	Sublattice	Continuous (Ising)
	Columnar	Discontinuous
11	?	?
	Columnar	?

is present in only a fraction of the sublattices, then the system will show multiple transitions. Applying this conjecture for $k > 5$, we claim that $k = 10, 11, 14, \ldots$ should have multiple transitions and $k = 6, 7, 8, 9, \ldots$ should have single phase transition. We verify the same in k-NN models with $6 \leq k \leq 11$ using Monte Carlo simulations. We find single first-order transitions for $k = 6, 7, 8, 9$ and multiple transitions for $k = 10, 11$. The results for $k \leq 11$ are summarized in Table. 1.

The conjecture reduces to determining for a given $k > 5$ whether the high density phase has columnar order. This may be determined by examining the fully-packed phase. We implement a simple algorithm to find out close packing structure for each k-NN and determine the nature of the phase at full packing for k up to 820302. We show that there are only eighteen values of k, all less than $k = 4134$, that show columnar order, while the others show solid-like sublattice order.

Hard rectangles: In our study of the k-NN model it is observed that understanding the columnar phase is crucial to determine whether multiple transitions are present. However, our understanding of columnar ordering is not very satisfactory. For instance, while

there exists rigorous proof for the existence of the solid-like sublattice [17] and nematic phases [18], there is no corresponding result for columnar order. We thus study the prototypical models that show columnar order – classical 2×2 (also the 2-NN model) hard-square lattice gas [11, 19] and hard rectangles on square lattice [20, 21].

Systems of hard rectangles with two orientations on square lattice have rich phase diagrams which depend only on the width and aspect ratio of the rectangles. Consider a mono-dispersed system of hard rectangles of size $m \times d$ ($d \geq m$) on a square lattice, where $k = d/m$ is the aspect ratio, and each rectangle may orient along one of two directions – horizontal or vertical. No two rectangles may overlap.

Known results: When $m \geq 2$ and $k \geq 7$, the system undergoes three density-driven transitions: first an isotropic-nematic (I-N) transition, second a nematic-columnar (N-C) transition, and third a columnar-sublattice (C-S) transition [20, 21]. Here, the columnar phase breaks translational symmetry in the direction perpendicular to the nematic orientation and the sublattice phase, unlike the columnar phase, breaks translational symmetry in both directions.

For large d, the threshold density for the I-N transition ρ_1^* tends to 0 [21], and the critical density for the C-S transition ρ_3^* tends to 1 [20]. Interestingly, simulations have shown that the critical density for the N-C transition ρ_2^* tends to a non-trivial finite value ≈ 0.73, as $d \to \infty$ [21], and $\rho_2^* \approx 0.93$ for $d = 2$ [9, 12, 13, 19]. From Monte Carlo simulations $\rho_c(2) \approx 0.932$, and $z_c(2) \approx 97.5$ [9, 12, 13, 19], while $\rho_c(d) \approx 0.73 + 0.46d^{-1} + O(d^{-2})$, $z_c(d) \approx 71.0d^{-1} + O(d^{-2})$ [21]. The results obtained by different analytical methods differ considerably from the numerically obtained values and are summarized in Table 2.

Results: We study the N-C transition by developing a high-activity expansion in integer powers of $z^{-1/d}$ for the columnar phase in a model where the rectangles are allowed to orient only in one direction. We generalize the calculations of the hard square gas in Ref. [19] to derive the high-activity expansion. We derive the exact expression of the free

Table 2: The estimates for the critical fugacity $z_c(d)$ and critical density $\rho_c(d)$ obtained for nematic-columnar phase transition in a system of $2 \times d$ rectangles from different approaches. The results for $z_c(d)$ are for $d \gg 1$.

$z_c(2)$	$\rho_c(2)$	Method
97.50	0.932	Numerical [9, 12, 13]
6.25	0.64	High density expansion (order one) [11, 19]
14.86	0.754	High density expansion (order two) [19]
135.9	-	Antiferromagnetic Ising model [22]
11.09	0.76	Fundamental measure theory [23, 24]
11.09	0.76	Approximate counting [25]
17.22	0.80	Cluster variational method [11]
11.09	0.76	Flory-type mean field [26]
48.25	0.928	Zero defect (result in this thesis)
52.49	0.923	One defect (result in this thesis)
54.87	0.9326	Overhang (result in this thesis)
$z_c(d)$	$\rho_c(d)$	Method
$\frac{71.0}{d}$	$0.73 + \frac{0.46}{d}$	Numerical [21]
$\frac{5.56}{d}$	$0.357 + \frac{0.73}{d}$	High density expansion (order d+2) (result in this thesis)
-	$0.59 + \frac{0.29}{d}$	Bethe approximation [20]
$\frac{60.26}{d}$	$0.75 + \frac{0.375}{d}$	Zero defect (result in this thesis)
$\frac{65.23}{d}$	$0.746 + \frac{0.374}{d}$	One defect (result in this thesis)
$\frac{67.78}{d}$	$0.755 + \frac{0.382}{d}$	Overhang (result in this thesis)

energy density $f(z)$ for the first $d + 2$ terms in the expansion,

$$-f(z) = \frac{\ln z}{dm} + \frac{z^{-1/d}}{dm} + \sum_{n=2}^{d+1} \frac{z^{-n/d}}{n! d^n m} \prod_{j=1}^{n-1} (jd - n) + \frac{z^{-1}}{md} (\kappa - 1)$$
$$+ \frac{z^{-1-1/d}}{md^2} \left[1 + 2d - \frac{\kappa \left(2d^2 - 2dm + d + m - 2 \right)}{d - 1} + 24\delta_{d,2} \ln \frac{9}{8} \right] + O(z^{-1-2/d}). \quad (1)$$

The expansion is not in terms of single defects, but in terms of clusters of defects. From the high-activity expansions for the densities of rectangles with heads on rows of different labels, truncated at $O(z^{-1-1/d})$, we estimate the transition points z_c and ρ_c. We find that $z_c \approx ck^{-1}$ [see Fig. 3(a)] , $\rho_c(m, k) \approx \rho_c(m, \infty) + b_1 k^{-1}$ [see Fig. 3(b)] for $k \gg 1$, where $c > 0$, and $b_1 > 0$, are m-independent constants, and $\rho_c(m, \infty)$ tends to a constant for large m with deviations decreasing as some inverse power of $\ln m$. For hard squares with $d = m$, or equivalently $k = 1$, we obtain that the critical density increases logarithmically to a constant when $m \gg 1$. However, we find that the estimates for the critical parameters

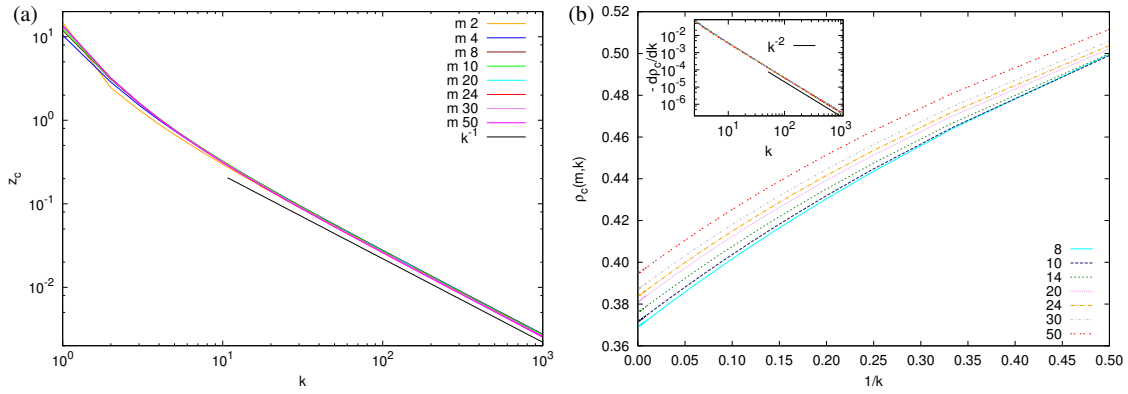

Figure 3: Variation of (a) z_c and (b) $\rho_c(m,k)$ with k for different m obtained from high-activity expansion in a system of $m \times d$ rectangles. Inset: The data for $d\rho_c/dk$ for different m collapse onto a single curve, independent of m.

differ from the numerically obtained values – z_c by a factor of 14 and ρ_c by 2 [see Table 2].

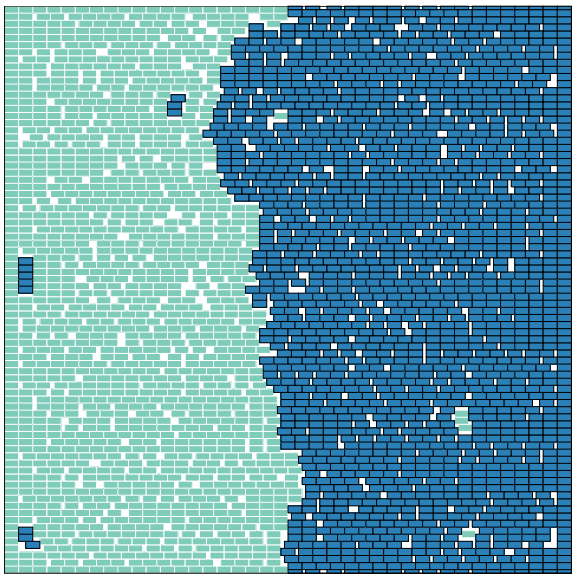

Figure 4: Snapshot of a typical configuration of 2×4 rectangles where the left (right) phase is constrained to be even (odd) by fixing the rectangles at the boundary. Even (odd) rectangles are shown in teal (blue). The system size is 160×160.

To obtain a better estimate of the critical parameters, we estimate the interfacial tension between two phases with different columnar order in a system of $2 \times d$ hard rectangles on square lattice. Setting the interfacial tension to zero, we obtain a condition for the limit of stability of the columnar ordered phase. To compute interfacial tension, we impose an interface by fixing the rectangles at the left (right) boundary to be even (odd). A typical

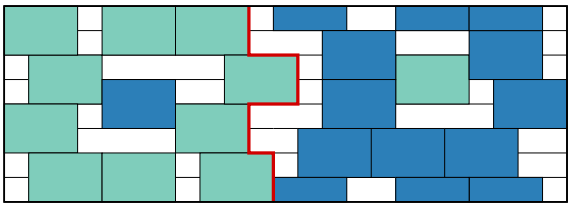

Figure 5: A schematic diagram of the interface (thick red line) between two phases having a defect each. Even (odd) rectangles are shown in teal (blue).

configuration seen in a simulation of 2×4 rectangles is shown in Fig 4. In the simplest approximation, we ignore overhangs such that the interface is a path from top to bottom with no upward steps allowed [see Fig 5].

We have done our calculation in two different approximations. In the first, we work out the high-density expansion for the interfacial tension as a perturbation series in the defect density, and estimate the critical point by truncating this expansion at first order. The formal power series in powers of defect density is a singular perturbation series in the activity z.

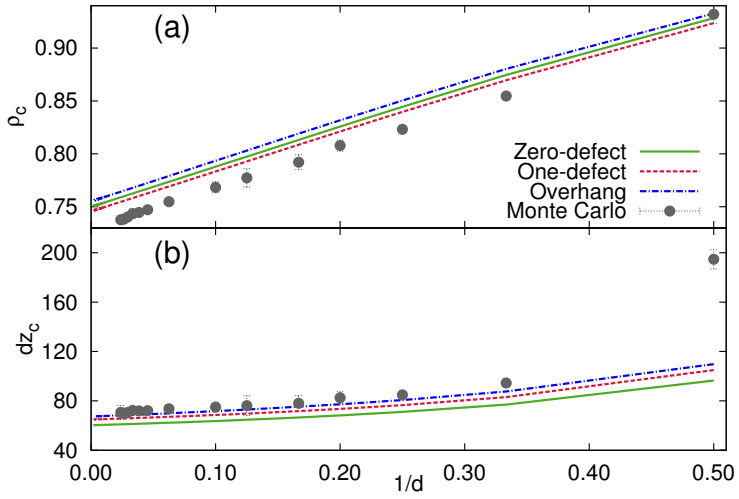

Figure 6: The results obtained from calculation of interfacial tension for (a) critical density ρ_c and (b) critical activity z_c for the disordered-columnar transition with zero defect (green line), one defect (red line) and overhangs (blue line) are compared with the results from Monte Carlo simulations (data points). The data for $d = 2$ is from Refs. [9, 12, 13].

At the zeroth order in defect density, it is straightforward to determine the partition function per site in the bulk, and the interface is a partially directed self-avoiding walk. Summing over the different configurations of the walk gives us the zeroth order estimates of $z_c(d)$ and $\rho_c(d)$,

$$z_c^*(d) = \left(\frac{1 + \sqrt{1 - d + d^2}}{d - 1}\right)^{2d} - \left(\frac{1 + \sqrt{1 - d + d^2}}{d - 1}\right)^{2(d-1)}, \tag{2}$$

$$\rho_c^*(d) = \frac{d(1 + d + 2\sqrt{1 - d + d^2})}{(d + \sqrt{1 - d + d^2})^2}. \tag{3}$$

We then calculate the first order correction to this result due to the presence of defects in the bulk phases. In the second method, we ignore defects in the bulk, but take into account a subset of configurations of the interface with overhangs to improve the estimate of the interfacial tension. For all values of d, the estimates of ρ_2^* show good agreement with Monte Carlo data and are a significant improvement over earlier methods [see Table 2]. The results for hard squares and those for general d are compared with the Monte Carlo results in Fig. 6.

List of Figures

List of Tables

Chapter 1

Introduction

Phase transitions are abrupt changes in the thermodynamic properties of a system as control parameters are tuned across a phase boundary. The two phases across the boundary often have different symmetries and order. A common example of phase transition is the freezing transition from liquid to solid where the solid has positional order in which the continuous translational symmetry of the liquid is broken. Other well studied examples of phase transitions include the ferromagnetic-paramagnetic transition in magnets and liquid-gas transition.

Phase transitions may be discontinuous or continuous. Discontinuous or first-order phase transitions involve a non-zero latent heat. The order parameter, a quantity that captures the order of the system, has a discontinuity corresponding to a discontinuity in the first derivative of the free energy with respect to the external field. An example is the solid-liquid transition where density, the first derivative of the free energy with respect to pressure, has a jump across the transition. Correlation length remains finite at the transition point. On the other hand, continuous transitions are characterized by an infinite correlation length and long-ranged power law correlations leading to diverging response functions near critical point. The ferromagnetic to paramagnetic transition is an example of such transition. Divergence of correlation length and other thermodynamic quantities such as compress-

ibility, susceptibility etc near criticality are characterized by critical exponents. Near criticality, different systems with different microscopic behavior have same critical exponents. This phenomenon is known as universality. Universality and continuous transitions are now well-understood within the scope of the renormalization group.

1.1 Entropy driven phase transitions

In a system at constant temperature and constant volume, phase transitions from a disordered to an ordered phase occur when the ordered phase has a lower free energy than the disordered one. The free energy F of a system is defined as $F = U - TS$, where U is the internal energy and S is the entropy. Intuitively, an ordered state is expected to have less entropy than a disordered state, as entropy may be interpreted as a measure of disorder in a system. In such cases, a transition to an ordered state can occur only if the internal energy of the system is lowered enough to outweigh the loss in entropy. Such transitions are energy-driven transitions. Examples are the the ferromagnetic-paramagnetic and liquid-gas phase transitions. However, there are many systems where the ordered state has counter-intuitively larger entropy than the disordered state with no significant difference in internal energy. Such transitions are driven by a gain in entropy and are called entropy driven transitions [27]. Examples of such transitions include the liquid-solid freezing transition in athermal systems [1, 2], isotropic-nematic transition in liquid crystals [3], ordered structures in adsorbed monolayers of gas particles on metal surfaces [4, 28], polymer induced attraction in colloidal particles [29] and phase separation in binary mixtures due to depletion interactions [30].

1.1.1 Hard core exclusion models

Systems of particles that interact only through excluded volume interactions are minimal models to study entropy-driven phase transitions [5, 27]. In such models, density

and shape of the particles are the only control parameters. Temperature plays no role as the energy of all allowed configurations are equal. Thus all transitions, if any, must be entropy-driven. Though simple, these hard core models can reproduce the phases and phase transitions in more complex systems with additional interactions. For example, the isotropic nematic transition seen in a system of long thin cylinders, as demonstrated first by Onsager [6], is able to reproduce the isotropic-nematic transition in liquid crystals which has additional interactions. Likewise the discontinuous fluid-crystal phase transition experimentally observed in suspension of colloidal polymethyl methacrylate may be reproduced by the hard sphere in continuum [2, 31]. Phase diagram of adsorbed gas particles on metal surfaces may be explained by models of hard core particles of different shapes on lattices [4, 28, 32–37]. The phase diagram of Brownian square or rectangular platelets may be obtained with hard corner-rounded squares and rectangles [38–41].

Studying phase behaviour of systems of hard particles of different shapes has attained great interest recently. Complete phase diagram of the system of hard sphero-cylinders in three dimensions was determined using computer simulations [42, 43]. Isotropic-to-nematic phase transition in systems of hard helical particles was investigated using Onsager theory and Monte Carlo computer simulations [44]. Hard pentagons and heptagons show a two-step isotropic-rotator-striped phase transition with increasing density [45,46]. Other systems of recent interest include hard convex type particle [47], bowl-shaped particles [48], octapods [49], convex and concave noncircular particles [50], dumbbells [51], polyhedra [52], banana or V-shaped particles [53], zigzag or bow-shaped particles [54,55], hard-cut spheres [56] and mixtures of particles [57–61] etc.

These entropy-driven phases are experimentally realized in anisometric inorganic colloids [62], colloids of polymethyl methacrylate [1], systems of tobacco mosaic virus [63, 64], rod-like *fd* and M13 viruses [65,66], silica particles [67,68], suspensions of inorganic and biological rod-like colloidal particles [69], boehmite particles [70], a monolayer consisting of anisotropic branched colloidal octapods [71], liquid crystals [3], colloidal cry-

tals of brownian square-crosses [72], squares [38], rectangles [39] and pentagons [46], banana-shaped molecules [73] etc.

Though extensively studied, the dependence of the phase diagram and the nature of the phases on the shape of the particles is not very clear. Despite sustained interest, there are only very few exactly solvable models. Only known solutions are for the hard hexagon on triangular lattice and related models [7,8] and a special limiting case of thin long cylinders in three dimensional continuum [6]. Thus, it is worthwhile to study different shapes to see whether a pattern may be deciphered. In this thesis, we focus on exclusion models that are defined on lattices. Such models are called hard core lattice gas (HCLG) models.

HCLG models

HCLGs have applications in diverse areas. These systems are closely related to freezing transitions [2, 74], directed and undirected lattice animals [75–77], and the Yang-Lee edge singularity [78]. By mapping occupied or vacancies to up and down spins these systems may be mapped onto antiferromagnetic spin systems albeit with infinite interaction strengths. The range of the interaction in these systems determines the shape and symmetry of the particle, hence the phase diagram. There have been numerous studies on disorder-order phase transitions of different shaped lattice gas particles on different lattices. Examples inlcue squares [11, 19, 79], hexagons [7], dimers [80–85], triangles [86], tetrominoes [87,88], rods [89,90], rectangles [20], y-shaped molecules [91], square-dimer mixtures [92], mixture of cubes [23], mixture of dimers [85]. Direct experimental realizations include adsorption of chlorine on silver (100) surface [4] and adsorption of selenium on nickel (100) surface [35].

In this thesis we focus on two HCLG models. (1) The k-NN model on the square lattice which is the discrete version of the hard disc system in two dimensions and (2) hard rectangles and squares on the square lattice. In sections 1.2 and 1.3, we summarize the known results for these models and the questions addressed in the thesis.

1.2 Hard spheres and k-NN model (Literature review)

1.2.1 Melting in hard discs and spheres

Introduced by Kirkwood [93] in 1950's the melting in hard spheres in three dimensional continuum is a well-known example of entropy-driven transitions. The hard-sphere system undergoes a first-order transition to a solid phase at high densities [2]. Though the existence and nature of the phase transition in three dimensional hard spheres is well established, the same is not true in two dimensions. Long range ordering, which is characteristic of a solid is not possible in two dimensions because of the thermal fluctuations of long-wavelength phonons [94, 95]. Yet hard spheres in two dimensions may have a solid-like phase [74]. A solid in three dimensions has long ranged positional order and long ranged orientational order of the bonds between neighboring particles. A solid in two dimensions however possess quasi-long-ranged positional order in the sense that the two point positional correlation function decays as a power law at large distances. Unlike positional order, orientational order in a two dimensional solid could be long-ranged. In a liquid whereas both correlations decay exponentially.

In two dimensions, the generally accepted Kosterlitz-Thouless-Halperin-Nelson-Young (KTHNY) scenario predicts an intermediate hexatic phase which has short ranged positional order and quasi-long-ranged orientational order. The theory predicts that melting in two dimensional hard spheres is through two continuous transitions: first from a solid phase to a hexatic phase and second from the hexatic phase to a liquid phase [96–98]. While the existence of the two transtions is well established and simulations are consistent with a continuous hexatic-solid transition, it is not clear whether the liquid-hexatic transition is continuous or discontinuous, and has been studied in detail recently [16, 99]. The results from Monte Carlo simulations of two dimensional Lennard Jones gas with soft interaction potentials are consistent with the liquid-hexatic transition being continuos [99]. However, large scale simulations of the hard discs in two dimensions using an

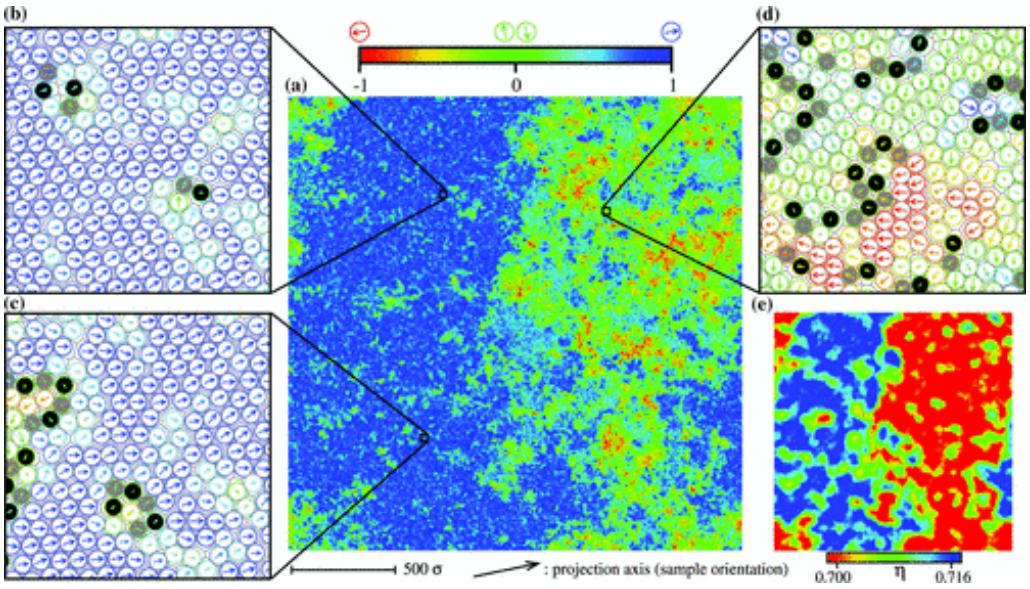

Figure 1.1: Phase coexistence of hard-spheres in two dimensions at density $\eta = 0.708$. (a) Long range orientational correlations coexist with short range correlations. This is shown by color-coding the local orientations. (b)–(c) zoomed-in views for the long orientational ordering (blue region). (d) zoomed-in view for the liquid region showing correlations over short-range. (e) shows the connection between density and local orientation. Figure courtesy [16].

event-chain Monte Carlo algorithm show that the liquid-hexatic transition is discontinuous [16]. Figure. 1.1 is a snapshot of the hard disc system showing phase coexistence between hexatic and liquid phases indicating a discontinuous phase transition. Such two-step melting scenario in two dimensions persists even for a quasi-two dimensional system of hard spheres with out-of-plane particle motions [100]. This discrepancy of findings of the nature of the transition may be due to the use of soft repulsive potential instead of hard-core potential in Ref. [99]. In Ref. [101] a system of soft spheres with repulsive power-law interactions have been studied using Monte-Carlo simulations. For interaction $\propto r^{-n}$ with $n \geq 6$, the system undergoes liquid-hexatic-solid transition where the liquid-hexatic transition is discontinuous, identical to the melting in two dimensional hard spheres. But for $n \leq 6$, the liquid-hexatic transition is continuous as in the KTHNY scenario. It is also possible to obtain a direct solid-liquid transition at low temperature and high density with suitable soft-core potential ($n = 14$) and hard-core diameter [102]. Extremely soft and long-ranged potential can be experimentally realized in colloidal two-dimensional

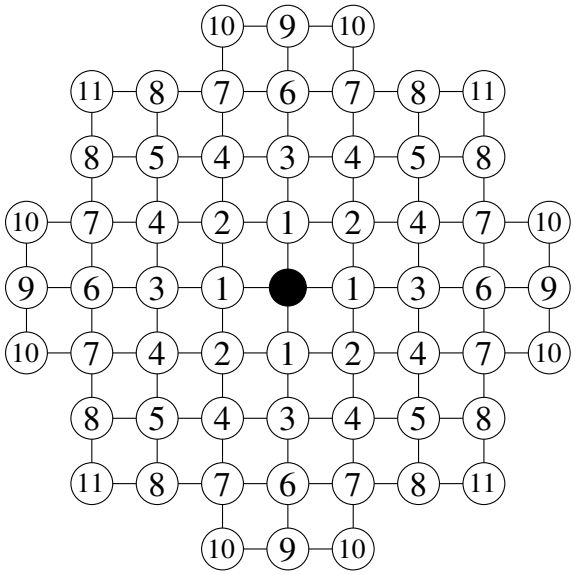

Figure 1.2: The lattices sites that are excluded by a particle (black filled circle) in the k-NN model. The labels denote the sites that are the k^{th} next nearest neighbors. For k-NN HCLG, all sites with labels less than or equal to k are excluded from being occupied by another particle.

systems [103]. Such systems generally follow KTHNY scenario of two continuous transitions.

1.2.2 k-NN HCLG model

The k-NN HCLG is the lattice version of the hard-sphere problem in the continuum, where larger k corresponds to smaller lattice spacing. In the k-NN model the first k nearest neighboring lattice points of a particle are excluded from being occupied by another particle. In Fig. 1.2, the sites excluded by a particle are shown for $k = 1, 2, \ldots, 11$. For a given k, all sites with labels less than or equal to k are excluded.

Introduced by Domb and Burley in the 1950s [104–106], the k-NN HCLG model has found applications in diverse areas of research. Examples include adsorption on surfaces [4, 28, 32–37], limiting cases of spin models [107–109], frustrated antiferromagnets at high magnetic fields [13, 110], glass transitions on square [111, 112] and Bethe lattices [113], study of two dimensional Rydberg gases [114], and in combinatorial prob-

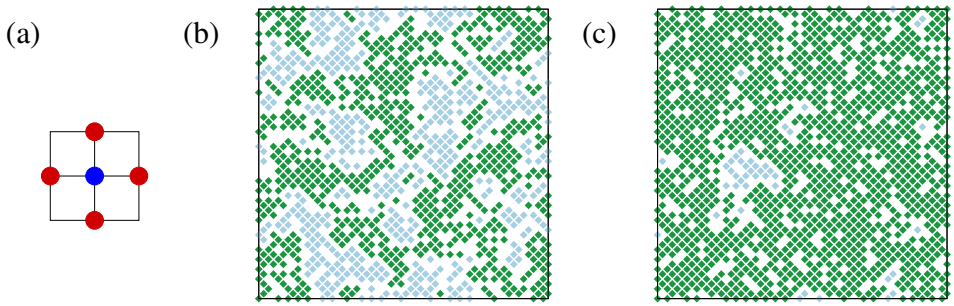

Figure 1.3: 1-NN model. (a) Schematic diagram of the model. Blue circle is the particle. Red circles are excluded lattice sites. Typical snapshots of a 1-NN system at (a) low density and (b) high density. In (b) and (c) particles in even diagonals are green in color whereas particles in odd diagonals are blue in color. (b) Disordered phase – both types of diagonals are equally occupied. (c) Sublattice-ordered phase – most of the particles are in even diagonals.

lems [115] such as unfriendly theater sitting problem [116], random independent set problem on graphs [117], loss networks [118], q-coloring graphs [119] and reconstruction problems [120].

We know summarize known results for the model.

1-NN model

The simplest non-trivial k-NN HCLG model is the nearest neighbor exclusion or 1-NN model [see Fig. 1.3(a)]. The 1-NN model undergoes a single transition from a disorderd fluid-like phase to an ordered solid-like phase with increasing density. The ordered high-density phase has sublattice order, where particles preferentially occupy either even or odd diagonals, breaking a two-fold symmetry [see Fig. 1.3(b) and (c)]. The system was initially investigated by activity and virial series and high-density expansion and the transition was found to be continuous [10, 11, 121]. The nature of the transition was found to be in the Ising universality class using transfer matrix [11, 122–129], series expansion [10, 130] and renormalization group methods [131, 132]. More recently, the equation of states of ordered and fluid phase were estimated by density functional theory [133]. The prediction of critical point is far from the actual one but it correctly captures the

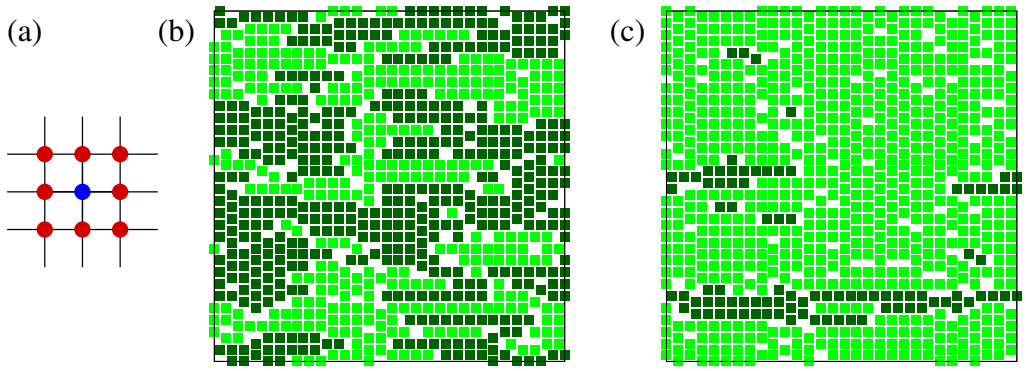

Figure 1.4: 2-NN model. (a) Schematic diagram of the model. Blue circle is the particle. Red circles are excluded lattice sites. Typical snapshots of a 2-NN system at (a) low density and (b) high density. In (b) and (c) light-green squares are particles on even columns while dark-green squares are particles in the odd columns. (b) Disordered phase – particles equally occupying even and odd columns, (c) Columnar-ordered phase – particles are mostly on even columns.

continuous nature of the phase transition. The different approximate analytical methods, for example ring approximation [106], Bethe approximation [106], necklace approximation [134], Rushbrooke and Scoins approximation (a generalization of Bethe method) [11] do not work very well for 1-NN model. These either cannot locate the transition point correctly [106] or fails to predict the true nature of the phase transition [134]. Numerical methods using Monte Carlo simulations unambiguously showed the transition to be Ising by calculating critical exponents using finite-size scaling theory [9, 108, 135–137].

2-NN model

The 2-NN model is a system of particles with nearest and next nearest neighbor exclusion. This is popularly known as 2×2 hard square model [see Fig. 1.4(a)]. This model undergoes one transition from disordered to ordered phase with increasing density. In contrast to 1-NN model, in this model the high density phase is columnar with partial translational order. In the columnar-ordered phase the particles preferentially occupy one of the rows (even or odd) or one of the columns (even or odd). Typical snapshots of a 2-NN system at low and high densities are shown in Fig. 1.4(b) and (c). At low density particles are in disordered phase occupying even and odd columns almost equally in Fig. 1.4(b), whereas

Table 1.1: The estimates for the critical fugacity z_c and critical density ρ_c obtained for disordered-columnar phase transition in 2-NN model from different approaches.

$z_c(2)$	$\rho_c(2)$	Method
97.50	0.932	Numerical [9, 12, 13, 142]
6.25	0.64	High density expansion (order one) [11, 19]
14.86	0.754	High density expansion (order two) [19]
135.9	-	Antiferromagnetic Ising model [22]
11.09	0.76	Fundamental measure theory [23, 24]
11.09	0.76	Approximate counting [25]
17.22	0.80	Cluster variational method [11]
11.09	0.76	Flory-type mean field [26]

at high density particles are in columnar-ordered phase occupying mostly even columns in Fig. 1.4(c).

The system has been considered as a limiting case of spin systems with infinite nearest and next-nearest neighbor coupling [22,107,108,138,139]. Some of these studies captured the existence of columnar phase, but the location, nature and universality class of the phase transition remained a puzzle. Initial studies with transfer-matrix [11, 14, 140, 141] and series expansion [11, 14] techniques either yielded no transition or mislocated the transition point. Whereas transfer matrix studies with phenomenological-scaling techniques correctly located the transition point and some of the critical exponents [12,107,139]. The approximation schemes like Rushbrooke and Scoins [11], cluster variational method [138] and density-functional-theory [23] underestimates the critical point by an order of magnitude. Recently a free energy expansion was developed [19, 142] in terms of vertical rods as a Mayer series in powers of $1/\sqrt{z}$ which gives significantly better estimate of critical point than previous series expansion results [11]. Critical point obtained by interface method as a limiting case of infinite interaction in the first and second nearest neighbor Ising antiferromagnet, gives a better estimate [22]. The estimates for the critical activity and density obtained by these methods are summarized in Table 1.1. Even if the continuous nature of the phase transition was established, finding the universality class using Monte-Carlo simulations created a lot of ambiguity. The 2-NN model goes to a columnar phase breaking a four-fold symmetry. The four columnar states give rise to a

XY model with four fold anisotropy [143]. Some models that exhibit transition breaking a four-fold symmetry are Eight-Vertex model and Ashkin-Teller model. The system belongs to Ashkin-Teller universality class, – a ferromagnetically coupled point which lies between the two dimensional Ising model and 4-state Potts model in the Ashkin-Teller phase diagram [12, 13, 142]. Since the correlation length critical exponent value is very close to Ising, some studies claimed it to be Ising [9].

3-NN model

The 3-NN model undergoes a transition from a disordered to a sublattice-ordered phase where the number of sublattices are ten. The phase transition is unambiguously showed to be first order by transfer matrix [11, 112, 140, 144–146], series expansion [11, 112], Rushbrooke and Scoins method [11] and Monte-Carlo [9] methods. The phase transition was also studied using Peierls' argument [17] and a new semi-analytic approach to treat first order phase transitions [147]. The 3-NN model has been used as zero temperature limit of finite interaction upto third-nearest-neighbor which again is a popular lattice-gas model of adsorption on crystal surfaces [148]. From dynamics study of 3-NN model by random sequential absorption deposition a glassy phase is claimed to exist below closest packing density [111]. The same is observed by low-density activity series in the fluid branch which extrapolates beyond critical point showing a super-cooled fluid phase [112].

4-NN model

For the 4-NN model, the exclusion radius of a particle extends upto 4-th nearest neighbor [see Fig. 1.2]. Previous studies claimed that the particle is equivalent to tilted hard squares of length $2\sqrt{2}a$ where a is the length of a cell in the lattice [see Fig. 1.5(a)]. These studies showed existence of a single phase transition to a sublattice-ordered phase where the sublattices are the same as the 1-NN model [9, 146]. Figure 1.5(b) is a typical fully-packed configuration. The lattice is divided into two sublattices, where lattice points on

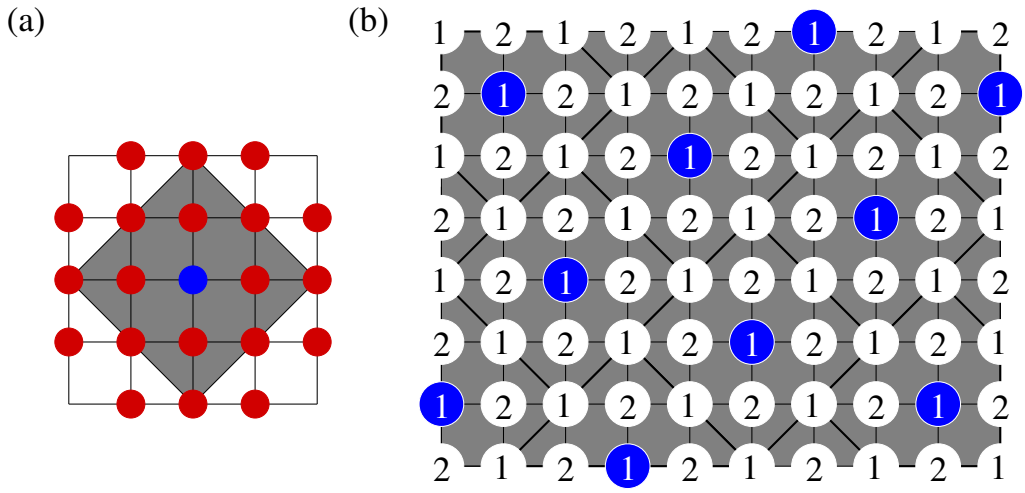

Figure 1.5: 4-NN model. (a) Schematic diagram of the model. Blue circle is the particle. Red circles are excluded lattice sites. The particle is equivalent to the grey square at fully packed configuration. (b) Sublattice division and a fully packed configuration according to Refs. [9, 146].

the odd diagonals are labelled as 1 and lattice points on even diagonals are labelled as 2. All the particle centres are on sublattice 1. The sublattices though are the same as 1-NN, the configuration is not exactly identical. In the ordered phase, the columns of the particles are slidable. Thus the configuration breaks translational order partially as seen in the columnar-ordered phase in 2-NN. Because of the presence of the partially broken translational symmetry, this particular sublattice-ordered phase is different from the high-density phases of 1-NN and 3-NN model.

Early transfer matrix studies suggested a single weak first order or continuous transition to sublattice-ordering [146]. The critical exponents obtained from Monte Carlo simulations are indistinguishable from those of the two dimensional Ising model [9]. However, the analysis based on cluster integrals excludes the possibility of the transition belonging to the Ising universality class [15].

5-NN model

The 5-NN model is equivalent to the 3×3 hard square problem and the high density phase is columnar as in the 2-NN model [9, 14]. The transition in the 5-NN model has

Table 1.2: The nature of the ordered phases and the transitions for $k \leq 6$. Question marks denote that the result is not known.

k	Ordered phases	Nature of transition
1	Sublattice	Continuous (Ising)
2	Columnar	Continuous (Ashkin-Teller)
3	Sublattice	Discontinuous
4	Sublattice	Continuous (Ising?)
5	Columnar	Discontinuous

been numerically shown to be first order [9], though very early studies claimed absence of a phase transition [14]. Mayer cluster integrals fails to identify the transition point correctly [15].

Larger k-NN models

Not much is known for $k \geq 6$. It becomes increasingly difficult to equilibrate systems with large k in Monte Carlo simulations that use only local evaporation, deposition and diffusion moves. At high densities, when the excluded volume of a particle is large, the system gets stuck in long lived metastable states. Thus, reliable data can be obtained only for low densities or small excluded volumes. Mean field approximations predict single continuous transitions for $k = 1, 2$ and single first order transitions for $k > 2$ [143]. The known results are tabulated in Table 1.2.

1.2.3 Questions addressed

The estimates for the critical activity and density of the 2-NN or the hard square model from analytical methods are significantly different from the critical acitivity and density obtained from numerical simulations. Approximation schemes like different versions of mean-field theory, cluster variational methods, and density functional theory, do not capture the correlations in the columnar phase well. *Is it possible to develop a systematic scheme by which we could obtain more accurate estimates of the critical activity and*

critical density of the diordered-columnar transition in the 2-NN model?

Monte Carlo simulations of the 4-NN model show a single continuous transition from a disordered phase to an ordered phase. The data are consistent with the transition belonging to the Ising universality class. However, analysis based on cluster integrals excludes the possibility of the transition being in the Ising universality class. A straightforward analysis of the fully packed configuration shows that it has a eight-fold symmetry in contrast to the previous claims of a two-fold symmetry [9, 146]. By analogy with the q-state Potts model for which the transition is discontinuous for $q > 4$, one would expect a first order transition as seen for k=3, 5, in contradiction with the numerical data.

What is the rationalization for the 4-NN model undergoing a continuous Ising like transition instead of a discontinuous transition?

Unlike the hard-disc problem, known results for the k-NN model show that there is only one transition with increasing density. It becomes very difficult to study the models with $k > 5$ using Monte Carlo simulations with local evaporation and deposition moves as the system tends to get stuck in long-lived metastable equilibrium states during its evolution. *Is it possible to implement an algorithm that allows the study of models with $k > 5$? Is it possible that there are multiple transitions for larger k? What happens at the large k limit of the k-NN model?*

In this thesis, we address these *questions* through a combination of analytical and numerical methods.

1.3 Hard rectangles (Literature review)

1.3.1 Continuum models

A system of rectangles or rod-shaped particles, which have two-fold rotational symmetry is expected to show a nematic phase which has similar symmetry. Similarly a system of squares which has four-fold symmetry is expected to show a tetratic phase with similar symmetry. But the effect of the shape of the particles on the phase diagram is not very clear.

A system of long rods in three dimensions with only excluded volume interactions is known to exhibit a density-driven phase transition from a disordered isotropic phase to an orientationally ordered nematic phase [3, 6, 149–151]. Further increase in density may result in a smectic phase with orientational order and partial translational order, and a solid phase [42, 152]. In two dimensional continuum space, the system undergoes a Berezinskii-Kosterlitz-Thouless transition [96, 153, 154] from a low-density phase with exponential decay of correlations to a high-density phase where the correlations decay as a power law [155–158].

Numerical simulations on a system of rectangles of aspect ratio 2 indicate a KTHNY type transition from a isotropic liquid phase to a tetratic solid phase with an intermediate tetratic liquid phase [40]. The tetratic liquid phase has a quasi-long range four-fold orientational order and no positional order, whereas the tetratic solid phase has a quasi-long range orientational and positional order. A system of rectangles with aspect ratio 6.4 is studied experimentally where a single KT transition from isotropic to nematic phase is observed with an intermediate almost-tetratic phase [39]. The tetratic phase is also observed experimentally on a vibrated-rod monolayer [159].

An experiment on Brownian squares found an intermediate six-fold hexagonal phase in between the low-density isotropic and high-density four-fold solid phase [38]. This is in

contrast to the numerical and experimental results which showed existence of a four-fold tetratic phase in between the isotropic and four-fold solid phase [160, 161]. According to recent numerical simulations this contradiction is due to the effect of corner-roundedness of the particles [41].

1.3.2 Lattice models

The model of hard rectangles and hard rods have been studied on lattices where the particles orient only along the lattice directions. Thus the number of allowed orientations is finite. In this case, it may be heuristically argued that the fully packed phase has no orientational order [3, 89]. There has been a renewed interest in this problem after it was convincingly demonstrated numerically that a system of hard rods on a square lattice exhibits a nematic phase for large enough aspect ratio [89].

Systems of hard rectangles or rods with two orientations on square lattice have rich phase diagrams. These phase diagrams depend only on the width and aspect ratio of the rectangles. Consider a mono-dispersed system of hard rectangles of size $m \times d$ ($d \geq m$) on a square lattice, where $k = d/m$ is the aspect ratio, and each rectangle may orient along one of two directions – horizontal or vertical. No two rectangles may overlap. We summarize the known results for these systems with different sets of m and k below.

Hard rods

For $m = 1$ the system consists of hard rods of length k. The system has been shown to undergo two density-driven transitions: a low-density isotropic–nematic transition shown numerically for $k \geq 7$ [89] and rigorously for $k \gg 1$ [18], and a second high-density nematic–disordered transition that has been shown numerically [90, 162]. While the first transition is in the Ising universality class [163–167], there is no clear-cut evidence for the second transition belonging to any known universality class [90]. The three phases

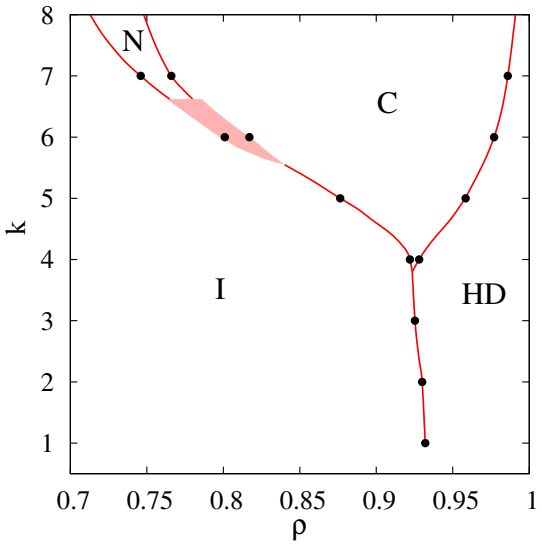

Figure 1.6: Phase diagram for $2 \times 2k$ rectangles, where k is an integer. I, N, C, HD refer to Isotropic, Nematic, Columnar and High-Density phases. Figure courtesy [20].

persist for small polydispersity [168, 169]. The $m = 1$ model may be solved exactly on a tree-like lattice where the system undergoes an isotropic–nematic transition for $k \geq 4$, but the second transition is absent [170], though an exact solution for rods with soft repulsive interactions on the same lattice shows two transitions [171]. The only other rigorous result is for $m = 1$ and $k = 2$ (dimers), where the absence of a transition for any density may be proved [82–84, 172].

Hard squares

When $k = 1$, and $m \geq 2$, the model reduces to the well-studied hard square model [11, 14, 19, 22, 23, 107, 108, 139–141, 173] which undergoes a density-driven transition from a disordered to a columnar phase. The transition is continuous for $m = 2$ [9, 12, 13] and first order for $m = 3$ [9]. The columnar phase breaks translational symmetry only in one lattice direction. For $m = 2$, the system is actually the 2-NN model. The known results for the 2-NN model are summarized in Sec. 1.2.2.

Hard rectangles with $k < 7$

For $2 \leq k < 7$, and $m \geq 3$, the system undergoes two first order transitions: isotropic-columnar and columnar-sublattice, with increasing density. When $m = 2$, and $k = 2, 3$, the system undergoes a single transition from the disordered isotropic phase to a solid-like sublattice phase [20]. The transition belongs to Ashkin-Teller universality class. For $m = 2$ and $4 \leq k < 7$ the system undergoes two transitions, the first one being isotropic-columnar and the second columnar-sublattice [20]. For $k = 4, 5$, the isotropic-columnar transition belongs to Ashkin-Teller universality class whereas for $k = 6$ the transition is first order. The columnar-sublattice transition belongs to Ashkin-teller universality class for all three k values [20].

Hard rectangles with $k \geq 7$

When $m \geq 2$ and $k \geq 7$, the system undergoes three density-driven transitions: first an isotropic-nematic transition, second a nematic-columnar transition, and third a columnar-sublattice transition [20, 21]. Here, the columnar phase breaks translational symmetry in the direction perpendicular to the nematic orientation and the sublattice phase, unlike the columnar phase, breaks translational symmetry in both directions.

Phase diagram of a $2 \times 2k$ rectangles is presented in Fig. 1.6.

Isotropic-Nematic (I-N) transition The limit $k \to \infty$ keeping m fixed, corresponds to the limit of oriented rods in continuum [20]. Thus the critical density at this limit should be independent of m. The critical density at this limit in three dimensions obtained from an exact virial expansion gives $\rho_c^{I-N} \approx A_1 k^{-1}$ [6, 150, 151]. In two dimensional continuum A_1 can be obtained by numerical simulations of oriented rods of length ℓ. The critical number density for this is $\approx A_1 \ell^{-2}$. A simulation of oriented rods of $\ell = 1$ in two dimensional continuum obtained $A_1 \approx 4.84$ [167]. For systems of long rods with k up to 60 on square lattice, numerical simulations found $\rho_c^{I-N} \approx 4.80 k^{-1}$ [21].

Table 1.3: The estimates for the critical fugacity z_c and critical density ρ_c obtained for nematic-columnar phase transition from different approaches for $d \gg 1$.

$z_c(d)$	$\rho_c(d)$	Method
$\frac{71.0}{d}$	$0.73 + \frac{0.46}{d}$	Numerical [21]
-	$0.59 + \frac{0.29}{d}$	Bethe approximation [20]

The I-N transition was also studied analytically using an ad-hoc Bethe approximation and a truncated virial expansion and numerically for rectangles of large aspect ratio [21]. A_1 was found to be independent of m. Numerically obtained estimate of A_1 is 4.80 where both the analytical theories predict $A_1 \approx 2$. Thus, at $m \to \infty$ limit, the continuum model of oriented rectangles of aspect ratio k, an I-N transition exists at a critical density proportional to k^{-1}.

Columnar-Sublattice (C-S) transition The entropy estimates of the columnar and sublattices phases predicts the critical density for the C-S transition to be $\rho_c^{C-S} \approx 1 - A_2/(mk^2)$ for large k, where A_2 is a constant [20]. This could not be verified numerically overcoming the difficulty of equilibration at such high densities. In the limit of $m \to \infty$ with fixed k, $\rho_c^{C-S} \to 1$, implying the nonexistence of the sublattice phase in systems of oriented rectangles in continuum.

Nematic-Columnar (N-C) transition Numerical simulations of rectangles of $m = 2$ and large k, found $\rho_c^{N-C} \approx 0.73 + 0.23k^{-1}$, where the transition belongs to the Ising universality class [21]. A Bethe approximation predicted the density of the N-C transition in hard rectangles is given by, $\rho_c^{N-C} \approx A_3(m) + A_4(m)k^{-1}$ at limit $k \to \infty$ where $A_3(m) \leq 1$ [20]. This limit, keeping m fixed corresponds to existence of a columnar phase in oriented long rectangles in the continuum. Within this approximation the critical density tends to 1 at $m, k \to \infty$. As this gives an upper bound of N-C transition, the continuum model will have a columnar-like phase through a second transition, the first one being I-N.

1.3.3 Questions addressed

Interestingly, the critical value of density $\rho_c(d)$ and activity $z_c(d)$ for the nematic-columnar transition remains finite even as $d \to \infty$. From Monte Carlo simulations $\rho_c(2) \approx 0.932$, and $z_c(2) \approx 97.5$ [9, 12, 13, 92], while $\rho_c(d) \approx 0.73 + 0.46d^{-1} + O(d^{-2})$, $z_c(d) \approx 71.0d^{-1} + O(d^{-2})$ [21]. There have been several attempts at obtaining these results analytically. These include high density expansions [11, 19, 174], fundamental measure theory [23], Flory-type mean field approximations [26], approximate counting schemes [25], from mapping the model onto the next-nearest neighbor model antiferromagnetic Ising model [22], and Bethe approximation [20]. The results obtained by these methods are summarized in Table 1.1 and Table 1.3. It is clear that all the estimates differ considerably from the numerically obtained values. Further, except for the high density expansion, the other methods are ad hoc and hence it is not clear how they may be improved upon. There has been a lot of interest in the study of columnar, or stripe order in recent years [175]. It is encountered in many different settings, such as liquid crystals [3], frustrated spin systems, both classical [81, 176], and quantum [177, 178], and hard core lattice gas models [11, 19, 20, 92, 179]. Also in our study of the k-NN model it will be observed that understanding the columnar phase is crucial to determine whether multiple transitions are present. However, our understanding of columnar ordering is still not very satisfactory. For instance, while there exists rigorous proof for the existence of the solid-like sublattice [17, 180, 181] and nematic phases [18], there is no corresponding result for columnar order.

Is it possible to develop a systematic scheme by which we could obtain more accurate estimates of the critical activity and critical density of the nematic-columnar transition in a system of hard rectangles? In this thesis, we address this *question* through two different analytical methods–high density expansion in terms of defects about the perfectly columnar phase and calculation of interfacial energy between two differently-ordered perfectly columnar phase.

1.4 Overview of the thesis

In this thesis, we address the questions raised in Secs. 1.2.3 and 1.3.3. The results obtained and the organization of the thesis are summarized below.

In **Chapter 2**, we describe a Monte Carlo algorithm suitable for studying hard core particles on lattices. This algorithm with global moves overcomes the difficulty of slowing down at high densities and is able to equilibrate the system. The algorithm is thus more efficient than that with local moves. It is also easily parallelizable, allowing us to perform large scale simulations. We describe the algorithm for k-NN models and hard horizontal rectangles on square lattice.

In **Chapter 3**, we investigate the 4-NN model. Using large scale Monte Carlo simulations we find the existence of two continuous transitions with increasing density of particles – the first from low-density disordered to sublattice-ordered phase and the second from sublattice-ordered to columnar-ordered phase. From finite size scaling analysis near critical point we establish that the first transition belongs to Ising class whereas the second to Ashkin-Teller universality class. We further analytically rationalize the existence of the intermediate sublattice-ordered phase by series expansion about a perfectly columnar state in terms of defects.

In **Chapter 4**, we conjecture a criteria for multiple transitions in k-NN models from high-density expansion about columnar state. Applying this conjecture we claim that $k = 10$, 11, 14, ... should have multiple transitions and $k = 6$, 7, 8, 9, ... should have single phase transition. We verify the same in k-NN models with $6 \leq k \leq 11$ using Monte Carlo simulations. We find single first-order transitions for $k = 6, 7, 8, 9$ and multiple transitions for $k = 10, 11$.

In **Chapter 5**, extending the conjecture of multiple transitions, we argue that existence of such multiple transitions can be predicted from the close packing structure. We implement a simple algorithm to find out close packing structure for each k-NN. We determine the

nature of the phase at full packing for k up to 820302. We show that there are only eighteen values of k, all less than $k = 4134$, that show columnar order, while the others show solid-like sublattice order.

In **Chapter 6**, we study a system of monodispersed hard rectangles of size $m \times d$, where $d \geq m$ on a two dimensional square lattice. For large d, the threshold density for the I-N transition ρ_1^* tends to 0, and the critical density for the C-S transition ρ_3^* tends to 1. Interestingly, simulations have shown that the critical density for the N-C transition ρ_2^* tends to a non-trivial finite value ≈ 0.73, as $d \to \infty$, and $\rho_2^* \approx 0.93$ for $d = 2$. We study the nematic-columnar transition by developing a high-activity expansion in integer powers of $z^{-1/d}$ for the columnar phase in a model where the rectangles are allowed to orient only in one direction. By deriving the exact expression for the first $d + 2$ terms in the expansion, we obtain estimates for the critical density and activity. For m, $k \gg 1$, these estimates decrease with increasing k and decreasing m.

In **Chapter 7**, we study a system of $2 \times d$ hard rectangles on square lattice. We determine critical density and activity for N-C transition approximately by theoretically determining the density for which interfacial tension between two different columnar phases vanishes. We obtain $\rho_2^* = 0.746$, for $d \to \infty$, and $\rho_2^* = 0.923$ for $d = 2$. For all values of d, the estimates of ρ_2^* show good agreement with Monte Carlo data.

Each chapter ends with a summary and discussion of promising areas for future research.

Chapter 2

Numerical methods

Conventional simulations of HCLG models of particles with large excluded volumes are difficult to equilibrate at high densities because the system tends to get stuck in long lived metastable equilibrium states. In this chapter, we describe a Monte Carlo algorithm [90, 162] with global moves that overcomes this difficulty. Its efficiency in equilibration was initially demonstrated for a system of hard rods for which equilibration was possible for densities upto 0.99 [90, 162]. Other implementations include hard rectangles [20, 21, 182] and squares [142]. More recently, the algorithm has been improved such that it works at full packing also, and demonstarted for a mixture of hard squares and dimers [92].

We describe the implementation of the algorithm for the k-NN model in Sec. 2.1 and hard rectangles in Sec. 2.2. Section 2.3 contains a final discussion.

2.1 k-NN model

We describe the implementation of the algorithm for the 1-NN model and then outline the modifications required to implement it for larger k.

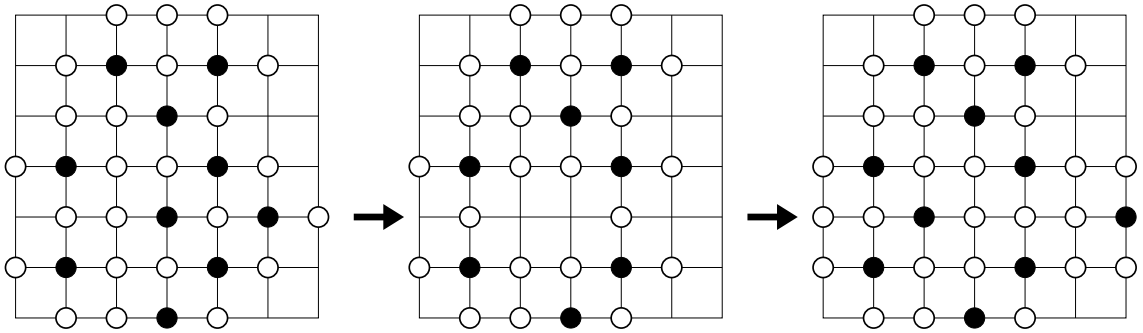

Figure 2.1: The Monte Carlo algorithm illustrated for 1-NN. (a) A typical valid configuration. The lattice consists of particles (filled circles), excluded sites (empty circles) and empty sites where a particle may be added to obtain a new valid configuration. (b) A row is chosen at random (denoted by arrow) and all particles on that row are removed. The row is now divided into intervals of contiguous empty sites by the excluded sites. (c) The row is reoccupied with a new valid configuration with the correct equilibrium weight.

2.1.1 1-NN model

Consider a valid configuration of the 1-NN model [see Fig. 2.1 (a)]. A row or column is chosen at random (say a row) and all particles on that row are removed. The aim is to reoccupy the row with a new configuration with the correct equilibrium weight. After evaporation, the row is divided by the excluded sites into intervals of contiguous empty sites [see Fig. 2.1 (b)]. In the 1-NN model, along a row, a particle excludes the nearest neighbor from being occupied by a particle. Thus, the particle configuration in an interval is independent of its neighboring intervals, and the re-occupation of the row reduces to the occupation of empty intervals.

The calculation of probability of a configuration may be determined from the exact solution of the one dimensional problem on a lattice of length l with open and periodic boundary conditions. Let $\Omega_o(z,\ell)$ [$\Omega_p(z,\ell)$] denote the partition function of the problem with nearest neighbor exclusion on a lattice with open [periodic] boundary conditions.

They obey recursion relations

$$\Omega_o(z,\ell) = 1 + \ell z(1-\delta_{\ell,0}),\ \ell = 0,\ldots,d, \tag{2.1a}$$

$$\Omega_o(z,\ell) = z\Omega(z,\ell-d-1) + \Omega(z,\ell-1),\ \ell > d, \tag{2.1b}$$

$$\Omega_p(z,L) = dz\Omega_o(z,L-2d-1) + \Omega_o(z,L-d), \tag{2.1c}$$

where for the 1-NN model, $d = 1$. Given an empty interval of length $\ell < L$, the probability that the left most site is occupied equals $z\Omega_{z,\ell-d}/\Omega_\ell$. If $\ell = L$, then the probability that one of the first d sites is occupied equals $dz\Omega_{z,L-d-2}/\Omega_p(z,L)$. These probabilities are calculated for all ℓ and stored as input for the Monte Carlo simulations. A Monte Carlo step corresponds to $2L$ such evaporation–deposition moves. It is straightforward to show that the algorithm is ergodic and obeys detailed balance.

2.1.2 k-NN models with $k > 1$

The algorithm is easily generalized to higher values of k. However, one cannot always choose rows and columns for the evaporation–deposition moves because the occupation of the empty intervals may no longer be independent of one another. This is most easily seen for the 3-NN model, where along a row, a particle excludes the nearest and next nearest neighbors. However, in a row, only one site is excluded by a particle that is two rows away. An example is shown in Fig. 2.2. A valid configuration is shown in Fig. 2.2(a). If a deposition is attempted in the row denoted by an arrow [see Fig. 2.2(b)], then the occupation of site A excludes site B which belongs to a different empty interval. This makes the occupation of different empty intervals interdependent. However, if one attempts evaporation and deposition along diagonals oriented in the $\pi/4$ direction [Fig. 2.2(c)], then the occupation of empty intervals become independent of each other. In Table 2.1, we tabulate the orientations of the diagonals for the evaporation–deposition moves that we have used for k up to $k = 11$. For each of these choices, the values of d that should be used in

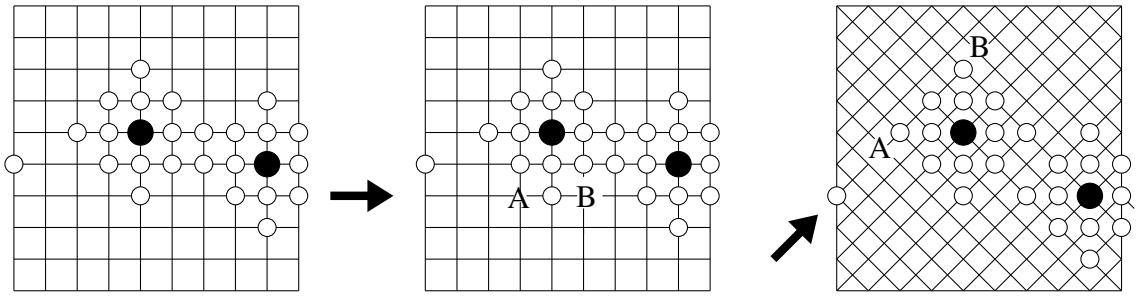

Figure 2.2: An example of the algorithm for 3-NN. (a) A valid configuration of 2 particles (filled circles) and excluded sites (empty circles). (b) Adding particles in a row (denoted by arrow) by deposition. If a particle is added at A, then its exclusion range includes B. Thus, the occupation of the empty intervals are not independent. (c) Adding particles in a diagonal oriented in the $\pi/4$ direction (denoted by arrow). Now the occupation of the empty intervals are independent of each other.

Eq. (2.1) are also tabulated in Table 2.1.

We implement a parallel version of the above algorithm. The evaporation and deposition of particles in two rows in the 1-NN model (diagonals in general) that have at least $\Delta - 1$ rows between them ($\Delta = 2$ for the 1-NN model) are independent of each other. The value of Δ for different k are given in Table 2.1. Hence, we update simultaneously every Δth row. Once all rows are updated in this manner, the columns are updated. The parallelization and efficiency of the algorithm allows us to simulate large system sizes and high densities.

We check for equilibration by initializing the simulations with two different initial configurations, corresponding to two different phases, and making sure that the final equilibrium state is independent of the initial condition. One configuration is a fully packed state and the other is a random configuration where particles are deposited at random.

In a typical run for a fixed value of μ, after equilibration, the different thermodynamic quantities are averaged over 10^8 Monte Carlo steps that are divided into 10 statistically independent blocks for estimating errors.

In addition, we use the method of histogram re-weighting [183] to extrapolate for values of μ that are not directly simulated. This allows us to determine quantities like the

Table 2.1: For each k, the orientation of the diagonals along which particles are evaporated and deposited, and the corresponding value of d to be used in Eq. (2.1) are tabulated. Evaporation and deposition along diagonals separated by Δ or more are independent.

k	orientation of diagonal	d	Δ
1	$0, \pi/2$	1	2
2	$0, \pi/2$	1	2
3	$\pi/4, 3\pi/4$	1	3
4	$0, \pi/2$	2	3
5	$0, \pi/2$	2	3
6	$\tan^{-1}(\pm 2), \tan^{-1}(\pm 1/2)$	1	7
7	$\pi/4, 3\pi/4$	2	5
	$0, \pi/2$	3	4
8	$\pi/4, 3\pi/4$	2	6
	$0, \pi/2$	3	4
9	$\pi/4, 3\pi/4$	2	6
10	$\pi/4, 3\pi/4$	2	6
11	$\tan^{-1}(\pm 2), \tan^{-1}(\pm 1/2)$	1	10

maximum value of susceptibility and its location more precisely.

2.2 Hard rectangles

In this section we describe implementation of the Monte Carlo algorithm for systems of hard rectangles. Consider a square lattice of size $L \times L$ with periodic boundary conditions. We consider a system of monodispersed hard horizontal rectangles of size $m \times d$, where $k = d/m$ is the aspect ratio, and $d \geq m$. A horizontal rectangle occupies d consecutive lattice sites along the x-direction and m consecutive lattice sites along the y-direction. No lattice site may be occupied by more than one rectangle. The grand canonical partition function for the system is

$$\overline{\mathcal{L}}(z_h) = \sum_{n_h} \overline{C}(n_h) z_h^{n_h}, \tag{2.2}$$

where $\overline{C}(n_h)$ is the number of valid configurations with n_h horizontal rectangles, and z_h is the corresponding activity.

We call the bottom-left corner of a rectangle as its head. Consider a valid configuration

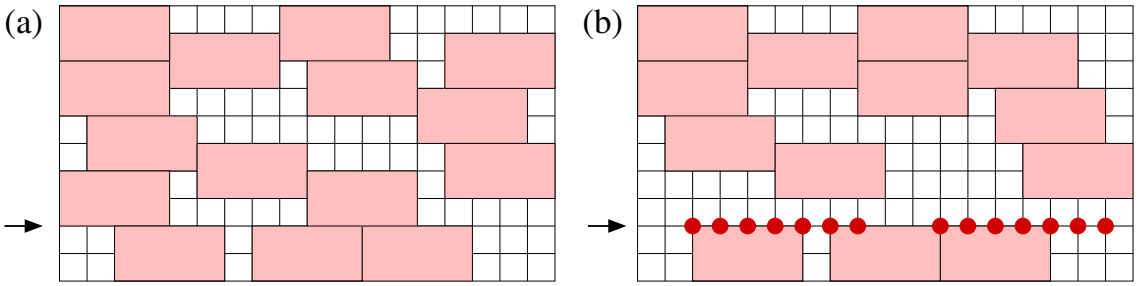

Figure 2.3: The Monte Carlo algorithm illustrated for 2×4 horizontal rectangles. (a) A typical valid configuration. (b) A row is chosen at random (denoted by arrow) and all rectangles with head on that row are removed. The row is now divided into intervals of contiguous empty sites by the excluded sites (denoted by red circles).

[see Fig. 2.3(a)]. A row is chosen at random and all rectangles with head on that row are removed [see Fig. 2.3(b)]. After evaporation the row now consists of forbidden sites due to rectangles with heads in the neighboring $(m-1)$ rows and empty sites. The sites that may be reoccupied with horizontal rectangles are thus divided into intervals of contiguous empty sites. Reoccupation of the row with rectangles with heads on that row now reduces to problem of reoccupying the row with rods of length d. Each empty intervals can be reoccupied independently. For this we need to calculate occupation probability of one-dimensional rows with rods of length d. A Monte Carlo move corresponds to $2L$ such evaporation-deposition moves.

Consider $\Omega_p(z, L)$ is the grand canonical partition function of a system of hard rods of length d on a one dimensional lattice of L sites with periodic boundary condition and $\Omega_o(z, \ell)$ is the corresponding grand canonical partition function with open boundary conditions. $\Omega_p(z, L)$ is related to $\Omega_o(z, \ell)$ as

$$\Omega_p(z, L) = dz\Omega_o(z, L-d) + \Omega_o(z, L-1), \ L \geq d. \tag{2.3}$$

$\Omega_o(z, \ell)$ obeys the following recursion relation:

$$\Omega_o(z, \ell) = z\Omega_o(z, \ell-d) + \Omega_o(z, \ell-1), \ \ell \geq d, \tag{2.4}$$

$$\Omega_o(z, \ell) = 1, \ 0 \leq \ell < d. \tag{2.5}$$

Equation (2.4) is solved by the ansatz $\Omega_o(z,\ell) = A\lambda^\ell$, where A is a constant. Substituting into Eq. (2.4), we obtain

$$\lambda^d - \lambda^{d-1} - z = 0. \tag{2.6}$$

$\Omega_o(z,\ell)$ is a linear combination of the d roots of Eq. (2.6). Denoting the roots by λ_n,

$$\Omega_o(z,\ell) = \sum_{n=1}^{d} c_n \lambda_n^\ell, \tag{2.7}$$

where c_n are constants to be determined from Eq. (2.5).

All the equilibrium probabilities of the one dimensional chain can be calculated exactly once we obtain $\Omega_o(z,\ell)$. The probability that the left most site of an open one dimensional chain of length ℓ is occupied by the head of a horizontal rod is

$$p_\ell = z\,\frac{\Omega_o(z,\ell-d)}{\Omega_o(z,\ell)}, \tag{2.8}$$

and the probability of it being empty is $(1-p_\ell)$. If occupied, we move to the d-th neighbor of the head along the chain and reduce the length of the open interval to be occupied by d. If not occupied, we consider the neighbor to the right of the site and reduce the length of the open interval by one. If the whole row is empty probability of occupying a site by a rod is

$$p_L = zd\,\frac{\Omega_o(z,L-d)}{\Omega_p(z,L)}. \tag{2.9}$$

The algorithm is parallelizable as occupation of rows with horizontal rectangles which are in a gap of m are independent. Thus deposition of rectangles in theses rows gapped by m can be done simultaneously. We have used Open Multi-Processing for parallel computation.

The algorithm discussed here for horizontal rectangles can be easily extended to include vertical rectangles with evaporation and deposition along columns. In case of hard rectangles an additional flip move can reduce the autocorrelation time considerably [20].

2.3 Discussion

We discussed an efficient Monte Carlo algorithm with global moves. The algorithm overcomes the difficulty of extremely long equilibration times faced by Monte Carlo algorithms with only local moves.

The algorithm used in the chapter is well suited to efficiently study hard core exclusion models on other lattices, dimensions, and for particles of different shapes. In three dimensions, simulations of hard cubes in the continuum show a first order transition from a disordered phase to a simple cubic crystal phase [184]. It would be interesting to study the lattice version of the hard cube model as well as the k-NN model in three dimensions, and obtain the phase diagram. Another interesting problem is that of rounded squares in two dimensions. Recent experiments on brownian squares report the existence of hexagonal, rhombic and square phases [38]. Some of these features have been reproduced in simulations of rounded squares [41, 185]. It is straightforward to make a lattice version of such shapes, making it suitable to be studied by this algorithm.

Chapter 3

4-NN model on square lattice

3.1 Introduction

In this chapter, we focus on the 4-NN hard core lattice gas model (HCLG), where the first 4 next nearest neighbors of a particle may not be occupied by another particle, on the two dimensional square lattice [see Fig. 3.1].

We study the 4-NN model by adapting and implementing an efficient algorithm with cluster moves [162]. The algorithm is explained in detail in Sec. 2.1.2. For the 4-NN model,

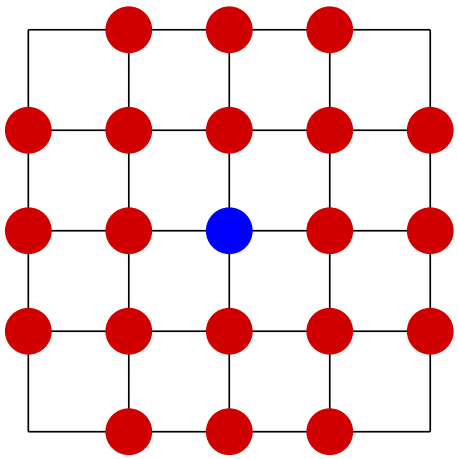

Figure 3.1: The 4-NN model. Blue circle is a particle and red circles are excluded sites.

we show that the system undergoes two continuous transitions with increasing density and that the high density phase is columnar. This, in effect, resolves the question of why the 4-NN model showed a continuous transition by arguing that the eight fold symmetry of the model is broken in two steps. The exponents describing the two transitions are numerically determined. The first transition is consistent with the Ising universality class while the second transition has exponents that belong to the two color Ashkin Teller model. The numerical study of the 4-NN model is presented in Sec. 3.2. In Sec. 3.3, we calculate the first four terms in the high density expansion for the free energy and the densities of particles in the different sublattices of the 4-NN model. From the form of the expansion, it is seen that the columnar order has a sliding instability in only some sublattices. This observation is used to heuristically argue why the system shows two entropy driven transitions. Section 3.4 contains a discussion of the results. The content of this chapter is published in Ref. [179].

3.2 Two transitions in the 4-NN model

In this section, we show numerically that the 4-NN model undergoes two phase transitions with increasing density. To assist in defining the different phases, we divide the lattice into sublattices by assigning 2 labels to each site. Each lattice site belongs to a diagonal oriented in the $\pi/4$ direction and to a diagonal oriented in the $3\pi/4$ direction. All sites that belong to a diagonal with orientation $\pi/4$ are assigned a label from 0 to 3 as shown in Fig. 3.2(a). If the coordinates of a site are (x, y), then the label is $[(x - y) \mod 4]$. Similarly, all sites that belong to a diagonal with orientation $3\pi/4$ are assigned a label from 4 to 7 as shown in Fig. 3.2(b). If the coordinates of a site are (x, y), then the label is $[(x + y) \mod 4 + 4]$.

In Fig. 3.3, we show typical snapshots of the equilibrated system at low, intermediate and high densities. In the left panels, all particles belonging to sublattice i ($i = 0, 1, 2, 3$)

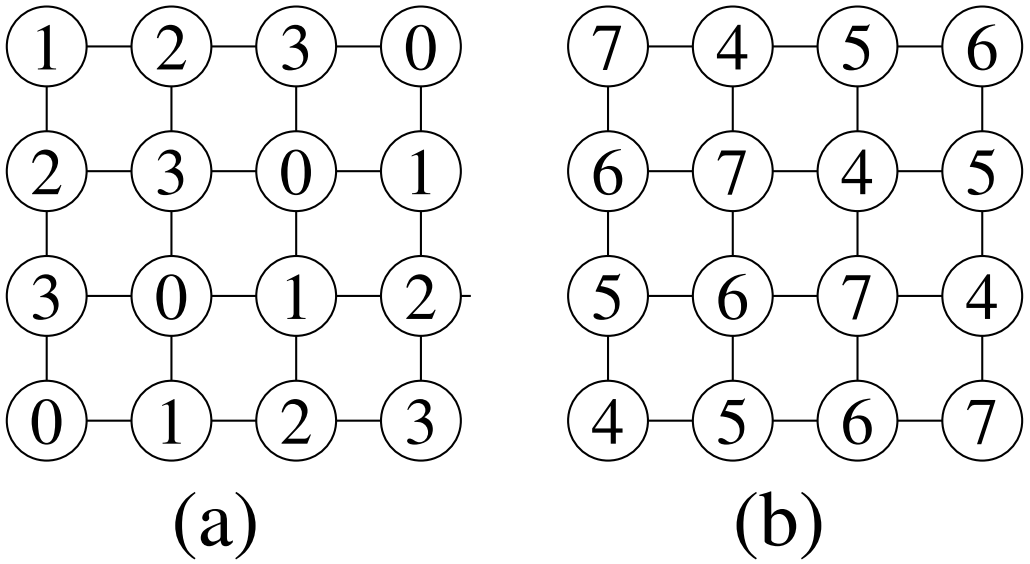

Figure 3.2: The sublattice labeling for 4-NN. (a) All sites belonging to a diagonal oriented in the $\pi/4$ direction have same label. If the site has coordinates (x, y), then the label is $[(x - y) \mod 4]$. (b) All sites belonging to a diagonal oriented in the $3\pi/4$ direction have same label. If the site has coordinates (x, y), then the label is $[(x + y) \mod 4 + 4]$. In addition, all sites with label 0 or 2 (or equivalently 4 and 6) will be called sublattice A and all sites with label 1 or 3 (or equivalently 5 and 7) will be called sublattice B.

have the same color. Similarly, in the right panels, all particles belonging to sublattice i ($i = 4, 5, 6, 7$) have the same color. At low densities [see Fig. 3.3(a)], all four colors are present (roughly equal) in both the left and right panels. This is the disordered phase with equal occupation of all sublattices $0, \ldots, 7$. At intermediate densities [see Fig. 3.3(b)], we find that that majority of particles have two of the four colors in both left and right panels. This corresponds to particles preferably occupying either the even sublattices or the odd sublattices. There are two such states corresponding to particles in sublattices $(0, 2)$ and $(4, 6)$ or in sublattices $(1, 3)$ and $(5, 7)$. If we label the sites on sublattices 0 and 2 (equivalently 4 and 6) as A and the sites on sublattices 1 and 3 (equivalently 5 and 7) as B, then this intermediate phase breaks the symmetry between A and B sublattices. We will call this phase a sublattice phase (following the terminology in Ref. [9]). We note that this phase was observed in Ref. [9]. At high densities [see Fig. 3.3(c)], we find that the particles occupy one of the four sublattices from 0–3 or 4–7, but not from both. In the example shown in Fig. 3.3(c), in the left panel, particles preferentially occupy sublattice

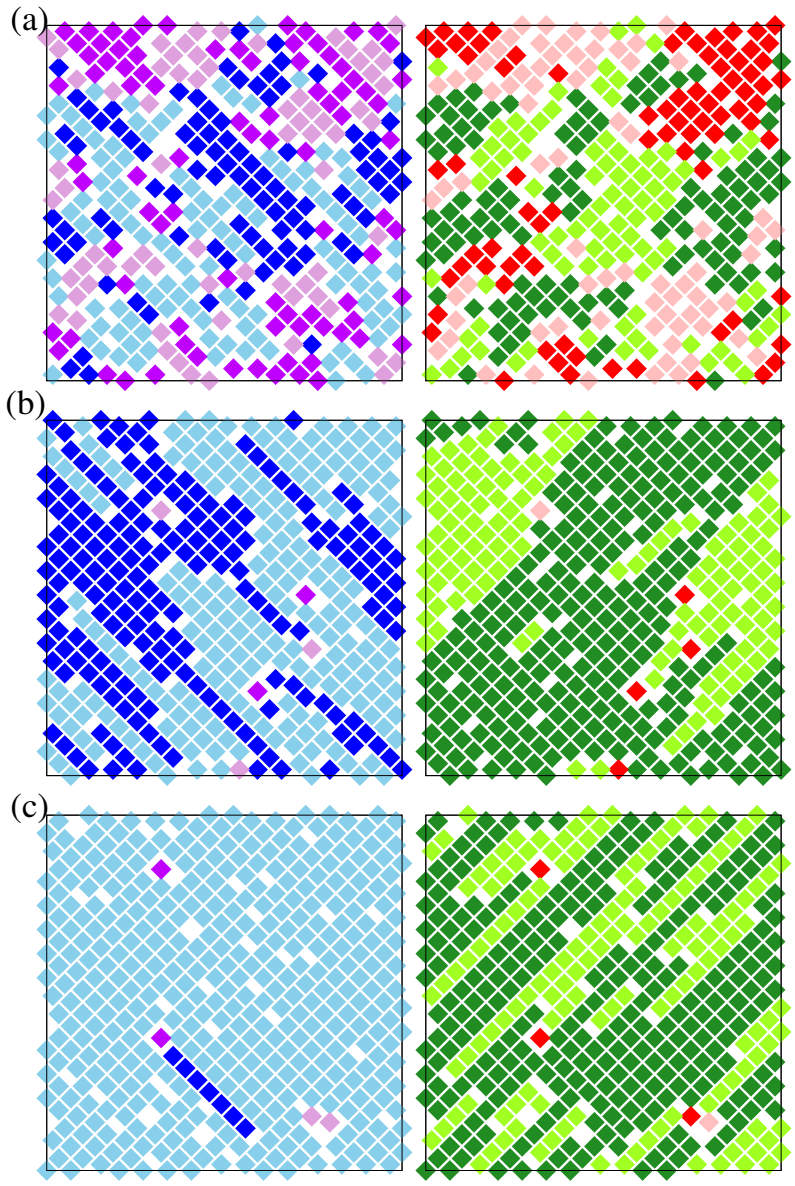

Figure 3.3: Snapshots of typical configurations of the 4-NN model. The particles are colored according to the sublattice it belongs to (see Fig. 3.2). In the left panel, the colors are light blue for 0, dark magenta for 1, deep blue for 2 and plum for 3. In the right panel, the colors are dark green for 4, red for 5, light green for 6 and pink for 7. (a) Low density disordered phase where all four colors are present in both panels. (b) Intermediate density sublattice phase, where even or odd sublattices are preferentially occupied. (c) High density columnar phase, where one sublattice in one of the panels (left in figure) and two sublattices in the other panel are preferentially occupied.

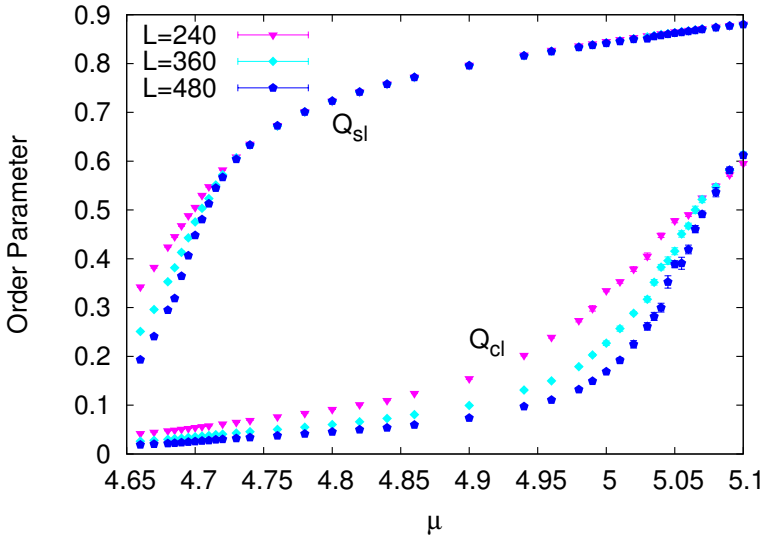

Figure 3.4: The variation of the order parameters Q_{sl} and Q_{cl} with chemical potential μ for different system sizes L. Q_{sl} becomes non-zero at a smaller value of μ than Q_{cl}.

0. However, in the right panel, particles occupy mostly two sublattices (4 and 6). This phase is identical to the high density phase of the hard square model (2-NN) where there is positional order in one direction but no positional order in the perpendicular direction due to a sliding instability. We call this phase the columnar phase. There are 8 such states, corresponding to the number of sublattices.

To distinguish between phases quantitatively, we define two order parameters Q_{sl} and Q_{cl}, where sl denotes sublattice and cl denotes columnar. Let ρ_i, $i = 0, \ldots, 7$ be the density of particles in sublattice i. We define

$$Q_{sl} = |(\rho_0 + \rho_2) - (\rho_1 + \rho_3)|, \tag{3.1a}$$

$$Q_{cl} = |\sum_{k=0}^{3} \rho_k e^{ik\pi/2}| - |\sum_{k=4}^{7} \rho_k e^{ik\pi/2}|. \tag{3.1b}$$

Q_{sl} measures the difference between the densities of sublattices A (sites in even sublattices) and B (sites in odd sublattices). It is zero in the disordered phase and non-zero in both the sublattice and columnar phases. Q_{cl} is zero in both the disordered and sublattice phases and non-zero only in the columnar phase.

While the snapshots in Fig. 3.3 are indicative of two transitions, we now show unambiguously the existence of two transitions. Figure 3.4 shows the variation of the two order parameters with chemical potential. Clearly, Q_{sl} takes on a L independent non-zero value when the chemical potential is larger than $\mu \approx 4.70$ ($\rho \approx 0.110$). At this value of μ Q_{cl} is still zero. Q_{cl} takes on a L independent non-zero value when the chemical potential is larger than $\mu \approx 5.07$ ($\rho \approx 0.116$). The two values of μ being clearly different, we conclude that there are two transitions.

The other thermodynamic quantities of interest are the susceptibility χ, the second moment of the order parameter $\chi^{(2)}$, the Binder cumulant U, and compressibility κ, defined as

$$\chi = L^2[\langle Q^2\rangle - \langle Q\rangle^2], \tag{3.2a}$$

$$\chi^{(2)} = L^2\langle Q\rangle^2, \tag{3.2b}$$

$$U = 1 - \frac{\langle Q^4\rangle}{3\langle Q^2\rangle^2}, \tag{3.2c}$$

$$\kappa = L^2[\langle \rho^2\rangle - \langle \rho\rangle^2], \tag{3.2d}$$

where Q represent Q_{sl} or Q_{cl}. Though χ and $\chi^{(2)}$ resemble each other, we find that the data for $\chi^{(2)}$ is much cleaner. The nature of the phase transitions is determined by the singular behaviour of U, Q, χ, and $\chi^{(2)}$ near the critical point. Let $\epsilon = (\mu - \mu_c)/\mu_c$, where μ_c is the critical chemical potential. The singular behaviour is characterized by the critical exponents ν, β, γ, and α defined by $Q \sim (-\epsilon)^\beta$, $\epsilon < 0$, $\chi \sim |\epsilon|^{-\gamma}$, $\chi^{(2)} \sim |\epsilon|^{-\gamma}$, $\kappa \sim |\epsilon|^{-\alpha}$and $\xi \sim |\epsilon|^{-\nu}$, where ξ is the correlation length and $|\epsilon| \to 0$. The other critical exponents may be obtained from scaling relations. The exponents are obtained by finite size scaling of

the different quantities near the critical point:

$$U \simeq f_U(\epsilon L^{1/\nu}), \tag{3.3a}$$

$$Q \simeq L^{-\beta/\nu} f_Q(\epsilon L^{1/\nu}), \tag{3.3b}$$

$$\chi \simeq L^{\gamma/\nu} f_\chi(\epsilon L^{1/\nu}), \tag{3.3c}$$

$$\chi^{(2)} \simeq L^{\gamma/\nu} f_\chi^{(2)}(\epsilon L^{1/\nu}), \tag{3.3d}$$

$$\kappa \simeq L^{\alpha/\nu} f_\kappa(\epsilon L^{1/\nu}), \tag{3.3e}$$

where f_U, f_Q, f_χ, $f_\chi^{(2)}$, f_κ are scaling functions and the system size is $L \times L$. In addition, if χ has a maximum $\chi_{max}(L)$ at $\mu_c(L)$, then

$$\chi_{max}(L) \propto L^{\gamma/\nu}, \tag{3.4a}$$

$$\mu_c(L) - \mu_c(\infty) \propto L^{-1/\nu}. \tag{3.4b}$$

The first transition from disordered to sublattice phase was studied in Ref. [9] using system sizes varying from $L = 80$ to $L = 240$, and was argued to be in the Ising universality class. However, analysis of the cluster integrals predict non-Ising exponents [15].

We re-examine this transition with data for system sizes up to $L = 600$. In addition to obtaining better estimates of the critical exponents, it also acts as a check for our Monte Carlo algorithm. The data for the different thermodynamic quantities near the disordered-sublattice transition are shown in Figs. 3.5 and 3.6 . The critical chemical potential μ_c is obtained from the intersection of the curves for the Binder cumulant U_{sl} for different system sizes. The intersection point depends very weakly on L [see Fig. 3.5(a)] allowing for an accurate determination of μ_c. We thus obtain $\mu_c = 4.705 \pm 0.005$, consistent with the μ_c found in Ref. [9]. At the critical point, we find the value of the Binder cumulant to lie between 0.606 and 0.619, consistent with the value 0.61.. for the two dimensional Ising

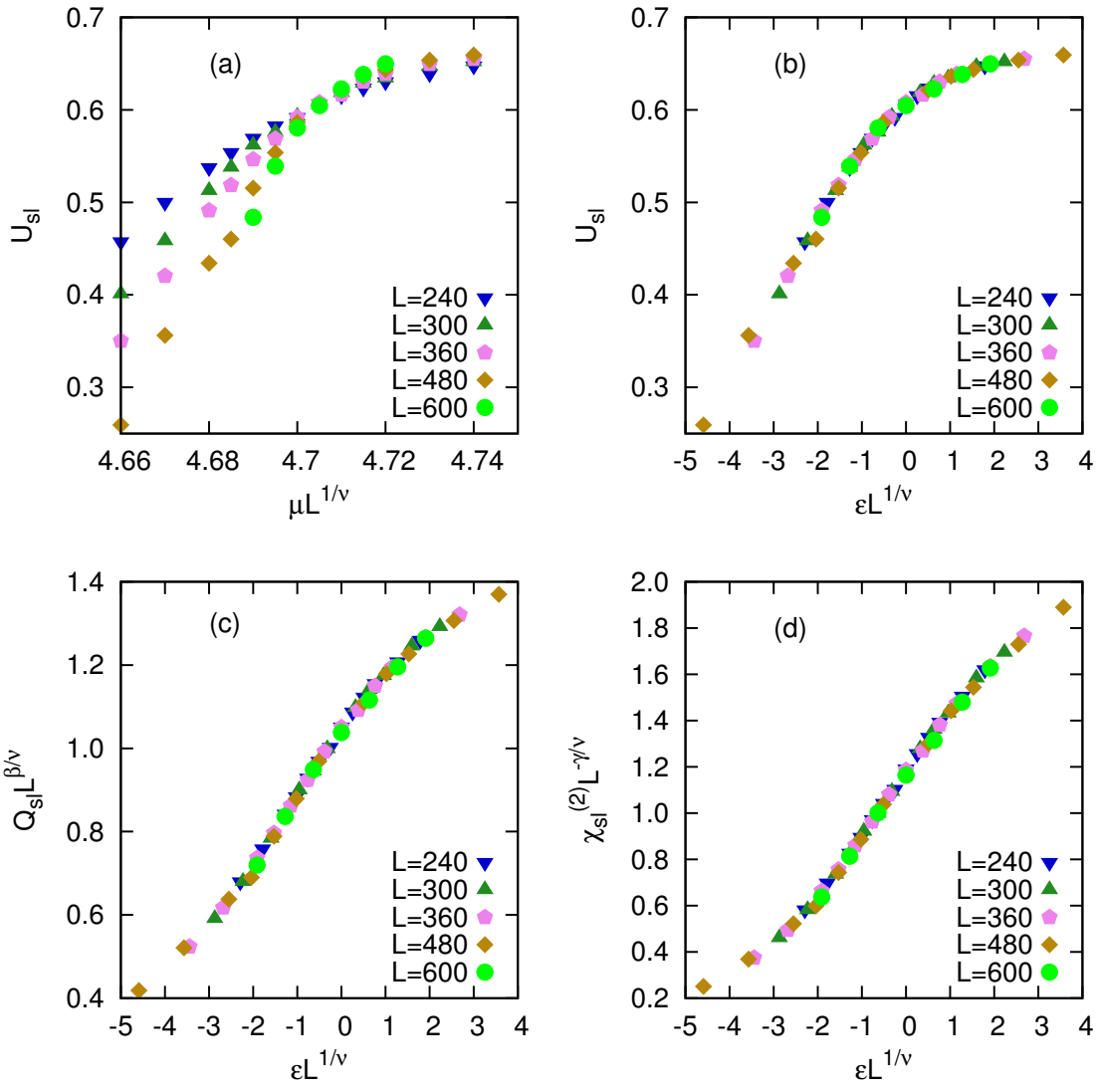

Figure 3.5: The data for cumulants of Q_{sl} for the 4-NN model near the first transition from the disordered phase to sublattice phase. (a) The Binder cumulant U_{sl} for different L intersect at $\mu_c = 4.705$. The data for (b) U_{sl}, (c) Q_{sl}, and (d) $\chi^{(2)}_{sl}$ for different L collapse onto a single curve when scaled as in Eq. (3.3) with the Ising exponents $\beta/\nu = 1/8$, $\gamma/\nu = 7/4$, and $\nu = 1$.

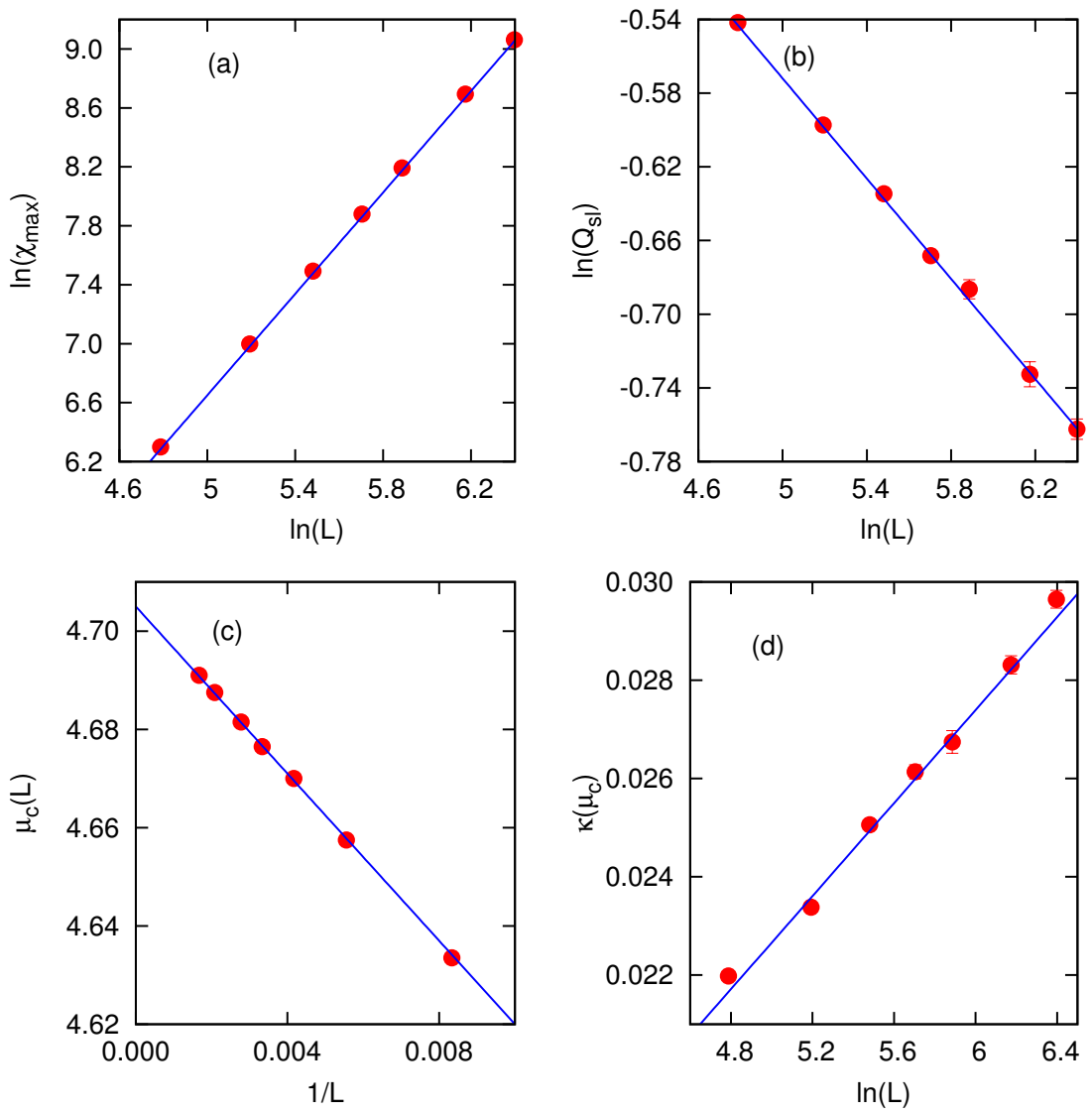

Figure 3.6: The data for cumulants of Q_{sl} for the 4-NN model near the first transition from the disordered phase to sublattice phase. (a) The variation of the maximum value χ_{max} of the susceptibility χ with L. The solid line is a best fit to the data with slope $\gamma/\nu = 1.72 \pm 0.04$. (b) The variation of the order parameter Q_{sl} at the critical point with L. The solid line is a best fit to the data with slope $-\beta/\nu = -0.136 \pm 0.017$. (c) Variation of μ_c for different L with $1/L$. The straight line intersects the μ-axis at $\mu_c = 4.705 \pm 0.005$. (d) The variation of the compressibility κ at the critical point with L. The straight line shows $\kappa(\mu_c) \sim \ln L$.

model. In the disordered-sublattice transition, the system breaks the symmetry between A and B sublattices. Due to the two-fold symmetry, we expect this transition to be in universality class of the two dimensional Ising model. Indeed, we find excellent data collapse when the data for U_{sl} [see Fig. 3.5(b)], Q_{sl} [see Fig. 3.5(c)] and $\chi^{(2)}_{sl}$ [see Fig. 3.5(d)] are scaled as in Eq. (3.3) with Ising exponents $\beta/\nu = 1/8$, $\gamma/\nu = 7/4$ and $\nu = 1$.

We also estimate β/ν and γ/ν independently. The maximum value of susceptibility χ_{max} scales with L as $L^{\gamma/\nu}$. We calculate χ_{max} by the method of histogram re-weighting, and obtain $\gamma/\nu = 1.72 \pm 0.04$ [Fig. 3.6(a)]. The order parameter Q_{sl} at the critical point decreases with L as $L^{-\beta/\nu}$. By simulating for different L, we obtain $\beta/\nu = 0.136 \pm 0.017$ [see Fig. 3.6(b)]. Both these numerical values are consistent with the Ising exponents. In Fig. 3.6(c), we show the variation of $\mu_c(L)$ with $1/L$. The data lie on a straight line, consistent with $\nu = 1$. The intersection of the straight line with the μ-axis gives $\mu_c = 4.705 \pm 0.005$, consistent with the estimation from the crossing of the curves for the Binder cumulant. Finally, we examine the data for compressibility κ at the critical point. The data for compressibility is more noisy that that for other quantities, but is consistent with a logarithmic divergence with L [see Fig. 3.6(d)], as expected for the Ising universality class. Thus, we conclude, as in Ref. [9] and contrary to the conclusion in Ref. [15], that the transition from disordered to sublattice phase is in the Ising universality class,

We now focus on the second transition from the sublattice phase to the columnar phase. Suppose, in the sublattice phase, the system is in sublattice A. This corresponds to all sites belonging to sublattices $0, 2, 4, 6$. In the second transition, the system picks out one of the four sublattices, with equal occupation of two other sublattices. Since this transition breaks a four fold symmetry, we expect this transition, if continuous, to be in the universality class of the two color Ashkin Teller model. We, thus, expect $\gamma/\nu = 7/4$, $\beta/\nu = 1/8$, and ν depending on the parameters of the problem at hand [186]. We now provide numerical evidence of the same.

The data for the different thermodynamic quantities for the second transition are shown

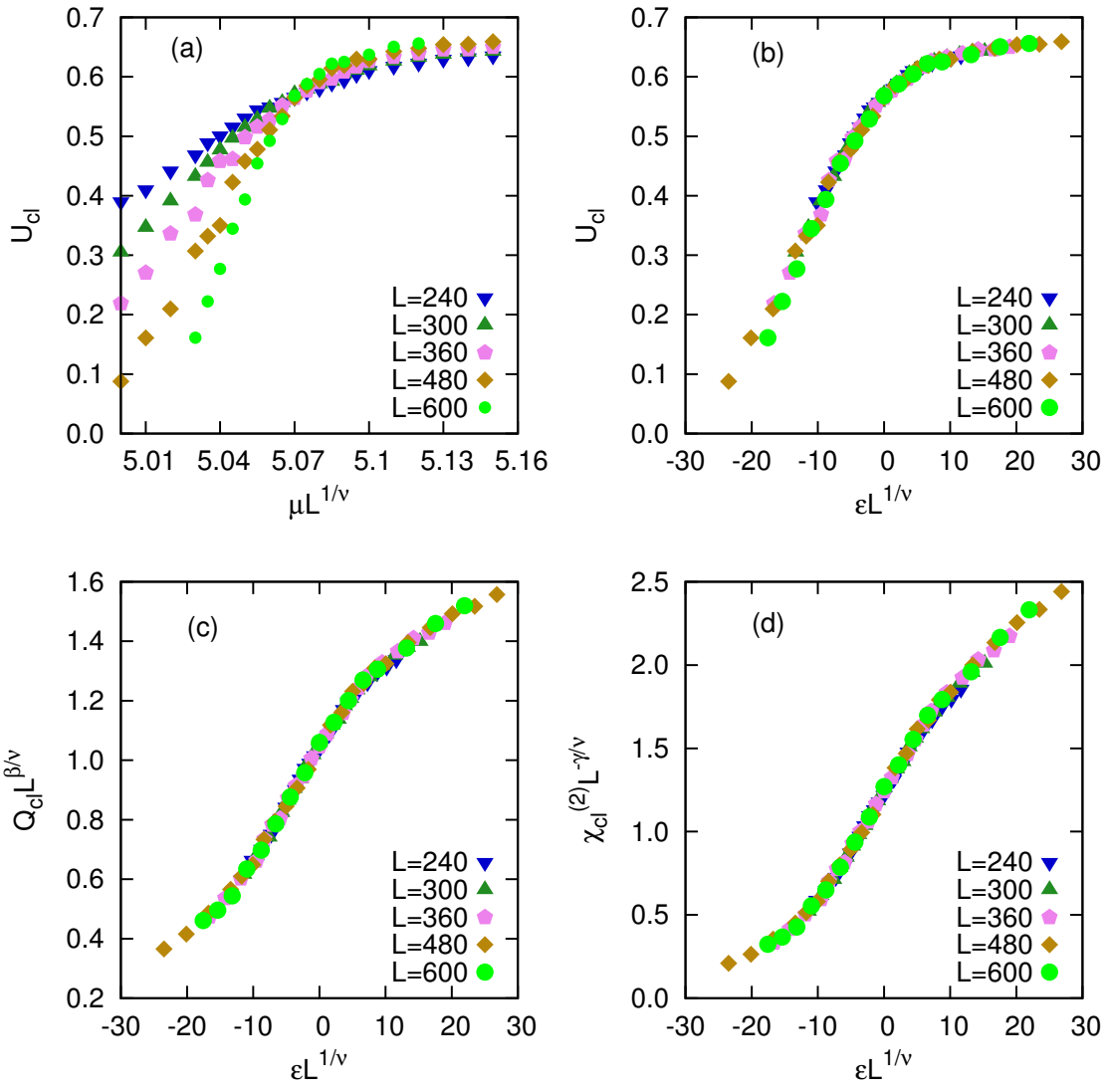

Figure 3.7: The data for cumulants of Q_{cl} for the 4-NN model near the second transition from the sublattice phase to the columnar phase. (a) The Binder cumulant U_{cl} for different L intersect at $\mu_c = 5.07 \pm 0.01$. The data for (b) U_{cl}, (c) Q_{sl} and (d) $\chi^{(2)}_{sl}$ for different L collapse onto a single curve when scaled as in Eq. (3.3) with critical exponents $\beta/\nu = 1/8$, $\gamma/\nu = 7/4$ and $\nu = 0.83 \pm 0.06$.

in Figs. 3.7 and 3.8. From the intersection of the curves of U_{cl} for different L [see Fig. 3.7(a)], we obtain $\mu_c = 5.07 \pm 0.01$. At the transition point, the Binder cumulant has value ≈ 0.56, clearly different from the value 0.61.. for the two dimensional Ising model. The Binder cumulant data for different system sizes collapse onto a single curve when scaled as in Eq. (3.3a) with $\nu = 0.083 \pm 0.06$ [see Fig. 3.7(b)]. For this value of ν and $\gamma/\nu = 7/4$, $\beta/\nu = 1/8$, we obtain excellent data collapse for Q_{sl} [see Fig. 3.7(c)] and $\chi^{(2)}_{sl}$ [see Fig. 3.7(d)] when scaled as in Eq. (3.3b) and Eq. (3.3c) respectively. Thus, we conclude that the transition belongs to the Ashkin Teller universality class with $\nu = 0.83 \pm 0.06$, lying between the 4 state Potts and Ising points. Independent measurement of γ/ν from the variation of the maximum of susceptibility with L gives $\gamma/\nu = 1.76 \pm 0.05$ [see Fig. 3.8(a)]. Similarly, from the dependence of Q_{sl} on L at the critical point, we obtain $\beta/\nu = 0.113 \pm 0.015$ [see Fig. 3.8(b)]. Both these values are consistent with the Ashkin Teller universality class. In Fig. 3.8(c), we show the dependence of the critical chemical potential $\mu_c(L)$ on L. When plotted against $L^{-1/\nu}$ [see Eq. (3.4b)], with $\nu = 0.83$, the data lie on a straight line which intersects the μ-axis at $\mu_c = 5.066 \pm 0.01$. This estimate of the critical μ is consistent with the value obtained from the intersection of the curves for the Binder cumulants. Since $\nu < 1$, the exponent $\alpha > 0$ and we expect the compressibility κ to diverge at the critical point with exponent α/ν. The data for κ is very noisy [see Fig. 3.8(d)] when compared to data for other thermodynamic quantities. Fitting to a power law, we obtain $\alpha/\nu = 0.34 \pm 0.08$. Within error bars, α/ν satisfies the exponent equality $2\nu = 2 - \alpha$.

We conclude that the 4-NN model, contrary to what was known earlier, undergoes two entropy driven transitions with increasing density. In order to provide some understanding of this phenomena, we derive the high density expansion of the model in the next section.

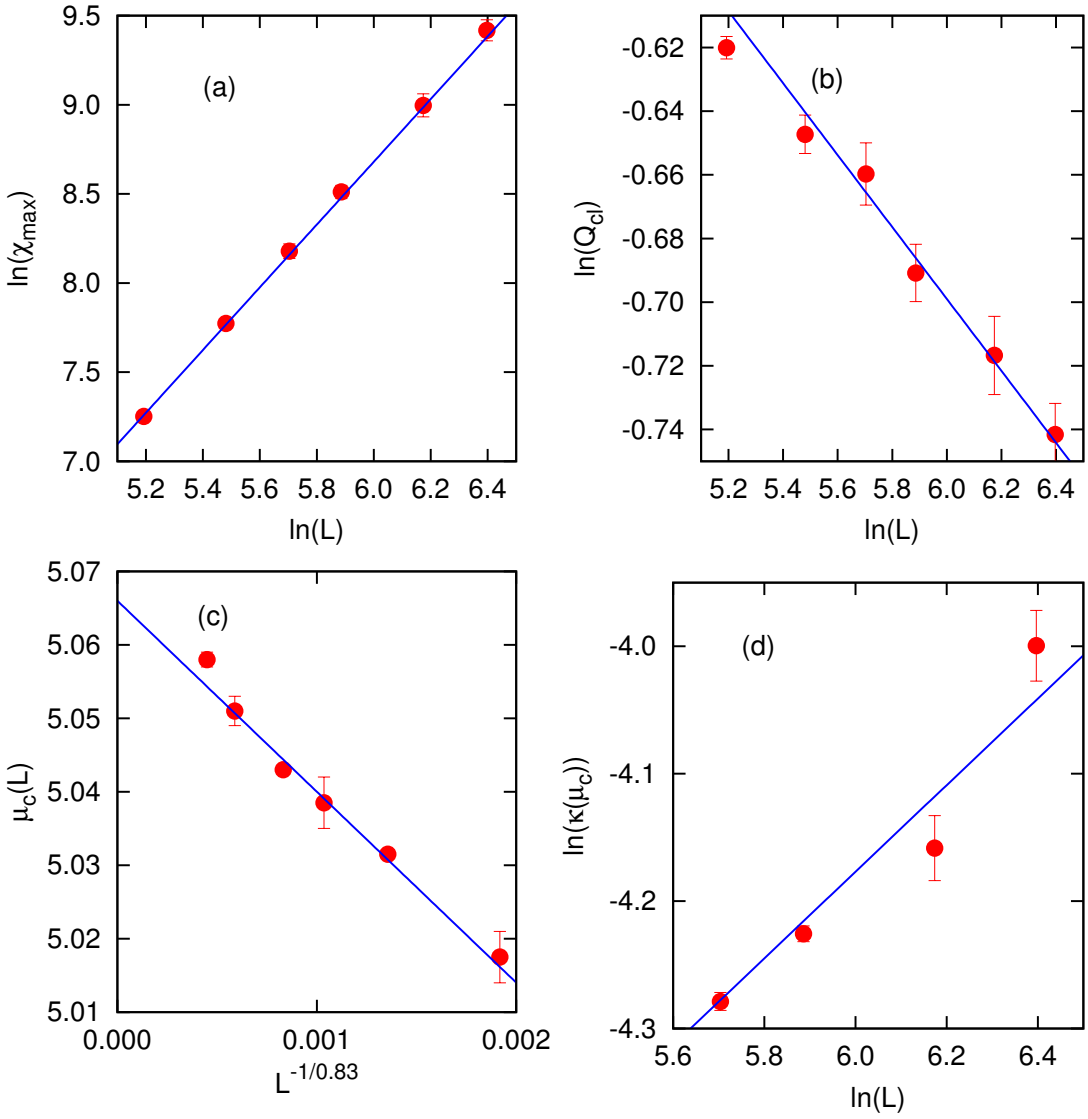

Figure 3.8: The data for cumulants of Q_{cl} for the 4-NN model near the second transition from the sublattice phase to the columnar phase. (a) The variation of the maximum value χ_{max} of the susceptibility χ with L. The solid line is a best fit to the data with slope $\gamma/\nu = 1.76 \pm 0.05$. (b) The variation of the order parameter Q_{sl} at the critical point with L. The solid line is a best fit to the data with slope $-\beta/\nu = -0.113 \pm 0.015$. (c) Variation of μ_c for different L with $L^{-1/\nu}$. The straight line intersects μ-axis at $\mu_c = 5.066 \pm 0.01$. (d) The variation of compressibility κ at the critical point μ_c with L. The solid line is a best fit to the data with slope $\alpha/\nu = -0.34 \pm 0.08$.

3.3 High density expansion of the 4-NN model

In this section, we calculate the first four terms in the large z (high density) expansion of the free energy for the 4-NN model. We show that the high density phase (say all particles in mostly sublattice 0) has a sliding instability only for defects in sublattice 2 and not for defects in sublattices 1 and 3. This results in the densities of defects in the different sublattices being different at large z. We argue that this sliding instability could be the origin of the two phase transitions in the 4-NN model.

The high density phase of the 4-NN model being columnar, the high density expansion is very similar to that for the 2-NN model [11, 19]. Due to the sliding instability, the large z expansion of the 2-NN model is in powers of $1/\sqrt{z}$ instead of the usual $1/z$ Mayer series. The first three terms in the high density expansion for the 2-NN model was obtained in Ref. [11]. More recently, it has been systematically extended to 4 terms [19]. We will closely follow the calculations of Ref. [19], modifying when necessary for the 4-NN model.

Consider a fully packed configuration of the 4-NN model. It has density $1/8$. If the particles occupy one of the sublattice from 0 to 3, then they occupy two sublattices from 4 to 7 and vice-versa (see Fig. 3.2 for labeling of sublattices). For example, if the particles are all in sublattice 0, then they are also simultaneously in sublattices 4 and 6. It is easy to see that the number of fully packed configurations is $8(2^{L/2} - 1)$, where we assume that L is even. Though the degeneracy diverges with L, the entropy per unit site is zero in the thermodynamic limit.

For constructing the large z expansion, we will describe the lattice sites only in terms of sublattices 0 to 3. Let the activities on sublattice i be z_i. We will consider $z_0 \gg z_i$, $i = 1, 2, 3$. After the expansion is obtained, we will equate all the activities to z. Thus, it will be an expansion about an ordered state where all the particles are in sublattice 0. The

free energy $f(z_0, z_1, z_2, z_3)$ is defined as

$$f(z_0, z_1, z_2, z_3) = \lim_{N\to\infty} \frac{-1}{N} \ln \mathcal{L}(z_0, z_1, z_2, z_3), \tag{3.5}$$

where $\mathcal{L}(z_0, z_1, z_2, z_3)$ is the grand canonical partition function. To lowest order, the contribution to the partition function is $\mathcal{L}(z_0, 0, 0, 0)$. It is easy to see that the partition function breaks up into a product of one dimensional partition functions, and is

$$\mathcal{L}(z_0, 0, 0, 0) = \Omega_p(z_0, L)^{L/4}. \tag{3.6}$$

Here $\Omega_p(z, \ell)$ and $\Omega_o(z, \ell)$ are the partition functions of a nearest neighbor exclusion hard core gas on a one dimensional lattice of length ℓ with periodic and open boundary conditions respectively, as defined in Eq. (2.1) with $d = 1$.

Solving Eq. (2.1), we obtain [11, 19]

$$\Omega_o(z, \ell) = \frac{\lambda_+^{\ell+2} - \lambda_-^{\ell+2}}{\sqrt{1+4z}}, \ \ell = 0, 1, \ldots, \tag{3.7}$$

$$\Omega_p(z, \ell) = \lambda_+^{\ell} + \lambda_-^{\ell}, \ \ell = 2, 3, \ldots, \tag{3.8}$$

where

$$\lambda_\pm = \frac{1 \pm \sqrt{1+4z}}{2}. \tag{3.9}$$

Knowing the partition functions, the contribution from configurations with zero defects (all particles in sublattice 0) to the free energy is

$$f(z_0, 0, 0, 0) = \frac{-\ln z_0}{8} - \frac{1}{8\sqrt{z_0}} + \frac{1}{192 z_0^{3/2}} + O(\frac{1}{z_0^{5/2}}). \tag{3.10}$$

We now switch on z_1. This creates some defect sites in sublattice 1. We first calculate the contribution from configurations with a single defect. A single defect on sublattice 1 excludes 4 sites from the diagonal of sublattice 0 closest to it and 2 sites from the diagonal

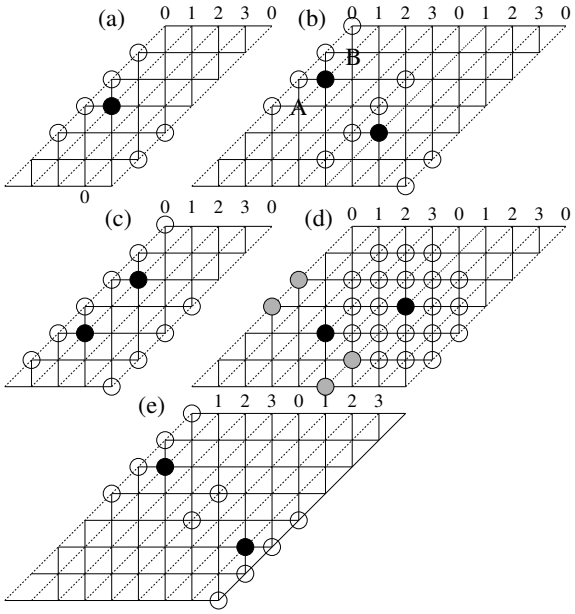

Figure 3.9: Examples of one and two defect configurations on sublattices 1 and 3 for an ordered state where particles are on sublattice 0. Black circles are particles, empty and lightly shaded circles are excluded sites. Exclusions only on sublattice 0 are shown in (a)–(c) and (e). $0, 1, 2, 3$ denote the diagonals that belong to sublattices $0, 1, 2, 3$. (a) A single defect on sublattice 1. (b) Two defects on sublattice 1 but on neighboring diagonals. A and B are two other lattice sites where the defect may be placed. (c) Two defects on sublattice 1 but on the same diagonal. (d) A defect on sublattice 1 and a defect on sublattice 3 at one of the 4 closest positions. The empty circles are all the excluded sites due to defect on sublattice 1 while the lightly shaded circles are excluded sites on sublattice 0 due to defect on sublattice 3. (e) A defect on sublattice 1 and a defect on sublattice 3 positioned such that they exclude the same two sites on the diagonal 0 separating them.

further away from it [see Fig. 3.9(a)]. The contribution of configurations with one defect to the partition function is

$$\left.\frac{\mathcal{L}(z_0, z_1, 0, 0)}{\mathcal{L}(z_0, 0, 0, 0)}\right|_{1D} = \frac{N z_1}{4} \frac{\Omega_o(z_0, L-4)\Omega_o(z_0, L-2)}{\Omega_p(z_0, L)^2}, \tag{3.11}$$

where the factor $N/4$ is the number of ways of placing a particle on sublattice 1, and $1D$ denotes one defect. Expanding for large z_0, we obtain

$$\left.\frac{\mathcal{L}(z_0, z_1, 0, 0)}{\mathcal{L}(z_0, 0, 0, 0)}\right|_{1D} = N z_1 \left[\frac{1}{16 z_0^2} - \frac{1}{16 z_0^{5/2}} + O(z_0^{-3})\right]. \tag{3.12}$$

We now consider the contribution from configurations with two defects on sublattice 1. The lowest order contributions come from the two defects being on the same diagonal or on adjacent diagonals. First consider two defects on adjacent diagonals, as shown in Fig. 3.9(b). Now, 4, 4 and 2 lattice sites are excluded from diagonals belonging to sublattice 0. The ratio of the partition functions with $z_1 \neq 0$ and $z_1 = 0$ for this configuration with two defects is

$$\frac{3Nz_1^2}{4}\frac{\Omega_o(z_0, L-4)^2\Omega_o(z_0, L-2)}{\Omega_p(z_0, L)^3}, \tag{3.13}$$

where the factor $3N/4$ is the combinatorial factor associated with the number of ways of placing the pair of particles. For each choice of the position of the first particle ($N/4$ ways), there are 3 ways of placing the second particle (A, B, and filled circle). Expanding for large z_0, we obtain

$$Nz_1^2\left[\frac{3}{32z_0^{7/2}} + O(z_0^{-4})\right]. \tag{3.14}$$

Second, consider the case when two defects are on sublattice 1 but on the same diagonal, as shown in Fig. 3.9(c). Now, 6 and 4 lattice sites are excluded from diagonals belonging to sublattice 0. The ratio of the partition functions for this two defect configuration is

$$\frac{Nz_1^2}{4}\frac{\Omega_o(z_0, L-6)\Omega_o(z_0, L-4)}{\Omega_p(z_0, L)^2}, \tag{3.15}$$

where the factor $N/4$ is the combinatorial factor associated with the number of ways of placing the pair of particles. Expanding for large z_0, we obtain

$$Nz_1^2 O(z_0^{-4}). \tag{3.16}$$

Thus, to order $z^{-3/2}$, there is no contribution. Collecting together the terms, we obtain

$$\left.\frac{\mathcal{L}(z_0, z_1, 0, 0)}{\mathcal{L}(z_0, 0, 0, 0)}\right|_{2D} = Nz_1^2\left[\frac{3}{32z_0^{7/2}} + O(z_0^{-3})\right]. \tag{3.17}$$

It is straightforward to verify that the contribution from configurations with 3 defects do

not contribute to terms up to order $z^{-3/2}$.

We now switch on a small z_3. Sublattices 1 and 3 being symmetric with respect to sublattice 0, the contribution from configurations with a single defect on sublattice 3 is identical to Eq. (3.12) except for $z_1 \to z_3$. Similarly, configurations with two defects on sublattice 3 have the same contribution as Eq. (3.17) with $z_1 \to z_3$. We now calculate the contribution to the partition function from configurations with one defect on sublattice 1 and another on sublattice 3 as shown in Fig. 3.9(d) and (e). In Fig. 3.9(d), the particles are placed as close to each other as possible. Given a particle on sublattice 1 (placed in $N/4$ ways), there are four ways of placing a particle on sublattice 3. The ratio of the partition functions for this two defect configuration is

$$N z_1 z_3 \frac{\Omega_o(z_0, L-2)^2 \Omega_o(z_0, L-6)}{\Omega_p(z_0, L)^3}. \tag{3.18}$$

Expanding for large z_0, we obtain

$$N z_1 z_3 \left[\frac{1}{8 z_0^{7/2}} + O(z_0^{-4}) \right]. \tag{3.19}$$

Now, consider the configuration shown in Fig. 3.9(e). Once the first particle is placed (in $N/4$ ways), there is a unique position for the second particle. The ratio of partition functions when two such defects are present is

$$\frac{N z_1 z_3}{4} \frac{\Omega_o(z_0, L-4)^2 \Omega_o(z_0, L-2)}{\Omega_p(z_0, L)^3}. \tag{3.20}$$

Expanding for large z_0, we obtain

$$N z_1 z_3 \left[\frac{1}{32 z_0^{7/2}} + O(z_0^{-4}) \right]. \tag{3.21}$$

Combining together the contributions from configurations with one or two defects on

sublattices 1 and 3, we obtain

$$\frac{\mathcal{L}(z_0,z_1,0,z_3)}{\mathcal{L}(z_0,0,0,0)} = N(z_1+z_3)\left[\frac{1}{16z_0^2}-\frac{1}{16z_0^{5/2}}\right] + \frac{3N(z_1^2+z_3^2)}{32z_0^{7/2}} + \frac{5Nz_1z_3}{32z_0^{7/2}} + O(z^{-2}). \tag{3.22}$$

We now focus on defects in sublattice 2. Unlike defects in sublattices 1 and 3, a vacancy on sublattice 0 can be broken into two half vacancies with the points in between being defects on sublattice 2. Thus, n defects on sublattice 2 contribute at the same order as a single defect [19]. The expansion is better performed in terms of rods which are a collection of contiguous defects in the $3\pi/4$ direction on sublattice 2 [19]. An example of a rod of length 3 is shown in Fig. 3.10 (focus only on black circles and empty circles that are triplets). It excludes three sites each from 4 diagonals belonging to sublattice 0. It is straightforward to obtain the contribution from a single rod [19]:

$$\left.\frac{\mathcal{L}(z_0,0,z_2,0)}{\mathcal{L}(z_0,0,0,0)}\right|_{1R} = \frac{N}{4}\sum_{n=1}^{\infty} z_2^n\left[\frac{\Omega_o(z_0,L-3)}{\Omega_p(z_0,L)}\right]^{n+1}, \tag{3.23a}$$

$$= \frac{N}{4}\frac{z_2\beta^2}{1-z_2\beta}, \tag{3.23b}$$

where $1R$ denoted one rod and

$$\beta = \frac{1}{\sqrt{1+4z_0}\lambda_+}, \tag{3.24}$$

is a function only of z_0.

The calculation of the contribution from two rods on sublattice 2 is identical to that for the 2-NN model, except for an overall factor of $1/2$ due to only half the lattice sites being involved in the calculation. Thus, one can read off the results from the calculations of Ref. [19] for the 2-NN model.

A further contribution to the free energy at order $z^{-3/2}$ is due to configurations with a rod on sublattice 2 and a particle on sublattice 1 or 3. Given a rod on sublattice 2, there

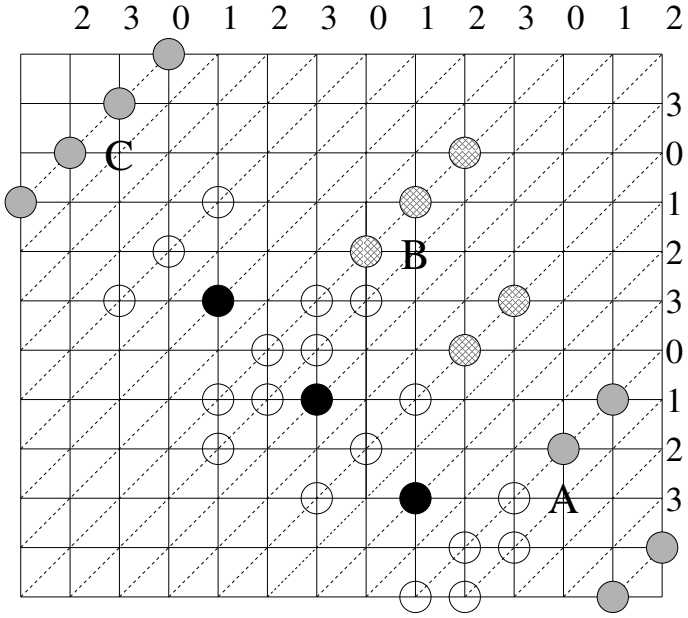

Figure 3.10: Example of a rod-like defect on sublattice 2 and defects on sublattice 1. Black circles are particles on sublattice 2. Empty circles are excluded sites on sublattice 0 or sublattice 1 (all not shown) due to defect on sublattice 2. Lightly shaded circles are excluded sites due to defects at A or C. Circles with a pattern are excluded sites due to defect at B.

are three kinds of sites on sublattice 1 where a particle may be placed. These are denoted by A, B and C (see Fig. 3.10). The contribution to the ratios of partition functions $\mathcal{L}(z_0, z_1, z_2, 0)/\mathcal{L}(z_0, 0, 0, 0)$ for the different cases are

$$A \;:\; \frac{N}{4} z_2^n \left[\frac{\Omega_o(z_0, L-3)}{\Omega_p(z_0, L)}\right]^n \times 2z_1 \frac{\Omega_o(z_0, L-5)\Omega_o(z_0, L-2)}{\Omega_p(z_0, L)^2} \sim O(z^{-3/2}), \tag{3.25}$$

$$B \;:\; \frac{N}{4} z_2^n \left[\frac{\Omega_o(z_0, L-3)}{\Omega_p(z_0, L)}\right]^{n-1} \times 2nz_1 \frac{\Omega_o(z_0, L-6)\Omega_o(z_0, L-5)}{\Omega_p(z_0, L)^2} \sim O(z^{-5/2}), \tag{3.26}$$

$$C \;:\; \frac{N}{4} z_2^n \left[\frac{\Omega_o(z_0, L-3)}{\Omega_p(z_0, L)}\right]^n \times 2z_1 \frac{\Omega_o(z_0, L-4)}{\Omega_p(z_0, L)} \sim O(z^{-3/2}), \tag{3.27}$$

where n is the length of the rod. Thus to order $z^{-3/2}$, only cases A and C are relevant, and

their contribution to the free energy add up to

$$\left.\frac{\mathcal{L}(z_0,z_1,z_2,z_3)}{\mathcal{L}(z_0,0,0,0)}\right|_{1R,1D} = \frac{N}{4}\frac{z_2\beta}{1-z_2\beta}\frac{(z_1+z_3)}{2z_0^{5/2}} + \frac{N}{4}\frac{z_2\beta^2}{1-z_2\beta}\frac{(z_1+z_3)}{z_0^{3/2}} + O(z^{-2}), \tag{3.28}$$

where, in the right hand side of Eq. (3.28), the first term is due to A and the second term is due to C.

The free energy of the 4-NN model may now be written down up to $O(z^{-3/2})$. In terms of the partition functions,

$$f(z_0,z_1,z_2,z_3) = -\frac{\ln \mathcal{L}(z_0,0,0,0)}{N} - \frac{\mathcal{L}(z_0,z_1,z_2,z_3)}{N\mathcal{L}(z_0,0,0,0)}. \tag{3.29}$$

Adding the contribution from configurations with two rods, as obtained in Ref. [19], to Eqs. (3.10), (3.22), (3.23b), and (3.28), and equating $z_i = z$, we obtain

$$-f(z) = \frac{1}{8}\ln z + \frac{1}{8z^{1/2}} + \frac{1}{4z} + \frac{\frac{3}{2}\ln\frac{9}{8} + \frac{149}{192}}{z^{3/2}} + O(z^{-2}). \tag{3.30}$$

Knowing the free energy, the particle densities in each sublattice is given by $\rho_i = z_i\partial/\partial z_i(-f)$. Doing the algebra and simplifying,

$$\rho(z) = \frac{1}{8} - \frac{1}{16z^{1/2}} - \frac{1}{4z} - \frac{\frac{9}{4}\ln\frac{9}{8} + \frac{149}{128}}{z^{3/2}} + O(\frac{1}{z^2}), \tag{3.31}$$

$$\rho_0(z) = \frac{1}{8} - \frac{1}{16z^{1/2}} - \frac{5}{8z} - \frac{\frac{605}{128} + \frac{17}{4}\ln\frac{9}{8}}{z^{3/2}} + O(\frac{1}{z^2}), \tag{3.32}$$

$$\rho_1(z) = \frac{1}{16z} + \frac{17}{32z^{3/2}} + O(\frac{1}{z^2}), \tag{3.33}$$

$$\rho_2(z) = \frac{1}{4z} + \frac{2\ln\frac{9}{8} + \frac{5}{2}}{z^{3/2}} + O(\frac{1}{z^2}). \tag{3.34}$$

The sublattice densities, truncated at order $z^{-3/2}$ are plotted in Fig. 3.11. Clearly, due to

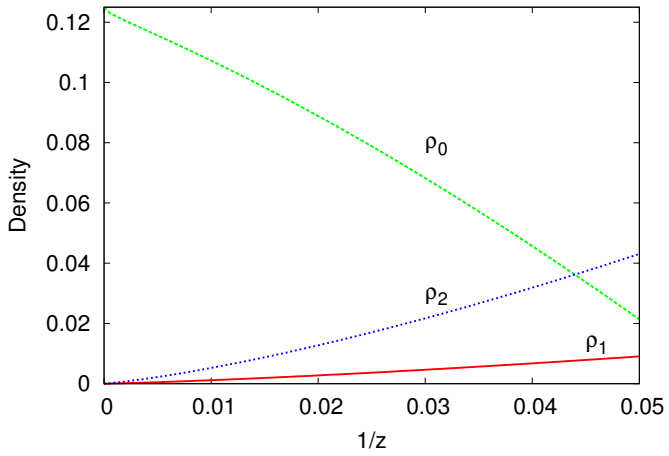

Figure 3.11: Variation of the densities of particles in different sublattices, truncated at order $z^{-3/2}$ [see Eqs. (3.32), (3.33), (3.34)], with $1/z$.

the sliding instability, the density on sublattice 2 increases faster than that of sublattices 1 and 3. Equating ρ_0 and ρ_2 in Eqs. (3.32) and (3.34), an estimate of the critical activity may be estimated. We find $z_c = 22.742\ldots$ or $\mu_c = 3.1242\ldots$. This should be compared with the actual value of $\mu_c \approx 5.07$.

The faster increase in the particle density of the sublattice where sliding instability exists is the likely reason for the second transition. As density is increased, the system is first destabilized by the sliding instability into sublattices 0 and 2. This is followed by a second transition where the density of sublattices 1, 3 equals that of 0, 2.

3.4 Discussion

In this chapter, we have studied the two-dimensional 4-NN hard core lattice gas model, where the first 4 next nearest neighbors of a particle are excluded from being occupied by another particle. The 4-NN model shows two transitions with increasing density–from low density disordered to high density columnar phase with an intermediate sublattice-ordered phase. The presence of two transitions resolved an existing puzzle as to why the system had a continuous transition when analogy with the Potts model predicts a first

order transition. In this chapter, we showed that the 8-fold symmetry is broken in two steps leading to two continuous transitions – one belonging to the Ising universality class and the other to the two color Ashkin Teller universality class – rather than a single first order transition. To rationalize this finding, we studied analytically the 4-NN model using a large z expansion. The high density phase being columnar, the expansion is in powers of $1/\sqrt{z}$ rather than the usual Mayer expansion in $1/z$. From the first four terms of the expansion, it was shown that the densities of defects increases more rapidly in sublattices where a sliding instability is present when compared to sublattices where it is absent.

For the 4-NN model, by simulating systems up to $L = 600$ (earlier simulations [9] having studied $L = 240$), we confirm that the first transition from the low density disordered phase to the intermediate sublattice phase is indistinguishable from the universality class of the two-dimensional Ising model. However, sophisticated analysis based on cluster integrals rule out Ising universality class [15]. This cluster analysis works very well for other repulsive interaction models and is a promising tool for studying phase transitions. It would therefore be important to understand why it fails for the 4-NN model. In particular should the analysis be modified in the presence of multiple transitions?

Chapter 4

k-NN model with $6 \leq k \leq 11$

4.1 Introduction

In this chapter, we generalize the arguments for the multiple transitions in the 4-NN model, based on the high density expansion, to larger k and conjecture a criteria for multiple transitions to be observed with increasing density. In particular, we argue that for a fixed k, if the high density phase is columnar but the sliding instability is not along all sublattices, then the system should undergo multiple transitions with increasing density. Applying this criteria to larger k, we argue that the HCLG with $k = 10, 11, 14, \ldots$ should undergo multiple transitions while $k = 6, 7, 8, 9$ should have a single first order transition.

In Sec. 4.2, the criteria of multiple transitions is conjectured for larger k. In Sec. 4.3, we present results from Monte Carlo simulations for $6 \leq k \leq 11$. It is shown that for $k = 6, 7, 8, 9$, there is a single first order transition. For $k = 10$, we show that there are two transitions– one continuous and the other first order. The exponents describing the continuous transition are shown to be consistent with those of the two dimensional Ising model. For $k = 11$, we show that there are at least two transitions with increasing density. Section 4.4 contains a discussion of the results. The content of this chapter is published in Ref. [179].

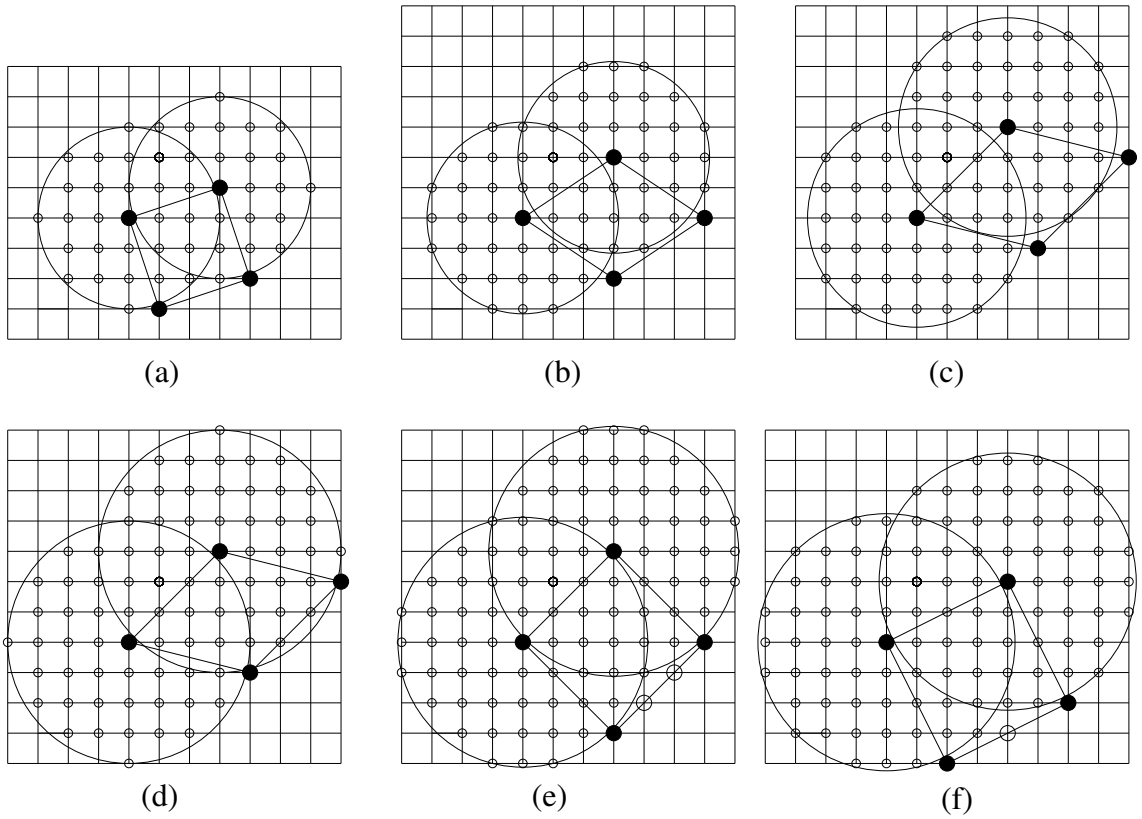

Figure 4.1: One of the configurations of maximum density for different k. Particles are shown by large filled circles. The excluded sites are shown by small circles. A circle that encloses the excluded sites due to a particle are drawn around the left most and top most particles. The empty large circles denote sites that may be occupied by sliding all particles on that diagonal, keeping other particles fixed. The examples are for (a) 6-NN, (b) 7-NN, (c) 8-NN, (d) 9-NN, (e) 10-NN, and (f) 11-NN.

4.2 Multiple transitions in the k-NN HCLG

In this section, we generalize the arguments of Sec. 3.3 to larger k. We ask for a criteria that will help determine whether the HCLG for a given k will undergo multiple transitions. From the analysis of the 4-NN model, it is clear that if the high density phase is columnar, then it is easier to generate defects in the sublattices where the sliding instability is present as compared to other sublattices. Hence, we conjecture that if the model satisfies (i) the high density phase is columnar and (ii) the sliding instability is present in only a fraction of the sublattices, then the system will show multiple transitions.

In hard square systems ($k = 2, 5$), though the high density phase is columnar, the sliding

instability is along all sublattices and hence does not satisfy condition (ii). Hence, one expects only one transition for the hard square system, at least for 2×2 and 3×3 systems. Models, other than hard square models, that show columnar order at high densities will typically have sliding instability in only a few sublattices. For $k > 5$, none of the k-NN HCLG models are hard square models. Thus, the criteria reduces to determining whether the high density phase is columnar or not.

The nature of the phase at high densities may be determined by constructing configurations at full packing for different k. In Fig. 4.1, we show configurations at full packing for $k = 6$ to 11. In each of the plots, 4 particles (filled circles) that constitute the unit cell are shown. A circle of radius R, which depends on k, is drawn around two of these particles – the left most and top most. R is distance of the farthest exclusion point from the particle hence all lattice sites within or on the circle are excluded by the particle. The value of R for different k is given in Table. 4.1. In all the cases, the configuration can be thought of as particles placed on equidistant parallel diagonals (not necessarily oriented in the $\pi/4$ direction). In some cases [see Fig. 4.1 (e) and (f)], all the particles in a diagonal may be slid by one or two lattice spacings without affecting the configurations in other diagonals. Such allowed sites are denoted by empty large circles. If such a freedom to slide exists, the system will have columnar order at high densities.

For 6-NN, in the fully packed configuration, the particles are along diagonals oriented in the $\tan^{-1}(1/3)$ or $\tan^{-1}(3)$ directions [see Fig. 4.1(a)]. There is no freedom to slide, and hence we expect sublattice order at full packing. This is true for $k = 7, 8, 9$, where the diagonals are oriented in different directions for different k [see Fig. 4.1(b)–(d)]. Thus, the conjecture would predict a single first order transition to an ordered sublattice phase for $k = 6, \ldots, 9$.

For the 10-NN model, the particles in any diagonal may be slid by one or two lattice sites in the $\pi/4$ direction without affecting the configurations in the other diagonals [see Fig. 4.1(e)]. For the 11-NN model, all the particles in a diagonal may be slid by one

Table 4.1: For each k, the square of radius of circle of exclusion R^2, density at full packing ρ_{max} and the nature of the high density phase are tabulated.

k	R^2	ρ_{max}	High density phase
1	1	1/2	Sublattice
2	2	1/4	Columnar
3	4	1/5	Sublattice
4	5	1/8	Columnar
5	8	1/9	Columnar
6	9	1/10	Sublattice
7	10	1/12	Sublattice
8	13	1/15	Sublattice
9	16	1/15	Sublattice
10	17	1/18	Columnar
11	18	1/20	Columnar
12	20	1/23	Sublattice
13	25	1/24	Sublattice
14	26	1/28	Columnar

lattice spacing in the $\tan^{-1}(1/2)$ direction without affecting the configurations in the other diagonals [see Fig. 4.1(f)]. Thus, the conjecture predicts that there should be multiple transitions in the 10-NN and 11-NN model.

The analysis is easily extended to larger k by constructing the fully packed configurations. For instance, the next k to have columnar order at high densities is $k = 14$. The nature of the high density phase and the density at full packing for $k \leq 14$ are summarized in Table. 4.1.

4.3 Monte Carlo simulations for $k = 6, \ldots, 11$

In this section, we present results from Monte Carlo simulations for k-NN HCLG models with $k = 6, \ldots, 11$ to verify the conjecture presented in Sec. 4.2. We refer to Sec. 2.1.2 and Table 2.1 for details of the simulations. We present the details for $k = 6$ to $k = 9$ in Sec. 4.3.1, $k = 10$ is Sec. 4.3.2, $k = 11$ in Sec. 4.3.3.

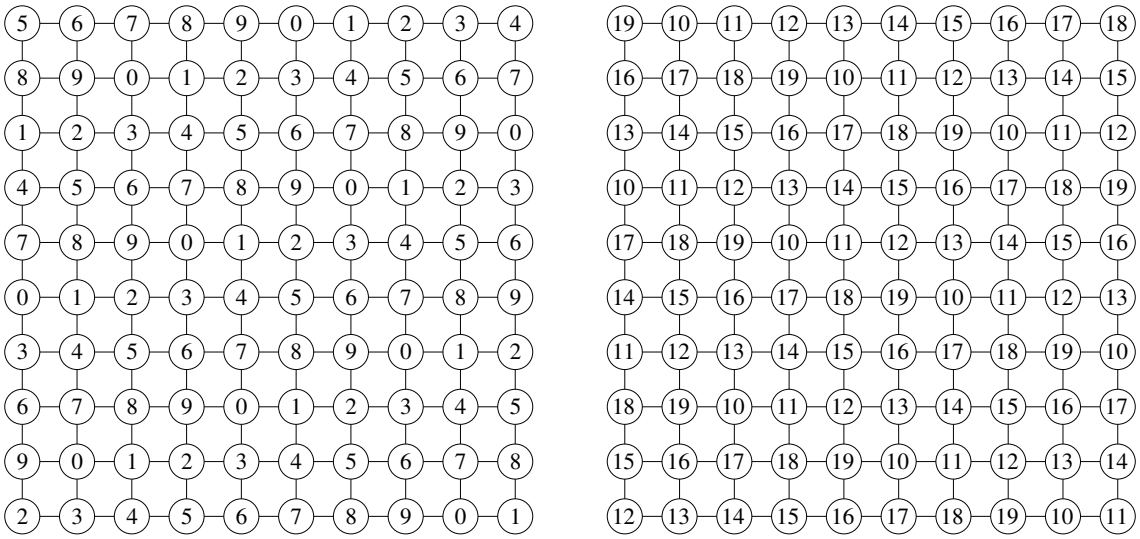

Figure 4.2: The sublattices of the 6-NN model. (a) All sites on a diagonal oriented in the $\tan^{-1}(1/3)$ direction belong to the same sublattice. (b) All sites on a diagonal oriented in the $\tan^{-1}(3)$ direction belong to the same sublattice.

4.3.1 The 6-NN to 9-NN models

The conjecture in Sec. 4.2 predicts a single first order transition from a disordered phase to an ordered sublattice phase for $k = 6, 7, 8, 9$. In order to define suitable order parameters, we divide the lattice sites into different sublattices. Like in the 4-NN model, each site belongs to two sublattices.

The sublattices for the 6-NN model are shown in Fig. 4.2. In Fig. 4.2(a) [Fig. 4.2(b)], all sites belonging to a diagonal oriented in the $\tan^{-1}(1/3)$ [$\tan^{-1}(3)$] direction belong to the same sublattice. There are 10 sublattices each for the two choices. In the high density phase, most particles will occupy one of the 20 sublattices with maximum density $1/10$.

The sublattices for the 7-NN model are shown in Fig. 4.3. In Fig. 4.3(a) [Fig. 4.3(b)], all sites belonging to a diagonal oriented in the $\tan^{-1}(2/3)$ [$\tan^{-1}(3/2)$] direction belong to the same sublattice. There are 12 sublattices each for the two choices. In the high density phase, most particles will occupy one of the 24 sublattices with maximum density $1/12$.

The sublattices for the 8-NN model are shown in Fig. 4.4. In Fig. 4.4(a) [Fig. 4.4(b)], all

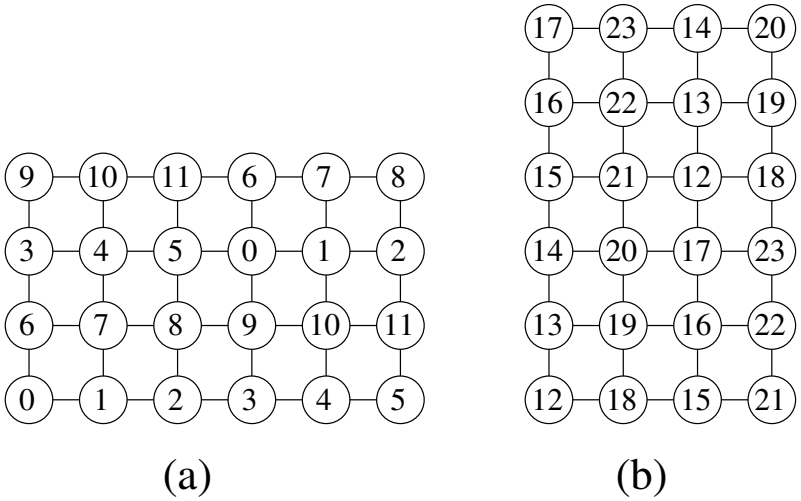

Figure 4.3: The sublattices of the 7-NN model. (a) All sites on a diagonal oriented in the $\tan^{-1}(2/3)$ direction belong to the same sublattice. (b) All sites on a diagonal oriented in the $\tan^{-1}(3/2)$ direction belong to the same sublattice.

sites belonging to a diagonal oriented in the $\tan^{-1}(1/4)$ [$\tan^{-1}(-4)$] direction belong to the same sublattice. There are 15 sublattices each for the two choices. In the high density phase, most particles will occupy one of the 30 sublattices with maximum density $1/15$.

The sublattices for the 9-NN model are identical to that for the 8-NN model shown in Fig. 4.4, and hence maximum density will be $1/15$.

To study the phase transition into the sublattice phase for $k = 6$ to 9, we define an order parameter

$$Q_k = |Q_k^{(a)}| - |Q_k^{(b)}|, \tag{4.1}$$

where $k = 6, 7, 8, 9$ denotes k-NN and $Q_k^{(a)}$ and $Q_k^{(b)}$ measure sublattice ordering according to the sublattice labeling in (a) and (b) respectively of Figs. 4.2, 4.3, and 4.4 and are defined as

$$Q_k^{(a)} = \sum_{j=0}^{m-1} \rho_j e^{2\pi\iota j/m}, \tag{4.2}$$

$$Q_k^{(b)} = \sum_{j=m}^{2m-1} \rho_j e^{2\pi\iota j/m}. \tag{4.3}$$

Here ρ_j is the particle density in sublattice j. The parameter m depends on k and has values

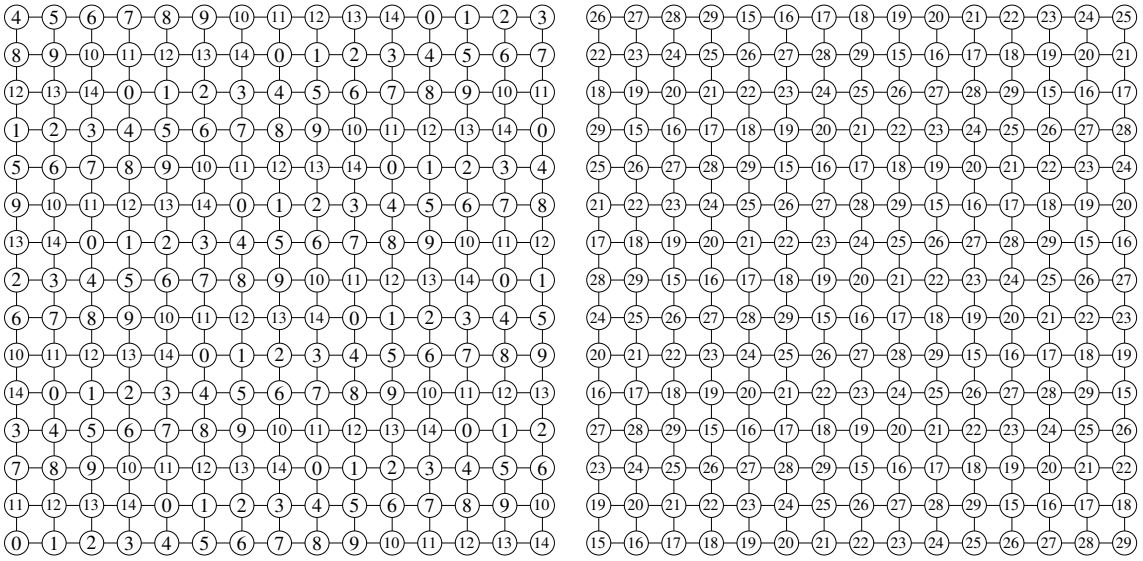

(a) (b)

Figure 4.4: The sublattices of the 8-NN and the 9-NN models. (a) All sites on a diagonal oriented in the $\tan^{-1}(1/4)$ direction belong to the same sublattice. (b) All sites on a diagonal oriented in the $\tan^{-1}(-4)$ direction belong to the same sublattice.

10 (6-NN), 12 (7-NN), 15 (8-NN) and 15 (9-NN). Clearly, Q_i is zero in the disordered phase and non-zero in the sublattice ordered phase.

We now study the transitions for $k = 6$ to $k = 9$ using the above order parameter. To show that a transition is first order, we measure the probability density function (pdf) of the density ρ and order parameter Q_k near the transition for two different values of L. The pdfs should have two peaks that do not move closer to each other with increasing L. One of the peaks correspond to the disordered phase and the other to the ordered phase. This will be taken as a signature of a first order transition.

We observe transitions at critical chemical potentials $\mu_c \approx 4.66$ ($k = 6$), $\mu_c \approx 4.88$ ($k = 7$), $\mu \approx 6.07$ ($k = 8$), and $\mu \approx 4.63$ ($k = 9$). Surprisingly, we find μ_c for 9-NN to be smaller than that for 6-NN.

The pdfs for ρ and Q_k are shown in Fig. 4.5 (a), (b) [6-NN], (c), (d) [7-NN], Fig. 4.6 (a), (b) [8-NN] and (c), (d) [9-NN]. In all the plots, we observe that the pdfs have two peaks that do not approach each with increasing system size. For 8-NN [see Fig. 4.6 (a), (b)], there is a long-lived metastable state at a density that lies between those for the

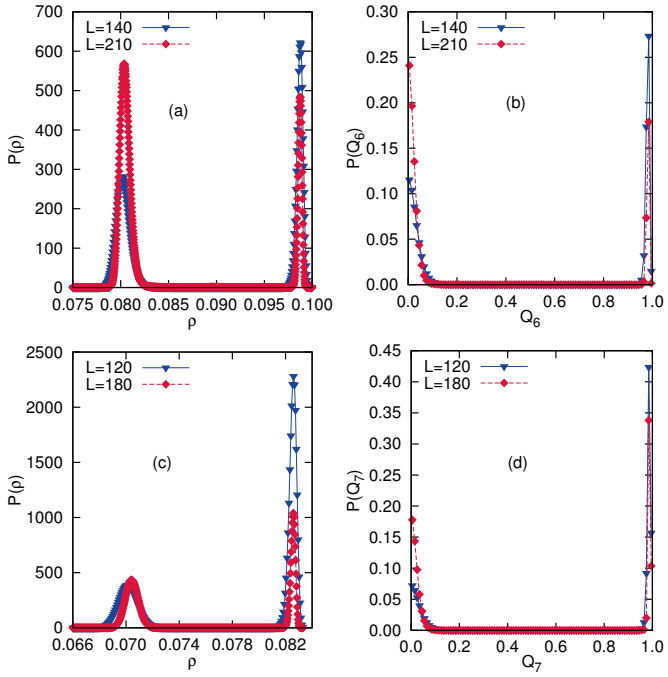

Figure 4.5: The probability density function for density ρ (left panels) and order parameter Q_k (right panels) for $\mu \approx \mu_c$, the critical chemical potential, for two different system sizes. The data are for the k-NN model with $k = 6$ [(a) and (b)] and $k = 7$ [(c) and (d)].

low-disordered phase and the high-density sublattice phase. Hence, the pdf for $\mu > \mu_c$ is peaked at a value different from the peak at the transition point. We, therefore, conclude that the transitions in the 6-NN to 9-NN models are first order. We check that the phase for values of $\mu \lesssim \mu_c$ is the disordered phase and for values of $\mu \gtrsim \mu_c$ is the sublattice ordered phase (by looking at typical snapshots) expected at full packing. Thus, we do not expect any more transitions. Both the first order nature and the single transition are consistent with the conjecture in Sec. 4.2.

4.3.2 The 10-NN model

For the 10-NN model, the conjecture in Sec. 4.2 predicts multiple transitions. In this subsection, we confirm the same. We divide the lattice into sublattices as shown in Fig. 4.7. Each site belongs to two sublattices. In Fig. 4.7(a) [Fig. 4.7(b)], all sites belonging to a diagonal oriented in the $\pi/4$ ($3\pi/4$) direction belong to the same sublattice. There are 6

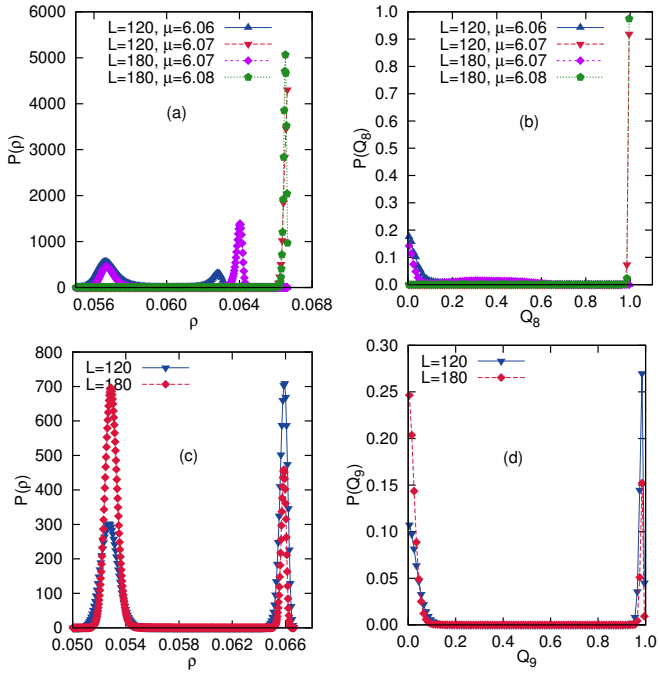

Figure 4.6: The probability density function for density ρ (left panels) and order parameter Q_k (right panels) for $\mu \approx \mu_c$, the critical chemical potential, for two different system sizes. The data are for the k-NN model with $k = 8$ [(a) and (b)] and $k = 9$ [(c) and (d)].

sublattices each for the two choices.

In the high density phase, we expect the system to be in a columnar phase where all the particles occupy one sublattice either from 0 to 5 or from 6 to 11. For example, if the particles are all in sublattice 0 direction, they are also in sublattices 6, 8 and 10. The maximum density possible is $1/18$.

Typical snapshots of the 10-NN model are presented in Fig. 4.8 at low, intermediate and high densities. In the left panel particles are colored according to whether they belong to sublattices 0,1,...5, and in the right panel according to whether they belong to sublattices 6,7,....11. At low densities [see Fig. 4.8(a)], all six colors are present roughly equally in both the left and right panels. This is the disordered phase. At intermediate densities [see Fig. 4.8(b)], majority of particles have three of the six colors in both left and right panels. This corresponds to particles preferably occupying either the even sublattices or the odd sublattices. At high densities [see Fig. 4.8(c)], we find that the particles occupy one of the six sublattices from 0–5 or 6–11, but not from both. In left panel of Fig. 4.8(c) particles

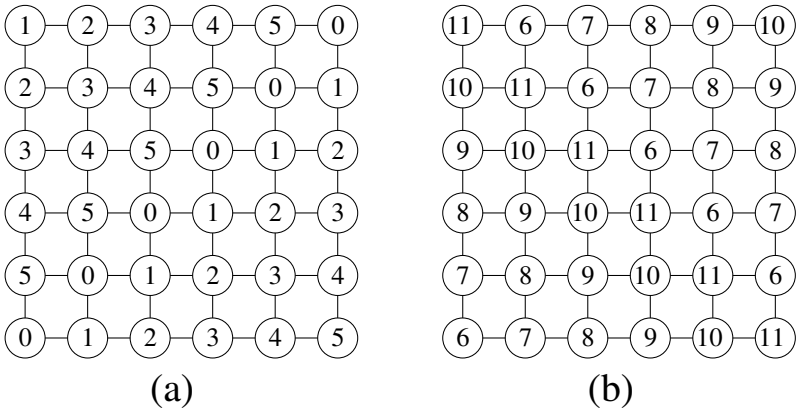

Figure 4.7: The sublattices of the 10-NN model. (a) All sites on a diagonal oriented in the $\pi/4$ direction belong to the same sublattice. (b) All sites on a diagonal oriented in the $3\pi/4$ direction belong to the same sublattice.

preferentially occupy sublattice 0. However, in the right panel, particles occupy mostly three even sublattices (6, 8 and 10). There are 12 such states, corresponding to the number of sublattices.

We first show that, if all the particles are in sublattice 0 in the columnar phase, then there is a sliding instability along sublattices 2 and 4. To do so, we consider configurations with defects on sublattice 2 or sublattice 4 that are rod-like, and show that rods of all lengths contribute at same order. In Fig. 4.9, we show examples of configurations with rods of length 3 on sublattice 2 (black circles) and on sublattice 4 (lightly shaded circles). A rod of length n excludes 5 sites each from $n+1$ diagonals belonging to sublattice 0. The contribution from configurations with rods of length n to the ratio of partition functions $\mathcal{L}(z_0,0,z_2,0,0,0/\mathcal{L}(z_0,0,0,0,0,0)$ configuration is

$$\frac{N}{6}z_2^n\left[\frac{\Omega_o(z_0,L-5)}{\Omega_p(z_0,L)}\right]^{n+1}. \tag{4.4}$$

In the 10-NN model, along a diagonal, a particle excludes its nearest and next-nearest neighbors from being occupied by a particle. Then, to leading order $\Omega_o(z_0,L-5)\sim z_0^{L/3-1}$, and $\Omega_p(z_0,L)\sim z_0^{L/3}$. Thus, the term in Eq. (4.4) is z^{-1} to leading order for all $n\geq 1$.

Thus, the sliding instability exists along sublattices 2 and 4. It is straightforward to verify

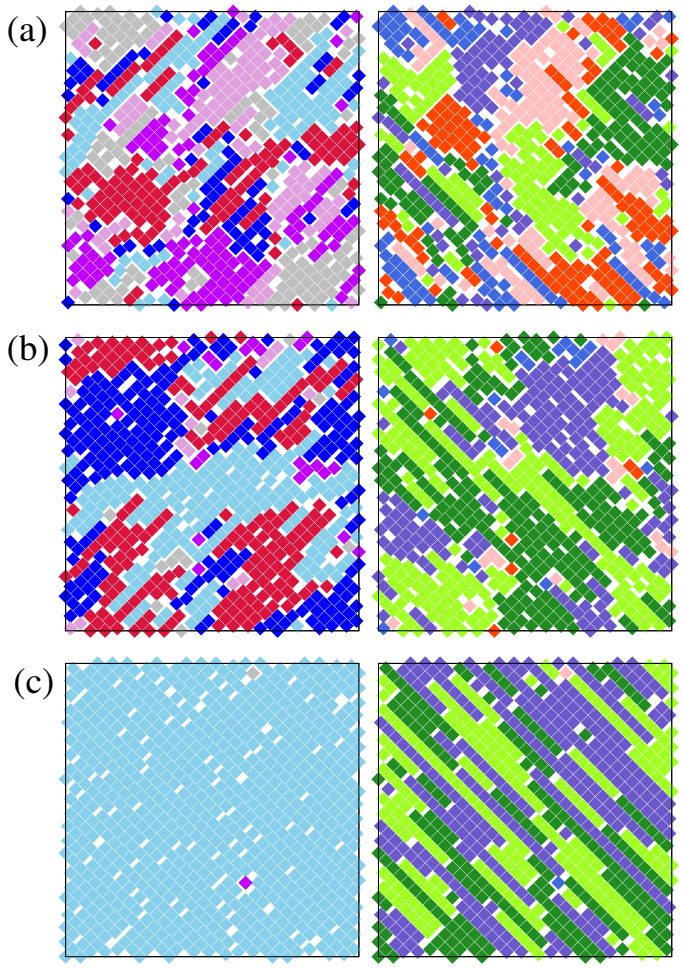

Figure 4.8: Snapshots of typical configurations of the 10-NN model. The particles are colored according to the sublattice it belongs to (see Fig. 4.7). In the left panel, the colors are light blue for 0, dark magenta for 1, blue for 2, plum for 3, dark-red for 4 and gray for 5. In the right panel, the colors are dark green for 6, orange-red for 7, light green for 8, pink for 9, slate blue for 10 and royal blue for 11. (a) Low density disordered phase where all six colors are present in both panels. (b) Intermediate density sublattice phase, where even or odd sublattices are preferentially occupied. (c) High density columnar phase, where one sublattice in one of the panels (left in figure) and three sublattices in the other panel are preferentially occupied.

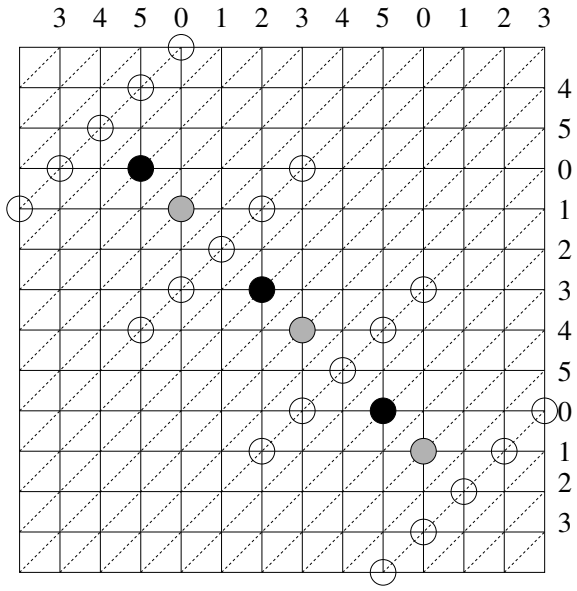

Figure 4.9: An example of rod-like defects of length 3 on sublattices 2 (black circles) or 4 (grey circles) in the 10-NN model. Exclusions only on sublattice 0 are shown by empty circles. $0, 1, 2, 3, 4, 5$ on the edge of the box denote diagonals that belong to sublattices $0, 1, 2, 3, 4, 5$ respectively.

that it does not exist on sublattices 1, 3, and 5. The conjecture in Sec. 4.2 then predicts that as z is decreased, the columnar phase should first destabilize into a phase where particle densities will be equal on all even sublattices and all odd sublattices, but not equal to each other. If we label the even sublattices as A and odd sublattices as B, then there is a symmetry breaking between A and B. Further decrease in z would result in a disordered phase. Like for the 4-NN model, we will call the intermediate phase as a sublattice phase.

In terms of increasing z or μ, we expect the first transition to be in the universality class of two dimensional Ising model because of symmetry breaking between two symmetric phases. In the second transition, the system chooses from one of 6 symmetric phases. By analogy with Potts model, we expect the second transition to be first order.

We now confirm these predictions numerically. To study the first transition, we define an order parameter,

$$Q_1 = |(\rho_0 + \rho_2 + \rho_4) - (\rho_1 + \rho_3 + \rho_5)|, \tag{4.5}$$

where ρ_i are the particle densities on sublattice i. Q_1 measures the density difference be-

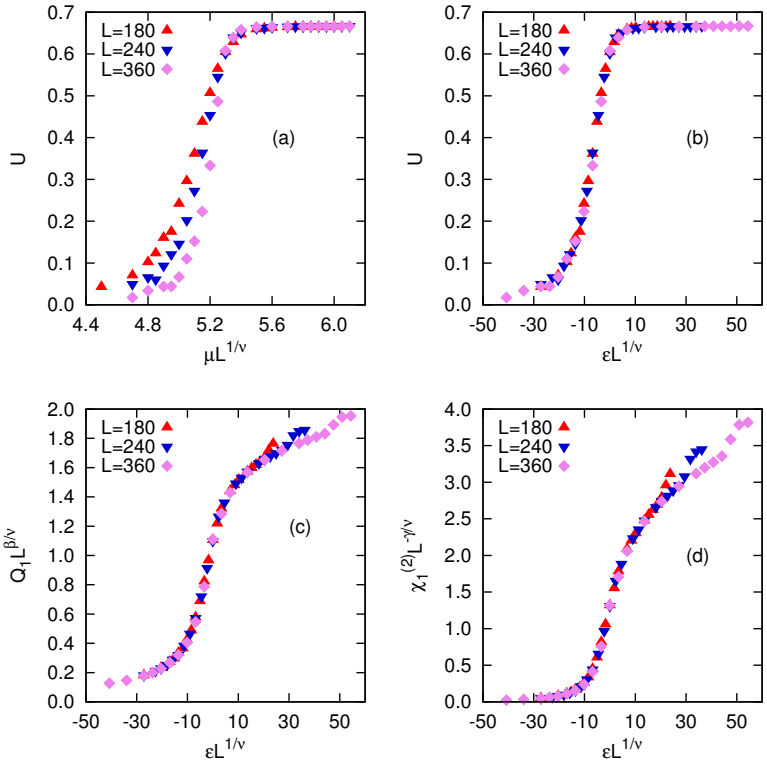

Figure 4.10: The data for cumulants of Q_1 for the 10-NN model near the first transition from the disordered phase to sublattice phase. (a) The Binder cumulant U_1 for different L crosses at $\mu_c = 5.30$. The data for (b) U_1, (c) Q_1, and (d) $\chi_1^{(2)}$ for different L collapse onto a single curve when scaled as in Eq. (3.3) with the Ising exponents $\beta/\nu = 1/8$, $\gamma/\nu = 7/4$, and $\nu = 1$.

tween even and odd sublattices. The data for the different thermodynamic quantities near the disordered-sublattice transition are shown in Fig. 4.10. The critical chemical potential μ_c is obtained from the intersection of the Binder cumulant curves U_1 for different system sizes. We obtain $\mu_c = 5.3 \pm 0.05$. The data for U_1 [see Fig. 4.10(b)], Q_1 [see Fig. 4.10(c)] and $\chi_1^{(2)}$ [see Fig. 4.10(d)] for different system sizes collapse onto a single curve when scaled as in Eq. (3.3) with Ising exponents $\beta/\nu = 1/8$, $\gamma/\nu = 7/4$ and $\nu = 1$. These results confirm that the first transition is continuous and is consistent to the Ising universality class.

We now study the second transition. This is best done using an order parameter Q_{10} as defined in Eqs. (4.1) and (4.2) with $m = 6$ in Eq. (4.2). Q_{10} is zero in disordered and sublattice phases and non-zero in the columnar phase. We find that Q_{10} is zero for

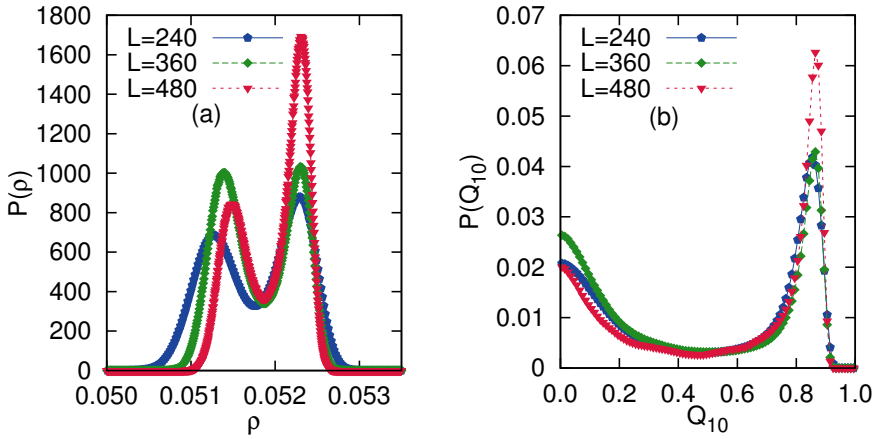

Figure 4.11: The probability density function for (a) density ρ and (b) order parameter Q_{10} near the transition point ($\mu_c \approx 6.0$) for three different system sizes. The data are for the 10-NN model.

$\mu \lesssim 5.95$ and non zero for $\mu \gtrsim 6.00$. These values are distinctly larger than the critical chemical potential found above for the first transition (5.30). To establish the first order nature of the transition, we measure the pdfs of density ρ and Q_{10} near the transition point. These are shown in Fig. 4.11 (a) and (b). The pdfs for both quantities have two well separated peaks that become sharper with increasing system size. This is a clear signature of a first order transition.

We check that the phase for values of $\mu \gtrsim \mu_c$ is the columnar ordered phase (by looking at typical snapshots) expected at full packing. Thus, we do not expect any more transitions. Thus, the numerical data are consistent with the conjecture in Sec. 4.2.

4.3.3 The 11-NN model

For the 11-NN model, the conjecture in Sec. 4.2 predicts multiple transitions. In this subsection, we numerically confirm the same. We divide the lattice into sublattices as shown in Fig. 4.12. In contrast to sublattice decomposition for $k \leq 10$, now each site belongs to four sublattices. In Fig. 4.7(a), (b), (c), and (d), all sites belonging to a diagonal oriented in the $\tan^{-1}(1/2)$, $\tan^{-1}(-1/2)$, $\tan^{-1}(2)$, and $\tan^{-1}(-2)$ directions respectively belong to the same sublattice. There are 10 sublattices for each of the four choices.

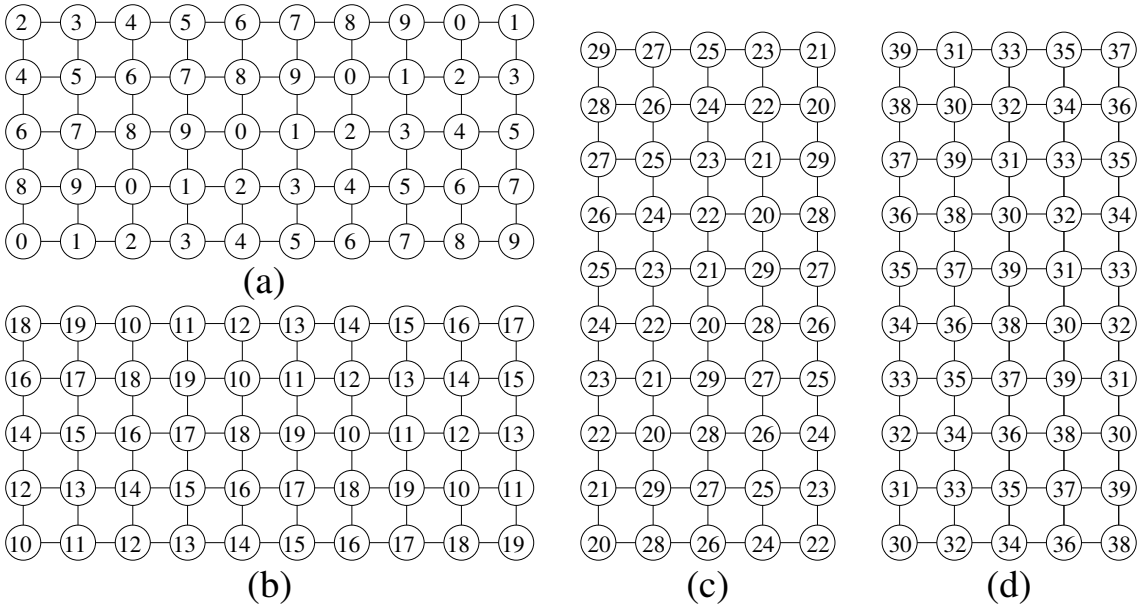

Figure 4.12: The sublattices of the 11-NN model. (a) All sites on a diagonal oriented in the $\tan^{-1}(1/2)$ direction belong to the same sublattice. (b) All sites on a diagonal oriented in the $\tan^{-1}(-1/2)$ direction belong to the same sublattice. (c) All sites on a diagonal oriented in the $\tan^{-1}(2)$ direction belong to the same sublattice. (b) All sites on a diagonal oriented in the $\tan^{-1}(-2)$ direction belong to the same sublattice.

In the high density phase, we expect the system to be in a columnar phase where all the particles occupy one sublattice chosen from one of the sets 0 to 9, 10 to 19, 20 to 29, and 30 to 39. An example of a columnar phase would be all particles in sublattice 0. In that case, the particles are also simultaneously in all even sublattices between 10 and 19, all sublattices between 20 and 29, and sublattices 30 and 35. Along a diagonal in sublattice 0, there is nearest neighbor exclusion. Hence, the maximum density possible is $1/20$.

Consider, now, the high density phase. Suppose the ordered phase is one in which all particles are present in sublattice 0. We now introduce defects and ask what sublattices have a sliding instability. We skip the details, but it is straightforward to verify that the sliding instability is present only for sublattice 5. This means that n-rod defects of n defects on sublattice 5 contribute to the same order in the free energy. The conjecture in Sec. 4.2 therefore predicts that the high density phase should destabilize into a phase where two sublattices are equally occupied. Further decrease in chemical potential would finally result in a low density disordered phase.

We now present results from Monte Carlo simulations for the 11-NN model. As chemical potential is increased, we find that the system undergoes a first order transition (see below) at $\mu_c \approx 6.40$. However, for $\mu \gtrsim \mu_c$, the phase that we observe is not the phase where 2 sublattices are present. Instead, we observe a phase in which particles are mostly present on even sublattices (for e.g., 0,2,4,6,8) or odd sublattices (for e.g.,1,3,5,7,9). Equivalently, in terms of rows and columns, the particles occupy every fourth row or every fourth column. There are 8 such states.

A convenient order parameter to study the transition is

$$Q_{11} = |\sum_{j=0}^{3} r_j e^{2\pi\iota j/4}| - |\sum_{j=0}^{3} c_j e^{2\pi\iota j/4}| \tag{4.6}$$

where r_j is the particle density in rows $[j \mod 4]$ and c_j is the particle density in columns $[j \mod 4]$. Q_{11} is zero in the disordered phase and non-zero in the intermediate phase.

We first show that the density ρ has a discontinuity across the transition. In Fig. 4.13, we show the pdf for ρ for three different system sizes near the transition point. The pdfs have two distinctly separated peaks that sharpen with system size. This is a clear indication of a first order transition.

The densities above the transition are very close to the maximum density possible (1/20). Since there is a possibility that the system may not have equilibrated, we present evidence for equilibration. The variation of density ρ and the order parameter Q_{11} with time is shown in Fig. 4.14. The data are for two different initial conditions. In the first, the initial configuration is one of maximal density, where all particles are on sublattice 0. In the second, the initial configuration is a random one where 10^5 deposition attempts (singe particle) are made at random locations. We find that, though the time profiles for the two initial conditions are different, they are statistically identical for larger times (see Fig. 4.14(a) for ρ and (b) for Q_{11}. Further, we also check using snapshots that the long time behaviour for both initial conditions is one every fourth row or column are occupied.

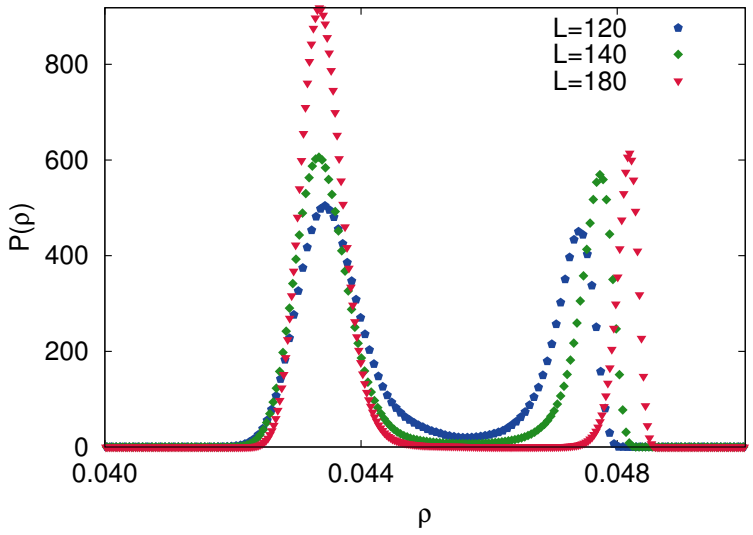

Figure 4.13: The probability distribution function for density ρ near the transition point for three different system sizes. The data are for the 11-NN model.

We, thus, conclude that the system is equilibrated in our simulations.

The intermediate phase, being different from the fully packed phase, we expect at least one more transition. But our conjecture in Sec. 4.2 predicts the existence of a phase where two sublattices are occupied. If this conjecture is true, then we expect at least two more transitions with increasing μ. Unfortunately, within available computational time, we are unable to equilibrate the system for larger μ, and hence unable to verify the above claim.

4.4 Discussion

In this chapter, we studied the two-dimensional k-NN hard core lattice gas model with $6 \leq k \leq 11$. In Chapter 3 we showed that in the 4-NN model 8-fold symmetry is broken in two steps leading to two continuous transitions rather than a single first order transition. From high-density expansion of density and free-energy we conjecture that if the high density phase is columnar and the system is not a hard square system, then the model should show multiple transitions. This conjecture predicts single first order transitions for $k = 6, 7, 8, 9$, and multiple transitions for $k = 10, 11$. This claim was verified numerically

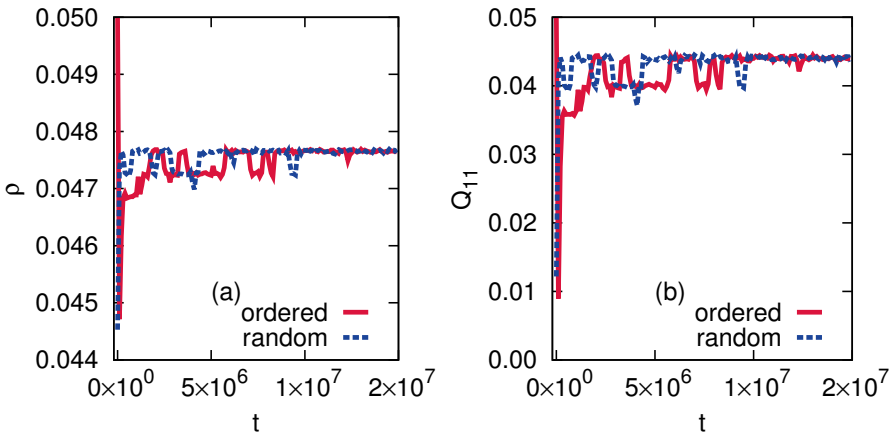

Figure 4.14: The variation of (a) density ρ and (b) order parameter Q_{11} with time t for the 11-NN model when $\mu \gtrsim \mu_c$. The data are for two different initial conditions. In the first, labelled "ordered", all particles are in sublattice 0. In the second, labelled "random", particles are initially deposited at random.

in this chapter.

In particular, for the 10-NN model, we showed that there are two transitions. The first transition into a sublattice phase is continuous and is indistinguishable from the Ising universality class. The second transition is first order. For the 11-NN model, due to computational limitations, we were able to numerically study only the first transition. However, the intermediate ordered phase was shown to be different from the phase at full packing. Hence, at least one more transition will definitely be present. Surprisingly, we found the intermediate phase to be different from what we found for the 4-NN and 10-NN models. For these latter models, as z is decreased from infinity, the system first destabilizes into a state where the original sublattice and sublattices with sliding instability are present, consistent with our conjecture. Hence, we expect the 11-NN model to undergo at least three transitions with increasing density.

It would be interesting to verify the above claim for 11-NN. Unfortunately, we are unable to equilibrate the 11-NN system at densities higher than just beyond the first transition. Seeking improvements to the algorithm in the future may help. One possible direction would be to use flat histogram Monte Carlo algorithms like the the Wang-Landau algorithm [187, 188] or tomographic sampling [189, 190]. A different approach would be to

calculate the high density expansion for the densities of particles in different sublattices for the 10-NN and 11-NN models. Like in the 4-NN model, this will help to identify the preferred sublattices for generation of defects.

Explaining the transitions in the k-NN models by analytical methods is an open problem. Possible approaches include modified Flory approximation [26] and fundamental measure theory [23, 133, 173] that have been applied earlier to HCLG models like the 2-NN model. Reproducing the two transitions in the 4-NN model would be a test for efficacy of these theories. A different approach would be to look for exact solutions for arbitrary k on simpler lattices like the random lattice or the Bethe lattice where the solution of the 1-NN model is known [191], or the recently introduced random locally tree like layered lattice [170, 171].

Chapter 5

The high density phase of the k-NN model

5.1 Introduction

In Chapter 3 we showed numerically that the 4-NN model surprisingly undergoes two phase transitions as density is increased: first from a low density disordered phase to an intermediate sublattice phase and second from the sublattice phase to a high density columnar phase. The existence of two transitions was rationalized by deriving a high density expansion about the ordered columnar phase. Columnar phases have a sliding instability in which a defect created by removing a single particle from the fully packed configuration splits into fractional defects that slide independently of each other along some direction [11, 19, 174]. The high density expansion for the 4-NN model showed that the sliding instability is present in only certain preferred sublattices. As density is decreased from full packing, it is thus plausible that the columnar phase destabilizes into these preferred sublattices resulting in a sublattice phase rather than a disordered phase. This led us to conjecture that for a given k, if the model satisfies the two conditions (i) the high-density phase is columnar and (ii) the sliding instability is present in only a

Table 5.1: The nature of the ordered phases and the transitions for $k \leq 11$. More than one entry for a given value of k indicates that multiple transitions occur with increasing density with the phases appearing in the order it is listed. Question marks denote that the result is not known.

k	Ordered phases	Nature of transition
1	Sublattice	Continuous (Ising)
2	Columnar	Continuous (Ashkin-Teller)
3	Sublattice	Discontinuous
4	Sublattice	Continuous (Ising)
	Columnar	Continuous (Ashkin-Teller)
5	Columnar	Discontinuous
6	Sublattice	Discontinuous
7	Sublattice	Discontinuous
8	Sublattice	Discontinuous
9	Sublattice	Discontinuous
10	Sublattice	Continuous (Ising)
	Columnar	Discontinuous
11	?	?
	Columnar	?

fraction of the sublattices, then the system will show multiple transitions. In Chapter 4 implementing a Monte Carlo algorithm with cluster moves [20, 90, 162], we were able to numerically verify the conjecture for $k = 6, 7, 8, 9$, by showing the presence of a single first order transition, and for $k = 10, 11$ (for which the high density phase is columnar), by showing the presence of multiple phase transitions [179]. The results for $k \leq 11$ are summarized in Table. 5.1.

The presence of multiple transitions in the k-NN model, which was hitherto unexpected, raises the intriguing possibility that in the continuum limit $k \to \infty$, the system may show multiple transitions as in the hard sphere problem in two dimensions. Monte Carlo simulations of systems with $k \geq 12$ is impractical as, at high densities, the large excluded volume per particle results in the the system getting stuck in long lived meta stable states, making it a poor candidate for studying large k. Instead, in this chapter, we find those values of k for which the high density ordered phase is columnar by determining the configuration at full packing.

The rest of the chapter is organized as follows. In Sec. 5.2, we precisely define the model

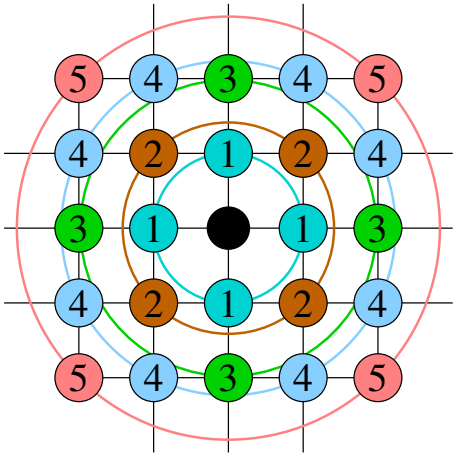

Figure 5.1: Consider a particle placed on the central black lattice site. The labels $n = 1$ to $n = 5$ denote the sites that are the n^{th} next nearest neighbors of the particle. In the k-NN hard core lattice gas model all the sites with labels less than or equal to k are excluded from being occupied by another particle. The excluded regions are also shown by concentric circles such that all sites within the circle of radius R are excluded for a given k.

and the columnar and sublattice phases. In Sec. 5.3, we explain the procedure for determining whether the high density phase has columnar order. Implementing this algorithm, we show that the number of system with columnar order is finite and that for large k, the high density phase has sublattice order. We conclude with discussions in Sec. 5.4. The content of this chapter is in Ref. [192].

5.2 Model and definitions

Consider a square lattice with periodic boundary conditions. A site may be empty or occupied by utmost one particle. A particle in a k-NN model excludes the first k next nearest neighbors from being occupied by another particle. Figure 5.1 shows the excluded sites for $k = 1, \ldots 5$, where the label n refers to the n-th next nearest neighbor. We refer to this model as the k-NN model. As an example, only the nearest neighbors are excluded in the 1-NN model. With increasing k, the successive excluded regions correspond to lattice sites within circles of radius R, where R^2 are norms of the Gaussian integers.

Our conjecture states that for multiple phase transitions to be seen, the high-density phase

should be columnar in nature and the sliding instability should be present in only a fraction of the sublattices. If the excluded volume is a perfect square oriented along the x or y-axes, then the high density phase will be columnar, but the sliding instability will be present in all sublattices. However, the excluded volume is a hard square oriented along the axes only when $k = 2$ and $k = 5$. Thus, the conjecture reduces to determining for a given $k > 5$ whether the high density phase has columnar order. This may be determined by examining the fully-packed phase.

We now give an example of a columnar phase at full packing to identify a criterion to determine whether the fully packed phase has columnar order. Consider the 4-NN model whose high density phase has columnar order [179]. A typical configuration at full packing is shown in Fig. 5.2. We divide the lattice into four sublattices depending on the diagonal that it belongs to. However, diagonals may be oriented in the $\pi/4$ [see Fig. 5.2(a)] or in the $3\pi/4$ [see Fig. 5.2(b)] directions and, thus, two such labellings are possible. In the configuration shown, all particles are in sublattice 2 when sites are labeled from 0 to 3 [see Fig. 5.2(a)], but in sublattices 4 and 6 when sites are labeled from 4 to 7 [see Fig. 5.2(b)]. Clearly, there are 8 such phases possible. The key feature is that when boundary conditions are periodic, then the particles may slide freely along diagonals (red lines in Fig. 5.2), independent of other diagonals. Thus, the degeneracy of the fully packed phase increases exponentially with system size.

In contrast, when the system has sublattice order, the number of fully packed configurations are finite. An example is the 1-NN model. In this case, the lattice may be divided into two sublattices such that neighbors of a site of one sublattice belong to the other sublattice (see Fig. 5.3). In the limit of full packing, all the particles are either in sublattice A or in sublattice B, and only two configurations are possible irrespective of system size.

Thus, we fix the the criterion for columnar order at full packing to be that the particles should be slidable along some direction (not necessarily $\pi/4$ or $3\pi/4$ as in 4-NN) independent of the positions of the other particles resulting in a highly degenerate fully packed

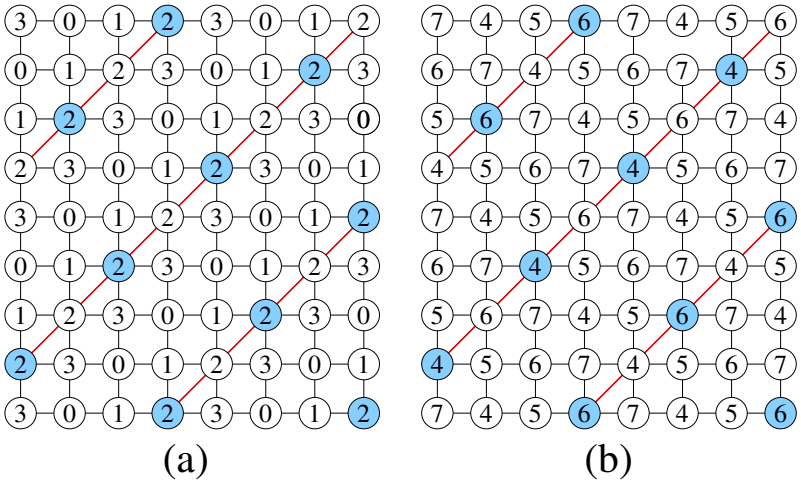

Figure 5.2: The sublattices for the 4-NN model. The lattice sites are labeled according to diagonals oriented in the (a) $\pi/4$ direction or (b) $3\pi/4$ direction. The filled blue sites correspond to a typical configuration at maximal density. In the example shown the particles are in sublattice 2 [see (a)] or equivalently sublattices 4 and 6 [see (b)].

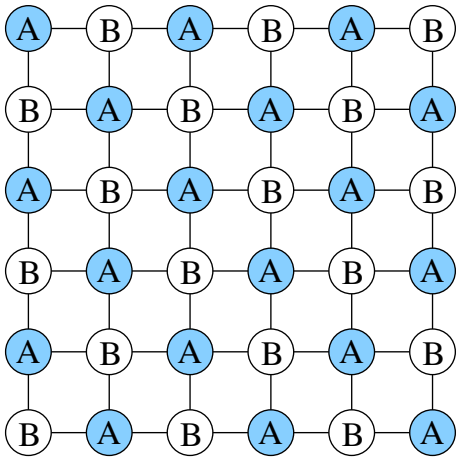

Figure 5.3: The two sublattices for the 1-NN model are shown by A and B. A fully packed configuration (shown by blue filled sites) consists of all particles being in sublattice A (as shown in figure) or in sublattice B.

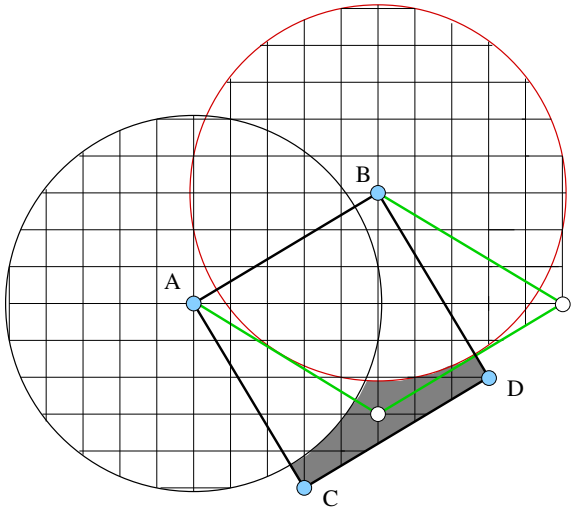

Figure 5.4: A schematic diagram to explain the procedure for constructing the unit cell at full packing. The unit cell is a parallelogram ABCD. The blue (filled) circles are particles. All lattice points inside the black and red circles are excluded by A and B respectively. If C is placed on the lattice site denoted by white (open) circle, then the parallelogram has smaller area than the square $ABCD$.

state. In Sec. 5.3, we describe the algorithm for checking slidability in the fully packed configuration.

5.3 Results

To find the possible configurations for the k-NN model at full packing, we proceed as follows. The unit cell that repeats to give the fully packed configuration is a parallelogram. Let the particle at the top left corner of the parallelogram be denoted by A (see Fig. 5.4). We choose the origin of the coordinate system to be at A. The excluded volume of A is a circle (shown in black in Fig. 5.4) whose radius is dependent on k. Let the particle at the top right corner of the parallelogram be denoted by B with coordinates (x, y). We restrict the choice of B to be in the first octant ($x \geq y$), as a choice in the second octant may be mapped onto the first octant by rotation. For every $y \geq 0$, x is the minimum value such that $x^2 + y^2 > R^2$, where R is the radius of the excluded volume. The excluded volume of B is shown by a red circle in Fig. 5.4.

For a fixed A and B, the orientation and length of the segment CD is fixed as the unit cell is a parallelogram. The position of C is determined by the constraint that the area of the parallelogram is the minimum and is determined as follows. A convenient initial choice of C that does not violate the hard-core constraint is obtained by rotating the point B counterclockwise about A by $\pi/2$ such that the unit cell is a square (see Fig. 5.4). A choice of C where $\angle BAC > \pi/2$ may be mapped onto a unit cell where $\angle BAC < \pi/2$ by translating the segment CD by its length along its length. It is now straightforward to see that any choice of C that results in a smaller area for the unit cell as compared to the initial square must lie within the initial square and outside the excluded volume of A and B (for example, the lattice point shown by an empty circle in Fig. 5.4). We fix C by minimizing the area of the parallelogram over all such points.

The minimization of area is repeated over all possible choices of B to determine the unit cell and the maximal packing density. If the segment CD now passes through any lattice point that is outside the excluded volume of A and B, then C could be moved to that lattice point to give a parallelogram of same area. Likewise, if AC passes through any lattice point that is outside the excluded volume of B and D, then A could be moved to that lattice point to give a parallelogram of same area. If such multiple choices are possible, then we identify the high-density phase to have columnar order.

Using the above procedure, we identify the fully packed configuration for k up to 820302 corresponding to $R^2 = 3999997$, where R is the radius of the smallest circle around a site that encloses all its excluded lattice sites. The number of distinct values of k increases linearly with R^2 [see Fig. 5.5(a)]. Asymptotically we find $k \approx 0.148R^2$, for $R \gg 1$. The values of k for which the high density phase has columnar order are listed in Table 5.2. We find that up to the values of R^2 that we have checked, the largest k for which there is columnar order at full packing is $k = 4183$ or $R^2 = 15482$. Among these, the stability of columnar phase for density close to full packing has been numerically established only for $k = 2, 4, 5, 10, 11$ [9, 19, 179]. Let $n_c(R)$ denote the number of systems whose exclusion

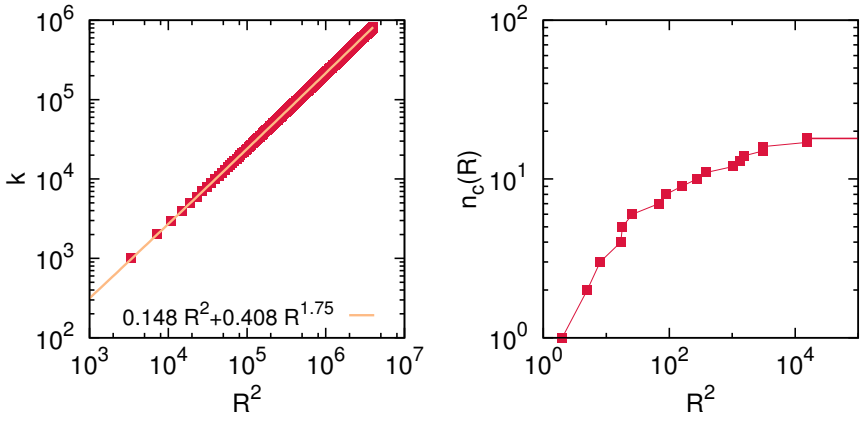

Figure 5.5: The variation with R^2 of (a) k and (b) $n_c(R)$.

is less than or equal to R and has columnar order at full packing. n_c increases irregularly with R and saturates at $n_c = 18$ [see Fig. 5.5(b)].

For large k, the fully packed configuration has sublattice or crystalline order. For each of this k we construct the Wigner-Seitz primitive cell obtained by constructing the convex envelope of the perpendicular bisectors of the lines joining a fixed particle to all other particles in the fully packed configuration. If the unit cell $ABCD$ is such that $\angle BAC$ equals $\pi/2$, then the Wigner-Seitz cell and the unit cell $ABCD$, are both squares. We find that the Wigner-Seitz cell is a square only for $k \leq 6$ and for $k = 11$. The Wigner-Seitz cell for 6-NN is shown in Fig. 5.6(a).

For other values of k, we observe that $\angle BAC$ of the unit cell is always smaller than $\pi/2$. Also the length of the two sides, AB and AC, are unequal. For these k, the Wigner-Seitz cell is an irregular hexagon where the opposite sides are parallel and of same length. Thus, pairs of opposite angles of the hexagon are equal to each other. As an example, the Wigner-Seitz cell for 13-NN is shown in Fig. 5.6(b).

We now characterize the shape of the Wigner-Seitz cell. Let the angles of the hexagon be denoted by α_1, α_2 and α_3, such that $\alpha_1 \leq \alpha_2 \leq \alpha_3$. As $R \to \infty$, the three angles approach $2\pi/3$ linearly with decreasing $1/R$ (see Fig. 5.7(a)).

Likewise, let l_1, l_2, and l_3 denote the lengths of the hexagon such that $l_1 \leq l_2 \leq l_3$. The

Table 5.2: The values of k for which the high density phase of the k-NN model has columnar order. R is radius of the smallest circle that encloses the excluded lattice sites [see Fig. 5.1]

k	R^2
2	2
4	5
5	8
10	17
11	18
14	26
31	68
39	89
64	157
105	277
141	389
342	1040
427	1322
493	1557
906	3029
907	3033
4132	15481
4133	15482

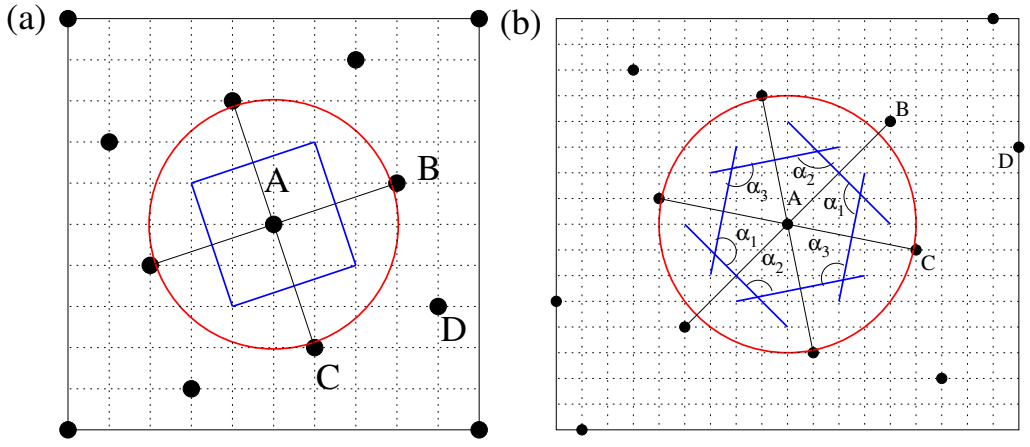

Figure 5.6: Wigner-Seitz cells for 6-NN and 13-NN models. Black dots are particles. The surrounding red circles are the exclusion regions of the central particle A. Blue lines are the perpendicular bisectors on the lines joining neighboring particles to A. Wigner-Seitz cell is a (a) square for 6-NN, (b) hexagon for 13-NN.

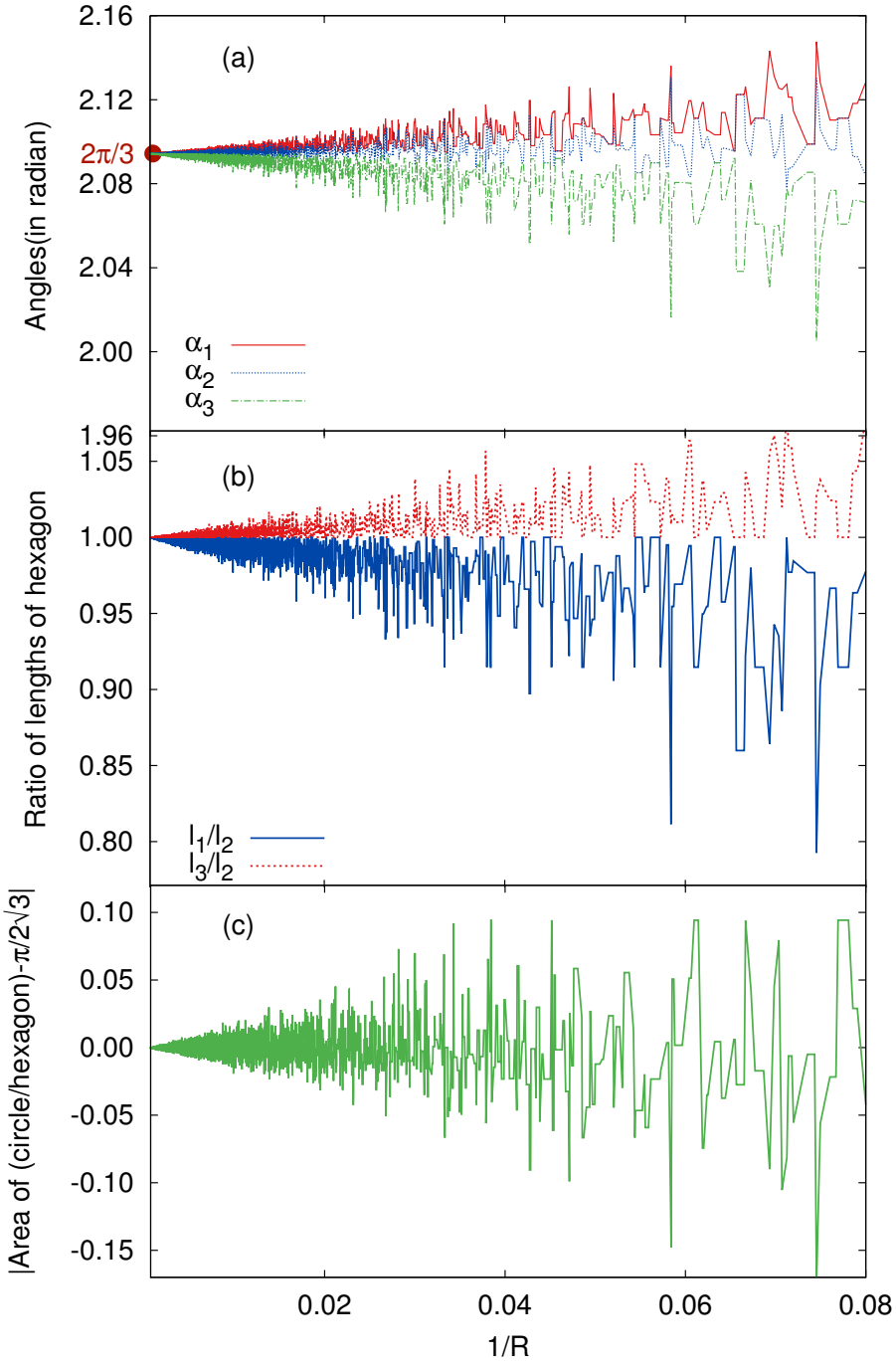

Figure 5.7: The dependence on exclusion radius R of (a) angles α_i, (b) ratios of lengths of different sides, and (c) ratio of area of the circumscribed circle to area of the hexagonal Wigner-Seitz cell.

ratios l_1/l_2 and l_3/l_2 approach 1 linearly with decreasing $1/R$ (see Fig. 5.7(b)). We thus conclude that the Wigner-Seitz cell converges to a regular hexagon with increasing k.

We also check that in the limit of large R, the packing approaches that of discs in two dimensions. For discs, the largest packing density is achieved when the packing is hexagonal close packing with packing density $\eta_h = \pi/(2\sqrt{3})$. In the limit of large R, the ratio of the area of the largest circle circumscribed in the hexagonal Wigner-Seitz cell to the area of the hexagonal cell approaches η_h (see Fig. 5.7(c)).

5.4 Discussion

In this chapter we obtained the nature of the phase at maximal density for the k-NN model hard core lattice gas models in which the first k next nearest neighbor sites of a particle are excluded from being occupied by other particles by finding out numerically the configuration that maximizes the density at full packing. We find that for up to $k = 820302$, there are only 18 values of k for which the high density phase has columnar order. The remaining ones have solid-like sublattice order. For these systems, we showed that the Wigner-Seitz primitive cell approaches a regular hexagon for large k, and the packing tends to a hexagonal packing.

The largest value of k for which we found columnar order is $k = 4133$. Since this is 200 times smaller than the maximum value of k that we have tested, it appears reasonable to conclude the number of systems with columnar order is finite.

If the conjecture that multiple transitions exist only if the high density phase is columnar [179] is true, then we conclude that for large k, the system shows one first order transition to a phase with sublattice order. In this case, the analogy to the hard disc problem in the two dimensional continuum, for which there are two transitions, breaks down. For each k, the k-NN model has a discrete symmetry. From our results for large k, it would appear that the continuous symmetry present in the hard disc model is not restored,

such that the limit $k \to \infty$ limit is different from $k = \infty$. This is unlike the q-state clock model with discrete symmetry where the continuous $U(1)$ symmetry of the XY model is restored for intermediate temperatures at large enough q. It would be interesting to test the conjecture more rigorously. One possibility is that even for systems with sublattice order, there could be two transitions. To show this, one needs to construct the high density expansion about the sublattice phase for large k and check whether certain defects are preferred over others.

Chapter 6

Columnar phase in systems of hard rectangles on square lattice–high density expansion

6.1 Introduction

In this chapter, we focus on the nematic-columnar transition in a system of hard rectangles on square lattice. Details of the nature of the transition and earlier findings are elaborated in Sec. 1.3.2. When $m = 2$, the critical density ρ_c (the fraction of occupied lattice sites) for this transition was numerically determined for d up to 48. By extrapolating to $d \to \infty$, it was shown that $\rho_c \approx \rho_c(\infty) + ak^{-1} + O(k^{-2})$, where the constants were estimated numerically to be $\rho_c(\infty) \approx 0.73$ and $a \approx 0.23$ [21], implying the existence of the columnar phase for infinitely long rectangles. As of now, unlike the nematic phase, there exists no rigorous proof for the existence of the columnar phase.

High-activity expansions are a systematic and more rigorous way of studying the effect of fluctuations in the ordered state. In the standard Mayer expansion, the high-activity

expansion is in integer powers of z^{-1}, where z is the activity or fugacity [10]. However, columnar phases possess a sliding instability resulting in the expansion being in fractional powers of z^{-1} [11]. The expansion was carried out to $O(z^{-3/2})$ for the hard square gas ($m = 2$, $d = 2$) recently [19], and the formalism was applied to hard core lattice gas models with first four next nearest neighbor exclusion, where the high-density phase is columnar [179].

In this chapter, we generalize the calculations of the hard square gas in Ref. [19] to derive the high-activity expansion for the columnar phase of the hard rectangle gas. To do so, we study a simpler model where rectangles may orient only in the horizontal direction. We expect the two models to have the same critical behaviour, and nearly same values of parameters like density and order parameter for a range of activities in which nematic order exists in the more general model. We justify this simplification by arguing that near the nematic-columnar transition, there are only a few rectangles with orientation perpendicular to the nematic orientation. We establish this by showing that the nematic-columnar transition densities are the same (within numerical error) for large k, whether both orientations or only one orientation is allowed. We show that the high-activity expansion is in powers of $z^{-1/d}$, where z is the activity or fugacity. The exact expressions for the first $d + 2$ terms in the expansion of free energy and densities are derived. Truncating the expansions for the densities at this order, we obtain estimates for the critical densities for the nematic-columnar transition. These estimates are lower bounds if the terms in the expansion do not change sign. For large m and k, these estimates are shown to decrease with increasing k and decreasing m.

The rest of the chapter is organized as follows. Section 6.2 contains a definition of the model and the justification for studying a model of hard rectangles with only horizontal orientation. The high-activity expansion for the free energy of $m \times d$ rectangles is derived in Sec. 6.3. In Sec. 6.4, we derive the high-activity expansion for the occupation densities of the different rows. The critical densities, and activities are estimated from these expan-

sions. Section 6.5 contains a discussion of the results and some possible extensions of the problem. The content of this chapter is published in Ref. [174].

6.2 Model and preliminaries

Consider a square lattice of size $L \times L$ with periodic boundary conditions. We consider a system of monodispersed hard rectangles of size $m \times d$, where $k = d/m$ is the aspect ratio, and $d \geq m$. A horizontal (vertical) rectangle occupies d (m) consecutive lattice sites along the x-direction and m (d) consecutive lattice sites along the y-direction. No lattice site may be occupied by more than one rectangle. The grand canonical partition function for the system is

$$\overline{\mathcal{L}}(z_h, z_v) = \sum_{n_h, n_v} \overline{C}(n_h, n_v) z_h^{n_h} z_v^{n_v}, \tag{6.1}$$

where $\overline{C}(n_v, n_h)$ is the number of valid configurations with n_h horizontal rectangles and n_v vertical rectangles, and z_h and z_v are the corresponding activities.

In the nematic and columnar phases, the orientational symmetry is broken, and thus the majority of rectangles are either horizontal or vertical. Typical snapshots of the system ($m = 2, d = 18$) at equilibrium near the nematic-columnar transition are shown in Fig. 6.1. The system has nearly complete orientational order, and one may ignore the effects of the rectangles with perpendicular orientation. To study the nematic–columnar phase transition, it is thus more convenient to study a system in which all rectangles are horizontal. Thus, we set $z_v = 0$ in Eq. (6.1), disallowing vertical rectangles.

Further justification of this simplification may be obtained by comparing the critical density ρ_c for the nematic-columnar transition for the model of rectangles with both orientations and the model of rectangles with only horizontal orientation. ρ_c for the model with both orientations allowed was numerically obtained for $m = 2$ as $\rho_c \approx 0.727 + 0.226k^{-1}$ for $k \gg 1$ [21]. Here, we obtain ρ_c for the model restricted to horizontal rectangles

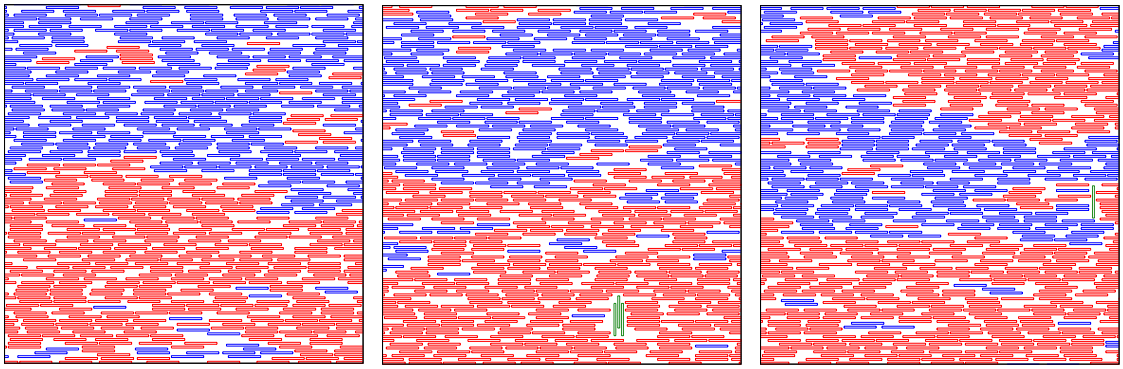

(a) (b) (c)

Figure 6.1: Snapshots of a system of rectangles of size $2 \times 18 (k = 9)$ at Monte Carlo time steps (a) 7×10^7, (b) 8×10^7, and (c) 9×10^7. Red and blue- are horizontal rectangles with heads at the even and odd rows respectively and green are vertical rectangles.

from Monte Carlo simulations. The details of the algorithm and parameters are as in Refs. [20, 21]. ρ_c is obtained for $m = 2$ by the intersection point of the Binder cumulant for three different lattice sizes, and is shown in Fig 6.2. We obtain $\rho_c \approx 0.727 + 0.226k^{-1}$ for $k \gg 1$, numerically indistinguishable from that for the model with both horizontal and vertical rectangles. We thus conclude that the simplified model is well-suited for studying the nematic-columnar transition. However, it is possible that the two models have qualitatively different phenomenology for small k when the nematic phase is absent for the model with both orientations allowed (also see Sec. 6.5 for more discussion of this point).

Let the bottom left corner of a rectangle be called its head. In the nematic phase, each row on an average contains equal number of heads of rectangles. In the columnar phase, this symmetry is broken. An example illustrating the two phases for 2×6 rectangles is shown in Fig. 6.3. In this and later figures, we have used the space filling convention, where a 2×6 rectangle corresponds to a rectangle of length 6 and breadth 2, and two rectangles may touch each other. To quantify the nematic–columnar transition, we assign to the i^{th} row a label $(i \mod m) + 1$, such that the labels are $1, \ldots, m$. In the columnar phase, majority of the rectangles have their heads on one of the m types of rows. The

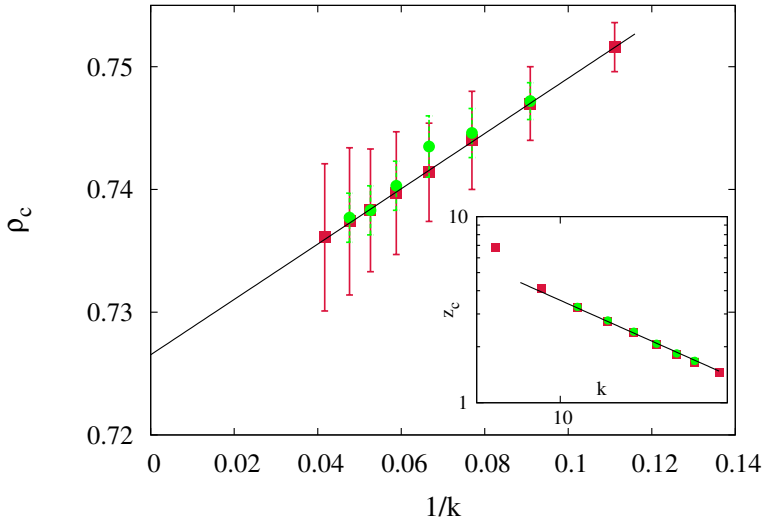

Figure 6.2: The critical density ρ_c for the nematic-columnar transition for the model with only horizontal rectangles (circles) and the model with both horizontal and vertical rectangles (squares) from Monte Carlo simulation. The data for the latter is from Ref. [21]. The straight line is $0.727 + 0.226k^{-1}$. Inset: The corresponding critical activity z_c from Monte Carlo simulation. The straight line is $35.5k^{-1}$.

grand canonical partition function for the model with only horizontal rectangles is then

$$\mathcal{L}(\{z_i\}) = \sum_{n_1,\ldots,n_m} C(n_1,\ldots,n_m) \prod_{i=1}^{m} z_i^{n_i}, \tag{6.2}$$

where $C(n_1,\ldots,n_m)$ is the number of configurations with n_i rectangles whose heads are on rows with label i, and z_i's are the corresponding activities. For large activities, the system will be in the columnar phase, and undergoes a transition to the nematic phase as the activities are decreased.

The free energy of the system in the thermodynamic limit is

$$f(z_1,\ldots,z_m) = \lim_{N\to\infty} -\frac{1}{N} \ln \mathcal{L}(z_1,\ldots,z_m), \tag{6.3}$$

where $N = L^2$ is the total number of lattice sites. The density of occupied sites ρ is then given by

$$\rho(z) = -mdz \frac{d}{dz} f(z,\ldots,z). \tag{6.4}$$

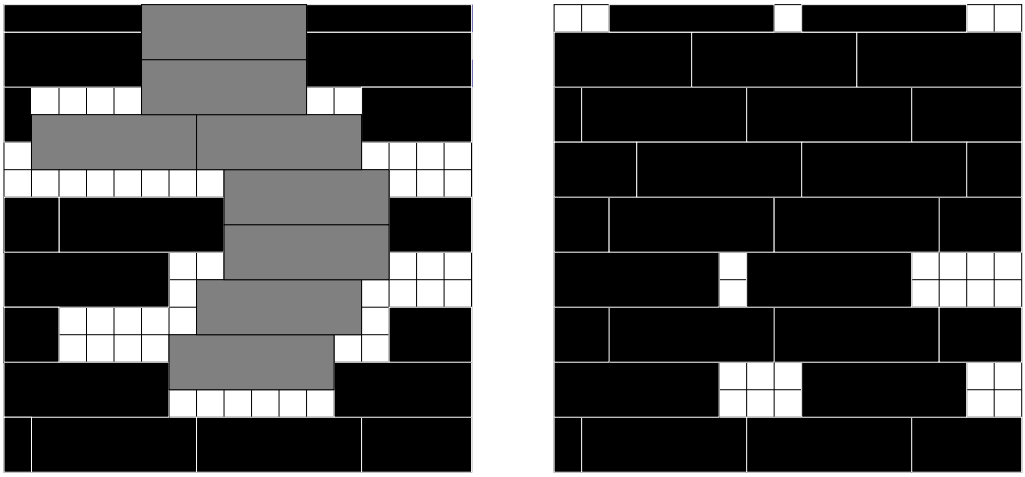

(a) (b)

Figure 6.3: A schematic diagram illustrating the two phases for 2×6 rectangles. In this and later figures, we have used the lattice filling convention in which rectangles are not allowed to touch each other (see text). (a) The low activity nematic phase where some of the heads (bottom left corner) of the rectangles are on odd rows (black) and some of the heads are on even rows (grey). (b) The high activity columnar phase where most of the heads of rectangles are either on even or odd rows (odd in the example shown).

The aim of the chapter is to determine the free energy f and density ρ as a perturbation series in inverse powers of the activity.

6.3 High activity expansion for the free energy

The perturbation series for the free energy will be in powers of $z^{-1/d}$ [see Sec. 6.3.1 and Eq. (6.19)] rather than the usual Mayer expansion in integer powers of z^{-1} because of the ordered columnar phase having a sliding instability [11, 19]. Suppose a vacancy is created in a fully ordered columnar phase at full packing by removing a rectangle. The d consecutive empty sites that are created may now be broken into d fractional vacancies with gain of entropy by sliding sets of rectangles in the horizontal direction. This breaking up of vacancies into fractional vacancies leads to fractional powers of z^{-1} appearing in the perturbation expansion.

To set up a perturbation expansion about the ordered columnar state, it is convenient to

choose one of the activities to be large and treat the other activities as small parameters:

$$z_1 = z_o, \tag{6.5}$$

$$z_2 = \ldots = z_m = z_e, \tag{6.6}$$

where $z_e \ll z_o$. The notation is such that when $m = 2$, o indicates odd rows and e indicates even rows. Once the perturbation expansion is obtained, z_o and z_e are equated to z to obtain the high-activity expansion.

In the completely ordered state, heads of all the rectangles are in rows with label 1 [see Fig. 6.3(b)]. In the perturbation expansion, we refer to rectangles whose heads are in rows with a label different from 1 as defects. For systems with sliding instability, the perturbation expansion is not in terms of number of defects, but rather in terms of clusters of defects [11, 19]. We illustrate this for the case $m = 2$. Consider a single defect on a row with label 2 [see Fig. 6.4(a)]. This defect results in one or more rectangles removed from each of the two rows denoted by $*$ in Fig. 6.4(a), both with label 1, and therefore has leading weight z^{-1}. Now consider two defects both on rows with label 2 but one directly above the other [see Fig. 6.4(b)]. This cluster of defects results in one or more rectangles removed from each of the three rows denoted by $*$ in Fig. 6.4(b), all three with label 1, and therefore still has leading weight z^{-1}. It is easy to see that a similar defect cluster of arbitrary size will have leading weight z^{-1}. When $m > 2$, defect-clusters may have defects with different labels (as defined below). For such clusters, it is again possible that defect-clusters of different sizes also have leading weight z^{-1}.

We define a single cluster of defects more precisely. Let a sub-cluster of size n and label j denote a set of n rectangles of label j, directly on top of each other such that the long sides are parallel and the short sides are aligned. A single cluster of defects is made up of sub-clusters of label $2, 3, \ldots m$, such that the labels are in ascending order and the gap between two sub-clusters is the minimum possible. Examples of single clusters of size 4 for 3×6 rectangles are shown in Fig. 6.5. In Fig. 6.5(a), the cluster is made up of a single

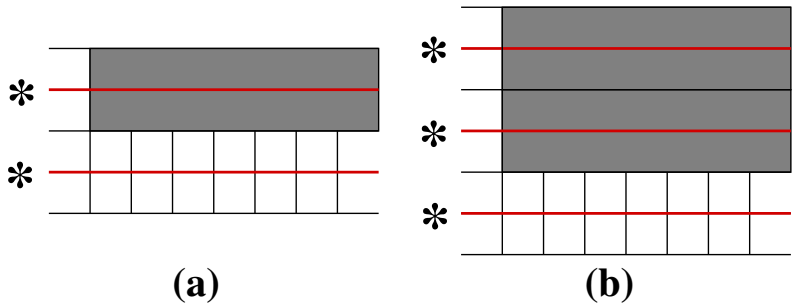

Figure 6.4: A schematic diagram illustrating clusters. (a) One rectangle on an even row results in reducing the maximal occupancy of two odd rows (red lines labeled $*$) by one. (b) Two rectangles on even rows one directly above the other results in reducing the maximal occupancy of three odd rows (red lines labeled $*$) by one.

sub-cluster of label 2 while in Fig. 6.5(b), the cluster is made up of one sub-cluster of size 2 of label 2 and one sub-cluster of size 2 of label 3. It is straightforward to check that all such single cluster of defects will have leading weight z^{-1}.

The perturbation expansion is well-defined in terms of number of clusters [11, 19]. Thus, we write

$$\frac{\mathcal{L}(z_o, z_e)}{\mathcal{L}(z_o, 0)} = 1 + W_1(z_o, z_e) + W_2(z_o, z_e) + \dots, \tag{6.7}$$

where W_n represents the contribution from n clusters. The free energy may then written as a series:

$$f(z_o, z_e) = f_0(z_o) + f_1(z_o, z_e) + f_2(z_o, z_e) + \dots, \tag{6.8}$$

where f_i corresponds to the contribution from i clusters. From Eq. (6.3), we immediately obtain

$$f_0(z_o) = \lim_{N\to\infty} \frac{-1}{N} \ln \mathcal{L}(z_o, 0), \tag{6.9}$$

$$f_1(z_o, z_e) = \lim_{N\to\infty} \frac{-1}{N} W_1(z_o, z_e), \tag{6.10}$$

$$f_2(z_o, z_e) = \lim_{N\to\infty} \frac{-1}{N} \left[W_2(z_o, z_e) - \frac{W_1(z_o, z_e)^2}{2} \right]. \tag{6.11}$$

The free energies f_0, f_1 and f_2 are calculated in the following subsections.

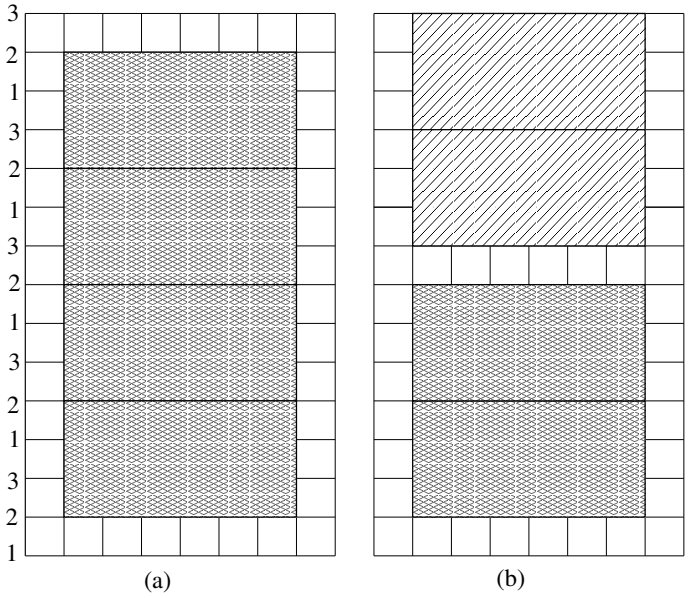

Figure 6.5: An example of a single cluster of size 4 made up of (a) 4 defects of label 2 and (b) 2 defects of label 2 and 2 defects of label 3. The example is for rectangles of size 3×6.

6.3.1 Calculation of f_0

f_0 is the contribution to the free energy from configurations that do not have defects. Then the heads of all the rectangles are in rows with label 1 and the configuration in a particular row is independent of the configurations in other rows, Hence, we can write

$$\mathcal{L}(z_o, 0) = \left[\Omega_p(z_o, L)\right]^{L/m}, \tag{6.12}$$

where $\Omega_p(z_o, L)$ is the grand canonical partition function of a system of hard rods of length d on a one dimensional lattice of L sites with periodic boundary condition. The one dimensional partition function obeys simple recursion relations. $\Omega_p(z_o, L)$ is related to $\Omega_o(z_o, L)$, the corresponding grand canonical partition function on a one dimensional lattice of L sites with open boundary conditions, as

$$\Omega_p(z, L) = dz\Omega_o(z, L - d) + \Omega_o(z, L - 1),\ L \geq d. \tag{6.13}$$

$\Omega_o(z,\ell)$ obeys the following recursion relation:

$$\Omega_o(z,\ell) = z\Omega_o(z,\ell-d) + \Omega_o(z,\ell-1),\ \ell \geq d, \tag{6.14}$$

$$\Omega_o(z,\ell) = 1,\ 0 \leq \ell < d. \tag{6.15}$$

Equation (6.14) is solved by the ansatz $\Omega_o(z,\ell) = A\lambda^\ell$, where A is a constant. Substituting into Eq. (6.14), we obtain

$$\lambda^d - \lambda^{d-1} - z = 0. \tag{6.16}$$

Let λ_1 denote the largest root of Eq. (6.16). For arbitrary d, λ_1 may be solved as a perturbation series in inverse powers of z^{-1}. By examining a few terms in the expansion, we find that the series solution of λ_1 has the following form:

$$\lambda_1(z) = z^{1/d} + \frac{1}{d} + \sum_{n=1}^{\infty} \frac{z^{-n/d}}{d^{n+1}(n+1)!} \prod_{j=1}^{n}(jd-n). \tag{6.17}$$

The expansion Eq. (6.17) coincides with the exact solution of Eq. (6.16) for $d = 2$. By substituting into Eq. (6.16), we have checked that the first 102 terms of Eq. (6.17) are correct for $d = 3, 4, \ldots, 10$. Also, for $z = 10, 15, 20$, we check that Eq. (6.16) is satisfied by Eq. (6.17) for $d = 2, 3, \ldots 100$.

The free energy f_0 is related to the λ_1 as

$$f_0 = -\frac{1}{m} \ln \lambda_1(z_0). \tag{6.18}$$

Thus,

$$f_0 = -\frac{\ln z_o}{dm} - \frac{z_o^{-1/d}}{dm} - \sum_{n=2}^{\infty} \frac{z_o^{-n/d}}{n!d^n m} \prod_{j=1}^{n-1}(jd-n). \tag{6.19}$$

Note that f_0 is a series in integer powers of $z_o^{-1/d}$ rather than the usual Mayer expansion that is in integer powers of z_o^{-1}.

It will turn out later that, to calculate the contribution from configurations with two defect-

clusters, we will need knowledge of the partition function $\Omega_o(z,\ell)$ for all ℓ and not just for large ℓ for which only the largest root λ_1 of Eq. (6.16) contributes. $\Omega_o(z,\ell)$ is a linear combination of the d roots of Eq. (6.16). Denoting the roots by λ_n,

$$\Omega_o(z,\ell) = \sum_{n=1}^{d} c_n \lambda_n^{\ell}, \tag{6.20}$$

where c_n are constants to be determined from Eq. (6.15). Substituting Eq. (6.20) in Eq. (6.15) we obtain

$$\begin{pmatrix} 1 & 1 & 1 & \dots & 1 \\ \lambda_1 & \lambda_2 & \lambda_3 & \dots & \lambda_d \\ \lambda_1^2 & \lambda_2^2 & \lambda_3^2 & \dots & \lambda_d^2 \\ \dots & \dots & \dots & \dots & \dots \\ \dots & \dots & \dots & \dots & \dots \\ \lambda_1^{d-1} & \lambda_2^{d-1} & \lambda_3^{d-1} & \dots & \lambda_d^{d-1} \end{pmatrix} \begin{pmatrix} c_1 \\ c_2 \\ \cdot \\ \cdot \\ \cdot \\ c_d \end{pmatrix} = \begin{pmatrix} 1 \\ 1 \\ \cdot \\ \cdot \\ \cdot \\ 1 \end{pmatrix}. \tag{6.21}$$

By inverting the Vandermonde matrix in Eq. (6.21), we obtain

$$c_n = (-1)^{d-1} \frac{\prod_{\substack{j=1 \\ j\neq n}}^{d} (\lambda_j - 1)}{\prod_{\substack{j=1 \\ j\neq n}}^{d} (\lambda_n - \lambda_j)}, \tag{6.22}$$

To obtain c_n's as a series in $z_o^{-1/d}$, we need to first obtain all λ_n's as a series in $z_o^{-1/d}$. From Eq. (6.16), we immediately notice that $|\lambda_n| = z^{1/d}$, $z \to \infty$. Let

$$\lambda_n = z^{1/d} e^{i\theta_n}. \tag{6.23}$$

Substituting into Eq. (6.16), we obtain

$$e^{i\theta_n d} = 1 + z^{-1/d} e^{i\theta_n (d-1)}. \tag{6.24}$$

The perturbative solution to Eq. (6.24) is straightforward to obtain:

$$\lambda_n = z^{1/d} e^{i\theta_n} + \frac{1}{d} + \frac{(d-1)e^{-i\theta_n}}{2d^2} z^{-1/d} + O(z^{-2/d}), \tag{6.25}$$

where

$$\theta_n = \frac{2(n-1)\pi}{d}, \quad n = 1, 2, \ldots, d. \tag{6.26}$$

Using the expression for c_n's in Eq. (6.22), we obtain

$$c_n = \frac{1}{d} + \frac{(d-1)e^{-i2\pi(n-1)/d}}{d^2} z^{-1/d} + \ldots, \; n = 1, \ldots, d. \tag{6.27}$$

6.3.2 Calculation of f_1

A single cluster of defects of size n consists of n rectangles placed one directly above the other, keeping the long sides parallel, with the heads being in rows with labels $2, \ldots, m$ (see text before Eq. (6.7) for a more precise definition). Given a defect-cluster of size n, the occupation of exactly $n+1$ rows with label 1 are affected. The contribution to W_1 from a single defect cluster of size n is then $\left[\frac{\Omega_o(z_o, L-d)}{\Omega_p(z_o, L)}\right]^{n+1} z_e^n$. The bottom left corner of the cluster has to be on a row with label 2, and there are N/m ways of choosing this lattice site. In addition, we need to account for the number of ways $H(n)$ that a cluster of size n may be split into sub-clusters with different labels. The number of ways of distributing n rectangles into $m-1$ sub-clusters, where the sub-clusters are arranged in ascending order of labels, is

$$H(n) = \binom{n+m-2}{m-2}. \tag{6.28}$$

Thus, the contribution to W_1 from configurations with a single cluster of defects is

$$W_1(z_o, z_e) = \frac{N}{m} \sum_{n=1}^{\infty} H(n) \left[\frac{\Omega_o(z_o, L-d)}{\Omega_p(z_o, L)} \right]^{n+1} z_e^n, \tag{6.29}$$

$$= \frac{N}{m} \frac{\Omega_o(z_o, L-d)}{\Omega_p(z_o, L)} \left[\frac{1}{\left[1 - \frac{z_e \Omega_o(z_o, L-d)}{\Omega_p(z_o, L)}\right]^{m-1}} - 1 \right]. \tag{6.30}$$

$\Omega_p(z_o, L)$ may be expressed in terms of $\Omega_o(z_o, L)$ using Eq. (6.13):

$$\Omega_p(z_o, L) = \Omega_o(z_o, L-d) \left[dz_o + \frac{\Omega_o(z_o, L-1)}{\Omega_o(z_o, L-d)} \right], \tag{6.31}$$

$$\underset{L\to\infty}{=} \Omega_o(z_o, L-d) \left[dz_o + \lambda_1^{d-1} \right]. \tag{6.32}$$

where in the limit $L \to \infty$, we used $\Omega_o(z_o, \ell) \sim \lambda_1^{\ell}$. Substituting into Eq. (6.30), using Eq. (6.10), setting $z_e = z_o = z$, and expanding for large z, we obtain,

$$f_1(z, z) = \frac{-1}{mdz} \left[\frac{d^{m-1}}{(d-1)^{m-1}} - 1 \right] + \frac{1}{md^2 z^{1+1/d}} \left[\frac{d^{m-1}(d+m-2)}{(d-1)^m} - 1 \right] + O\left(\frac{1}{z^{1+2/d}} \right). \tag{6.33}$$

Thus single clusters of defects contribute at $O(z^{-1})$.

6.3.3 Calculation of f_2

f_2 is the contribution to the free energy from two defect-clusters. There are four types of possible configurations:

(a) Clusters that are separated by at least one row of label 1 that may be occupied with rectangles independent of other rows.

(b) Clusters that intersect.

(c) Clusters that do not have any overlap in the y-direction, and are not of type (a) or (b).

(d) Clusters that have some overlap in the y-direction, and are not of type (b).

We calculate the contribution from each of these types in the following subsections.

Type (a): Clusters that are separated from each other

The contribution of clusters of type (a) to the free energy is exactly cancelled by the contribution from the product of two single clusters W_1^2 [which is $O(z^{-2})$]. Thus, there is no contribution to the free energy.

Type (b): Clusters that intersect

When two clusters intersect, W_2 is exactly zero since such configurations are forbidden. However, there is a contribution to f_2 from such configurations through the terms W_1^2. Since W_1 is $O(z^{-1})$, the contribution to f_2 is $O(z^{-2})$. Later, we will not be keeping terms of $O(z^{-2})$, and we therefore neglect the contribution to f_2 from such configurations.

Type (c): Clusters that do not overlap in the y-direction

Let $W_2^x(z_o, z_e)$ denote the contribution to $W_2(z_o, z_e)$ from configurations of clusters that have no overlap in the y-direction, but may overlap in the x-direction. Examples of such configurations are shown in Fig. 6.6. Let the number of defects in the clusters be denoted by n_a and n_b, and let Δ denote the distance in the x direction between the centers of the two clusters, where $\Delta \geq 1$. When $\Delta < d$, the two clusters have some overlap in the x-direction [see Fig. 6.6(a)], otherwise not [see Fig. 6.6(b)].

Let t_1 (t_2) denote the contribution to W_2^x from pairs with $\Delta < d$ ($\Delta \geq d$). We calculate t_1 and t_2 separately. For t_1, not all pairs of clusters with the same Δ contribute at the same

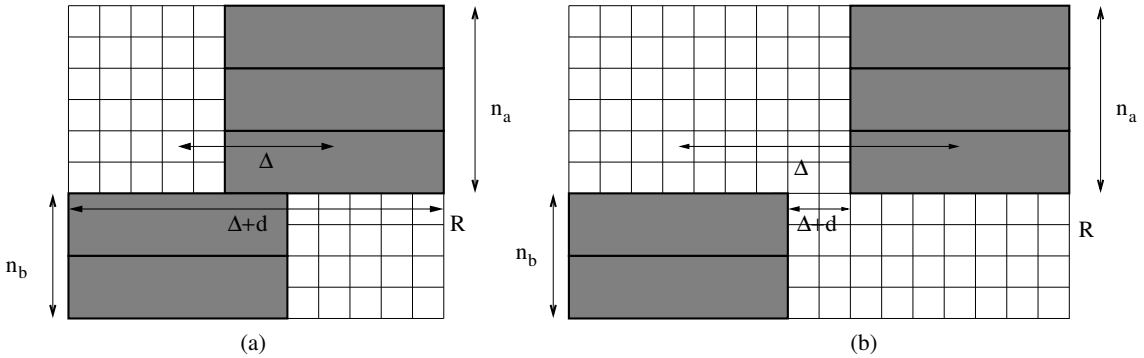

Figure 6.6: Examples of configurations of two clusters with no overlap in the y-direction. Δ is the distance between the centers of the two clusters in the x-direction. Clusters could overlap in the x-direction as in (a) $1 \leq \Delta < d$, or have no overlap in the x-direction as in (b) $\Delta \geq d$.

order in z. The lowest order contribution appears from pair of clusters where the smallest label of the defects in the upper cluster is larger than or equal to largest label of the defects in the lower cluster. Other pairs of clusters contribute at $O(z^{-2})$. This may be easily seen in the example shown in Fig 6.7, where two cluster configurations are shown for the case $m = 3$. In Fig 6.7(a), the largest label of lower cluster is 3 and the smallest label of the upper cluster is also 3. Such a configuration of four defects affects five rows of label 1 (denoted by bold lines) and contributes at $O(z^{-1})$. In Fig 6.7(b), the largest label of lower cluster is 3 but the smallest label of the upper cluster is now 2. Such a configuration of four defects affects six rows of label 1 (denoted by bold lines), contributing at $O(z^{-2})$.

For the calculation of t_1, we will, therefore, restrict ourselves to cluster configurations where the smallest label of the defects in the upper cluster is larger than or equal to largest label of the defects in the lower cluster. In this case, the upper cluster may be slid to the left by Δ till the two clusters merge to form a single cluster. Thus, the combinatorial factor associated with dividing the two clusters into sub-clusters of different labels is, as in the case of single clusters [see Sec. 6.3.2 and Eq. (6.28)], $H(n_a + n_b)$, where n_a and n_b are the number of defects in the top and bottom clusters respectively. For t_2 ($\Delta \geq d$), the labels in each cluster are independent of each other, and the combinatorial factor is therefore equal to $H(n_a)H(n_b)$. In addition, for both t_1 and t_2, since we restrict $\Delta \geq 1$, a symmetry factor 2 is associated with each configuration.

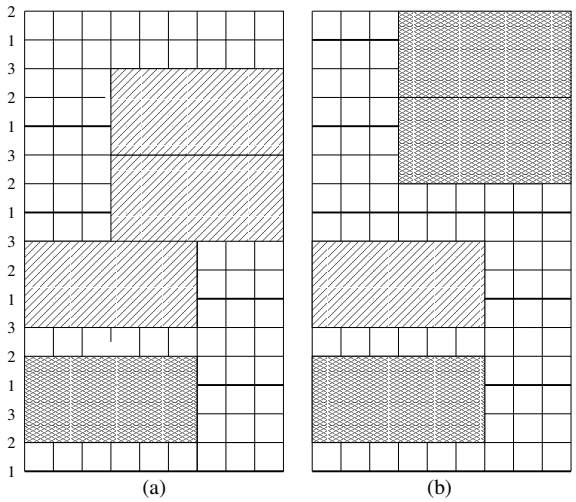

Figure 6.7: Examples of configurations with two defect-clusters when $m = 3$. (a) The lower cluster has two defects of labels 2 and 3 while the upper cluster has two defects of label 3. Such a configuration affects the occupation of five rows of label 1 (shown by bold lines). (b) The upper clusters has two defects of label 2. Such a configuration affects the occupation of 6 rows of label 1 (shown by bold lines).

We now calculate the contribution to t_1 and t_2 from the occupation of rows of label 1 with rectangles. The occupation of $n_a + n_b + 1$ rows of label 1 with rectangles are affected by the presence of the defects. The remaining rows of label 1 may be filled independently of each other. Among the $n_a + n_b + 1$ rows, other than the row marked by R in Fig. 6.6(a) and (b), $n_a + n_b$ rows may be thought of as open chains of length $L - d$. When $\Delta < d$ [see Fig. 6.6(a)], the row R is equivalent of an open chain of length $L - d - \Delta$. When $\Delta \geq d$ [see Fig. 6.6(b)], the row R is equivalent of two open chains of lengths $\Delta - d$ and $L - 2d - (\Delta - d)$. Thus, we obtain

$$t_1 = \frac{2N}{m} \sum_{n_a,n_b=1}^{\infty} H(n_a + n_b) \left[\frac{\Omega_o(z_o, L-d) z_e}{\Omega_p(z_o, L)} \right]^{n_a+n_b} \sum_{\Delta=1}^{d-1} \frac{\Omega_o(z_o, L-d-\Delta)}{\Omega_p(z_o, L)}, \tag{6.34}$$

and

$$t_2 = \frac{2N}{m} \sum_{n_a,n_b=1}^{\infty} H(n_a) H(n_b) \left[\frac{\Omega_o(z_o, L-d) z_e}{\Omega_p(z_o, L)} \right]^{n_a+n_b} \times \sum_{\Delta=d}^{\infty} \frac{\Omega_o(z_o, L-d-\Delta) \Omega_o(z_o, \Delta-d)}{\Omega_p(z_o, L)}, \tag{6.35}$$

where the factor N/m accounts for the number of ways of placing the lower cluster on sublattice 2.

In the limit $L \to \infty$, $\Omega_p(z_o, L)$ may be expressed in terms of $\Omega_o(z_o, L)$ using Eq. (6.32). The limit of large L does not apply to the term $\Omega_o(z_o, \Delta - d)$, as $\Delta - d$ may be as small as zero. Hence, we use Eq. (6.20) for the one dimensional partition function for any length. We, then, obtain

$$t_1 = \frac{2N}{m} \sum_{n_a,n_b=1}^{\infty} H(n_a + n_b) \left[\frac{z_e}{dz_o + \lambda_1^{d-1}} \right]^{n_a+n_b} \sum_{\Delta=1}^{d-1} \frac{\lambda_1^{-\Delta}}{dz_o + \lambda_1^{d-1}}, \tag{6.36}$$

and

$$t_2 = \frac{2N}{m} \sum_{n_a,n_b=1}^{\infty} H(n_a)H(n_b) \left[\frac{z_e}{dz_o + \lambda_1^{d-1}} \right]^{n_a+n_b} \sum_{\Delta=d}^{\infty} \sum_{j=1}^{d} \frac{c_1 \beta_j \alpha_j^{\Delta-d}}{\lambda_1^d (dz_o + \lambda_1^{d-1})}, \tag{6.37}$$

where

$$\beta_j = \frac{c_j}{c_1}, \tag{6.38}$$

$$\alpha_j = \frac{\lambda_j}{\lambda_1}, \tag{6.39}$$

with c_j and λ_j as defined in Eq. (6.20). Knowing the perturbation expansion for c_j [see Eq. (6.27)] and λ_j [see Eqs. (6.17) and (6.25)], the perturbation expansion for β_j and α_j may be derived to be

$$\beta_j = 1 + \frac{d-1}{dz_o^{1/d}} \left[e^{-i2\pi(j-1)/d} - 1 \right] + O(z_o^{-2/d}), \quad j = 2, \ldots, d, \tag{6.40}$$

$$\alpha_j = e^{i\theta_j} + \frac{1}{dz_o^{1/d}} (1 - e^{i\theta_j}) + O(z_o^{-2/d}), \quad j = 2, \ldots, d, \tag{6.41}$$

$$\frac{1}{1-\alpha_j} = \frac{1}{1-e^{i\theta_j}} \left(1 + \frac{1}{dz_o^{1/d}} \right) + O(z_o^{-2/d}), \quad j = 2, \ldots, d, \tag{6.42}$$

where θ_j is as defined in Eq. (6.26).

We now focus on t_2 [see Eq. (6.37)]. Since $|\alpha_j| < 1$ for $j > 1$, the sum over Δ reduces to a

convergent geometric series for $j > 1$. Summing over Δ, we obtain

$$t_2 = \frac{2N}{m} \sum_{n_a,n_b=1}^{\infty} H(n_a)H(n_b) \left(\frac{z_e}{dz_o + \lambda_1^{d-1}} \right)^{n_a+n_b} \times \left[\sum_{\Delta=d}^{\infty} \frac{c_1}{\lambda_1^d (dz_o + \lambda_1^{d-1})} + \sum_{j=2}^{d} \frac{c_1 \beta_j}{\lambda_1^d (dz_o + \lambda_1^{d-1})(1-\alpha_j)} \right] \tag{6.43}$$

Though the first term in Eq. (6.43) is divergent, in the calculation for f_2, it may be checked that this term is cancelled by the term $-W_1^2/2$. From Eq. (6.27) $c_1 \sim d^{-1}$, and Eq. (6.40) $\beta_j \sim O(1)$. Similarly $|\alpha_j| \sim 1$, though $\alpha_j \neq 1$ for $j > 1$ [see Eq. (6.41)]. Also $\lambda_1 \sim z^{1/d}$ [see Eq. (6.17)]. Therefore, we obtain that the second term in Eq. (6.43) is $O(z_o^{-2})$. Therefore, we conclude that $t_2 \sim O(z^{-2})$.

In the expression for t_1 [see Eq. (6.36)], the leading order of the term for a fixed Δ is $z^{-1-\Delta/d}$. Keeping only the $\Delta = 1$ term, we obtain

$$W_2^x = \frac{2N}{m} \sum_{n_a,n_b=1}^{\infty} \frac{H(n_a+n_b)}{dz_o^{1+1/d}} \left(\frac{z_e}{dz_o} \right)^{n_a+n_b} + O(z^{-1-2/d}). \tag{6.44}$$

Doing the summation and setting $z_e = z_o = z$, we obtain

$$W_2^x = \frac{2N}{mdz^{1+1/d}} \left[1 - \frac{d^{m-1}(d-m)}{(d-1)^m} \right] + O(z^{-1-2/d}). \tag{6.45}$$

Type (d): Clusters that overlap in the y-direction

Two non-intersecting rectangles of different labels are said to overlap in the y-direction if the y-coordinate of the head of the rectangle with larger label lies within the y-range of the rectangle with smaller label. Two rectangles of same label are said to overlap in the y-direction if their heads are on the same row. Two defect-clusters are said to overlap in the y-direction if they contain at least one pair of overlapping rectangles. Let W_2^y denote the contribution from configurations with two defect-clusters that have some overlap in the y-direction. We divide such configurations into four types, as shown in Fig. 6.8, with their

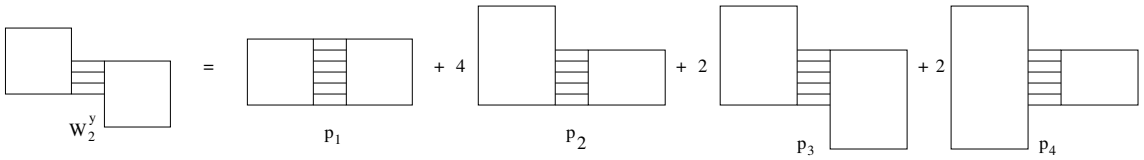

Figure 6.8: Four possible cases of two clusters with overlap along y. In p_1, both clusters do not extend beyond the common section. In p_2, one of the clusters extends beyond the common section in one direction. In p_3, both clusters extend beyond the common section. In p_4, one of the clusters extends beyond the common section in both directions. The numbers come from symmetry considerations and is straightforward to obtain.

contributions to W_2^y being denoted by p_1, p_2, p_3 and p_4. In p_1, neither of the clusters has any extension beyond the common section. In p_2, one of the clusters extends beyond the common section in one direction. In p_3, both clusters extend beyond the common section in mutually opposite directions, while in p_4, one cluster extends beyond the common section in both directions. Each of the two clusters are single clusters as defined in 6.3.2 (also see Fig. 6.4). The configurations of type p_2, p_3 and p_4 may occur in four, two and two ways respectively, depending on which of the clusters is extending beyond the common section and in which direction.

For a pair of clusters, let n_0 denote the number of rectangles that overlap in the y-direction. Let the number of rectangles in the sections extending above and below the common section be denoted by n_a and n_b respectively. As in Sec. 6.3.3, let Δ be the horizontal distance between the centers of the two clusters. Clearly $\Delta \geq d$. These symbols are illustrated in an example in Fig. 6.9.

We now calculate p_1, p_2, p_3 and p_4. For p_1, the presence of the defect-clusters affects the occupation of exactly $(n_0 + 1)$ rows of label 1. The occupation of each of these rows with rectangles is equivalent to occupying two open chains of length $\Delta - d$ and $L - d - \Delta$. Also, for each of the clusters, the number of ways of breaking it up into sub-clusters is $H(n_0)$. Thus,

$$p_1 = \frac{N}{m} \sum_{n_0=1}^{\infty} \sum_{\Delta=d}^{\infty} H(n_0)^2 \left[\frac{\Omega_o(z_o, L-d-\Delta)\Omega_o(z_o, \Delta-d)}{\Omega_p(z_o, L)} \right]^{n_0+1} z_e^{2n_0}. \tag{6.46}$$

Expressing Ω_p in terms of Ω_o using Eq. (6.32), and $\Omega_o(z_o, \Delta - d)$ in terms of λ_j using

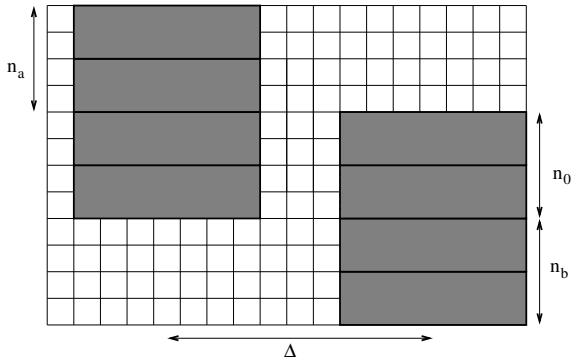

Figure 6.9: An example ($m = 2$, $d = 7$) illustrating the definition of n_0, n_a, n_b, and Δ. n_0 is the number of rectangles in the common section (2 in example), n_a and n_b are the extensions above and below (2 each) and Δ is the horizontal distance between the centers of the two clusters (10 in example).

Eq.(6.20), we obtain

$$p_1 = \frac{N}{m} \sum_{n_0=1}^{\infty} \sum_{\Delta=d}^{\infty} H(n_0)^2 \left[\frac{c_1 \sum_{j=1}^{d} \beta_j \alpha_j^{\Delta-d}}{\lambda_1^d (dz_o + \lambda_1^{d-1})} \right]^{n_0+1}, \tag{6.47}$$

where β_j and α_j are as defined in Eq. (6.40) and Eq.(6.41). Expanding the last term in Eq. (6.47) using multinomial expansion, we obtain

$$\begin{aligned} p_1 = \frac{N}{m} \sum_{n_0=1}^{\infty} H(n_0)^2 z_e^{2n_0} \left[\frac{c_1}{\lambda_1^d (dz_o + \lambda_1^{d-1})} \right]^{n_0+1} \\ \times \sum_{\{n_l\} \geq 0}{}' \frac{(n_0+1)!}{\prod_{j=1}^{d} n_j!} \sum_{\Delta=d}^{\infty} \prod_{p=2}^{d} (\beta_p \alpha_p^{\Delta-d})^{n_p}, \end{aligned} \tag{6.48}$$

where the primed sum refers to the constraint

$$\sum_{i=1}^{d} n_i = n_0 + 1. \tag{6.49}$$

Summing over Δ, we obtain

$$p_1 = \frac{N}{m}\sum_{n_0=1}^{\infty} H(n_0)^2 z_e^{2n_0}\left[\frac{c_1\lambda_1^{-d}}{dz_o+\lambda_1^{d-1}}\right]^{n_0+1}\sum_{\{n_l\}\geq 0}{}' \frac{(n_0+1)!\prod_{p=2}^{d}\beta_p^{n_p}}{\prod_{s=1}^{d} n_s![1-\prod_{j=2}^{d}\alpha_j^{n_j}]}. \tag{6.50}$$

We now estimate the order of the different terms in Eq. (6.50). From Eq. (6.27) $c_1 \sim 1/d$ and from Eq. (6.25), $\lambda_1^d \sim z_o$. Hence

$$\frac{c_1\lambda_1^{-d}}{dz_o+\lambda_1^{d-1}} \sim \frac{1}{(dz_o)^2}. \tag{6.51}$$

To leading order, $\beta_i = 1$, for all i [see Eq. (6.40)]. Hence, unless the term $1-\prod_{j=2}^{d}\alpha_j^{n_j}$ in Eq. (6.50), goes to zero as $z\to\infty$, the summand is $O(z^{-2})$. Since we are not interested in terms of $O(z^{-2})$, we focus only on those $\{n_l\}$ for which $\prod_{j=2}^{d}\alpha_j^{n_j} \approx 1$, when $z\to\infty$. We obtain from Eq. (6.41)

$$\prod_{j=2}^{d}\alpha_j^{n_j} = e^{\sum_{j=2}^{d} i\theta_j n_j}\left[1-\sum_{j=2}^{d}\frac{(1-e^{-i\theta_j})n_j}{dz_o^{1/d}}\right] + O(z_0^{-2/d}). \tag{6.52}$$

We are interested in those $\{n_l\}$ for which the leading term of the product is 1. This leads to the constraint

$$\sum_{j=2}^{d}\theta_j n_j = 2l\pi, \quad l\in\mathbb{Z}, \tag{6.53}$$

such that,

$$1-\prod_{j=2}^{d}\alpha_j^{n_j} = \sum_{j=2}^{d}\frac{(1-e^{-i\theta_j})n_j}{dz_o^{1/d}}. \tag{6.54}$$

Let

$$I(n_0) = \sum_{\{n_l\}\geq 0}{}'' \frac{1}{\prod_{j=1}^{d} n_j!\sum_{j=2}^{d}(1-e^{-i\theta_j})n_j}, \tag{6.55}$$

where the double prime refers to the constraints Eqs. (6.49) and (6.53). It is straightforward to see that $I(n_0)$ is real. α_j's appear as complex conjugate pairs. For every $\{n_l\}$

satisfying the constraints, there is a $\{n_l'\}$ obtained by interchanging the n_l's of all complex conjugate pairs, the corresponding summand being the complex conjugate. Thus $I(n_0)$ is real. Equation (6.50) then reduces to

$$p_1 = \frac{N}{m} \sum_{n_0=1}^{\infty} H(n_0)^2 \left(\frac{z_e}{dz_o} \right)^{2n_0} \frac{(n_0+1)! I(n_0)}{dz_o^{2-1/d}} + O(z^{-2}). \tag{6.56}$$

Thus p_1 is of order $z^{2-1/d}$ and for $d > 2$ does not contribute to order $z^{1+1/d}$.

For configurations of type p_2, one of the clusters extends beyond the other, the two clusters being of length n_o and $n_0 + n_a$, where the common section in the y-direction has n_o rectangles. The presence of these defect-clusters affects the occupation of $(n_o + n_a + 1)$ rows of label 1. Out of these rows, $n_o + 1$ of them are equivalent to open chains of length $\Delta - d$ and $L - d - \Delta$, and the remaining n_a are equivalent to an open chain of length $L - d$. The number of ways of dividing the clusters into sub-clusters is $H(n_0 + n_a)H(n_0)$. In addition, there is a factor of $4N/m$ from symmetry considerations. Thus,

$$\begin{aligned} p_2 = \frac{4N}{m} \sum_{n_0,n_a=1}^{\infty} \sum_{\Delta=d}^{\infty} & H(n_0)H(n_0+n_a) z_e^{2n_0+n_a} \\ & \times \left[\frac{\Omega_o(z_o, L-d)}{\Omega_p(z_o, L)} \right]^{n_a} \left[\frac{\Omega_o(z_o, L-d-\Delta)\Omega_o(z_o, \Delta-d)}{\Omega_p(z_o, L)} \right]^{n_0+1}. \end{aligned} \tag{6.57}$$

For configurations of type p_3, both clusters extend beyond the common section in the y-direction, one cluster being of length $n_0 + n_a$ and the other being of length $n_0 + n_b$. The number of ways of dividing the clusters into sub-clusters is $H(n_0 + n_a)H(n_0 + n_b)$. For configurations of type p_4, one cluster extends beyond the common section in both directions, one cluster being of length $n_0 + n_a + n_b$ and the other being of length n_0. The number of ways of dividing the clusters into sub-clusters is $H(n_0+n_a+n_b)H(n_0)$. For both p_3 and p_4 the presence of the defect-clusters affects the occupation of $(n_o + n_a + n_b + 1)$ rows of label 1. Out of these rows, $n_o + 1$ of them are equivalent to open chains of length $\Delta - d$ and $L - d - \Delta$, and the remaining $n_a + n_b$ are equivalent to an open chain of length

$L-d$. Each of these two types also has an additional factor of $2N/m$ due to symmetry considerations. Thus, we obtain

$$p_3 = \frac{2N}{m}\sum_{n_a=1}^{\infty}\sum_{n_b=1}^{\infty}\sum_{\Delta=d}^{\infty}\sum_{n_0=1}^{\infty} H(n_0+n_a)H(n_0+n_b)z_e^{2n_0+n_a+n_b} \times\left[\frac{\Omega_o(z_o,L-d)}{\Omega_p(z_o,L)}\right]^{n_a+n_b}\left[\frac{\Omega_o(z_o,L-d-\Delta)\Omega_o(z_o,\Delta-d)}{\Omega_p(z_o,L)}\right]^{n_0+1}, \tag{6.58}$$

and

$$p_4 = \frac{2N}{m}\sum_{n_a=1}^{\infty}\sum_{n_b=1}^{\infty}\sum_{\Delta=d}^{\infty}\sum_{n_0=1}^{\infty} H(n_0+n_a+n_b)H(n_0)z_e^{2n_0+n_a+n_b} \times\left[\frac{\Omega_o(z_o,L-d)}{\Omega_p(z_o,L)}\right]^{n_a+n_b}\left[\frac{\Omega_o(z_o,L-d-\Delta)\Omega_o(z_o,\Delta-d)}{\Omega_p(z_o,L)}\right]^{n_0+1}. \tag{6.59}$$

The expressions for p_2 [see Eq. (6.57)], p_3 [see Eq. (6.58)] and p_4 [see Eq. (6.59)] are similar to that for p_1 [see Eq. (6.46)] except for the factor $z_e^{n_a+n_b}[\Omega_o(z_o,L-d)/\Omega_p(z_o,L)]^{n_a+n_b}$. However, this factor is $O(z^0)$. Hence, p_2, p_3, and p_4 are also of $O(z^{-2+1/d})$. Combining the contributions from p_1, p_2, p_3 and p_4, we obtain

$$W_2^y = \frac{N}{m}\left[\sum_{n_0=0}^{\infty} H(n_0)^2 + 4\sum_{n_0=0}^{\infty}\sum_{n_a=1}^{\infty} H(n_0)H(n_0+n_a)\left(\frac{z_e}{dz_o}\right)^{n_a} + 2\sum_{n_0=0}^{\infty}\sum_{n_a=1}^{\infty}\sum_{n_b=1}^{\infty}[H(n_0+n_a)H(n_0+n_b)+H(n_0+n_a+n_b)H(n_0)] \left(\frac{z_e}{dz_o}\right)^{n_a+n_b}\right]\left(\frac{z_e}{dz_o}\right)^{2n_0}\frac{(n_0+1)!I(n_0)}{dz_o^{2-1/d}} + O(z^{-2}). \tag{6.60}$$

Expression for f_2

The contribution to the free energy f_2 from clusters with two configurations may now be computed. W_2^x [see Eq. (6.45)] contributes at order $z^{-1-1/d}$. It is straightforward to argue that configurations with three clusters will contribute at utmost order $z^{-1-2/d}$, hence we truncate f_2 at order $z^{-1-1/d}$. The leading term of W_2^y is $O(z^{-2+1/d})$, which for $d>2$ is much

smaller than W_2^x. Hence W_2^y does not contribute to f_2 for $d > 2$. When $m = 2$ and $d = 2$ we should include $O(z^{-2+1/d})$ term in W_2^y. This equals $3\ln(9/8)$, and coincides with the high-activity expansion for 2×2 hard squares [19]. Substituting for W_2^x from Eq. (6.45), we obtain

$$f_2 = \frac{-2}{mdz^{1+1/d}}\left[1 - \frac{d^{m-1}(d-m)}{(d-1)^m} + 6\delta_{d,2}\ln\frac{9}{8}\right] + O(z^{-1-2/d}). \tag{6.61}$$

6.3.4 High activity expansion for the free energy

The free energy up to order $z^{-1-1/d}$ is obtained by summing f_0 [Eq. (6.19)], f_1 [Eq. (6.33)], and f_2 [Eq. (6.61)]:

$$\begin{aligned} -f(z,z) = {} & \frac{\ln z}{dm} + \frac{z^{-1/d}}{dm} + \sum_{n=2}^{d+1} \frac{z^{-n/d}}{n!d^n m}\prod_{j=1}^{n-1}(jd-n) + \frac{z^{-1}}{md}(\kappa-1) \\ & + \frac{z^{-1-1/d}}{md^2}\left[1 + 2d - \frac{\kappa\left(2d^2 - 2dm + d + m - 2\right)}{d-1} + 24\delta_{d,2}\ln\frac{9}{8}\right] \\ & + O(z^{-1-2/d}). \end{aligned} \tag{6.62}$$

where

$$\kappa = \left(\frac{d}{d-1}\right)^{m-1}. \tag{6.63}$$

6.4 Densities and transition points

In this section we derive the high-activity expansion for the occupation densities of different rows. We truncate these expressions at $O(z^{-1-1/d})$ and then estimate the critical densities and activities for the nematic-columnar transition, and obtain their dependence on m and k.

Let ρ_o (ρ_e) denote the number of lattice sites occupied by rectangles whose heads are

in rows with label 1 (label different from 1). For rows with labels different from 1, the occupation densities will be equal. Hence,

$$\rho_o = -mdz_o \frac{d}{dz_o} f(z_o, z_e), \tag{6.64}$$

$$\rho_e = \frac{-mdz_e}{m-1} \frac{d}{dz_e} f(z_o, z_e), \tag{6.65}$$

where the factor md accounts for the volume of a rectangle, and the factor $m-1$ accounts for the $m-1$ labels that are different from 1. We, thus, obtain (after setting $z_o = z_e = z$)

$$\begin{aligned}\rho_o = 1 - \frac{z^{-1/d}}{d} - \sum_{n=2}^{d+1} \frac{z^{-n/d}}{d^n (n-1)!} \prod_{j=1}^{n-1} (jd - n) + \frac{1}{z}\left[1 - \frac{\kappa(d+m-2)}{d-1}\right] \\ - \frac{(2d+1)(d+1)}{d^2 z^{1+1/d}} - \frac{\kappa}{(d-1)^2 z^{1+1/d}}\Big[\frac{m-2}{d^2} - \frac{m^2-m+1}{d} \\ + 2m^2 - 5m + 6 + (2m-1)d - 2d^2 + (17\ln\frac{9}{8} + 4)\delta_{d,2}\Big] + O(z^{-1-2/d}),\end{aligned} \tag{6.66}$$

$$\rho_e = \kappa\left[\frac{1}{z(d-1)} + \frac{2md - 2d - m + 2 + (16\ln\frac{9}{8} + 8)\delta_{d,2}}{d(d-1)^2 z^{1+1/d}}\right] + O(z^{-1-2/d}), \tag{6.67}$$

where κ is as defined in Eq. (6.63).

In Fig. 6.10 we plot Eqs. (6.66) and (6.67), truncated at $O(z^{-1-1/d})$ for $m = 2$ and $d = 22$. With increasing z^{-1}, ρ_o decreases while ρ_e increases. The intersection point of these two curves gives an estimate of the transition point. In the example shown in Fig. 6.10, the estimates for the critical parameters are $z_c \approx 0.267$ and $\rho_c \approx 0.411$, where z_c and ρ_c are the critical activity and critical density respectively.

For large z, the expressions Eqs. (6.66) and (6.67) are a good approximation to the actual densities and reproduce the Monte Carlo results quite accurately. The comparison with the Monte Carlo results is in shown in the insets of Fig. 6.10 for both ρ_o and ρ_e, and in Table 6.1 for ρ. For $z \geq 25.0$, the expansion matches with the Monte Carlo results up to the third decimal place. This serves as an additional check for the correctness of the calculations.

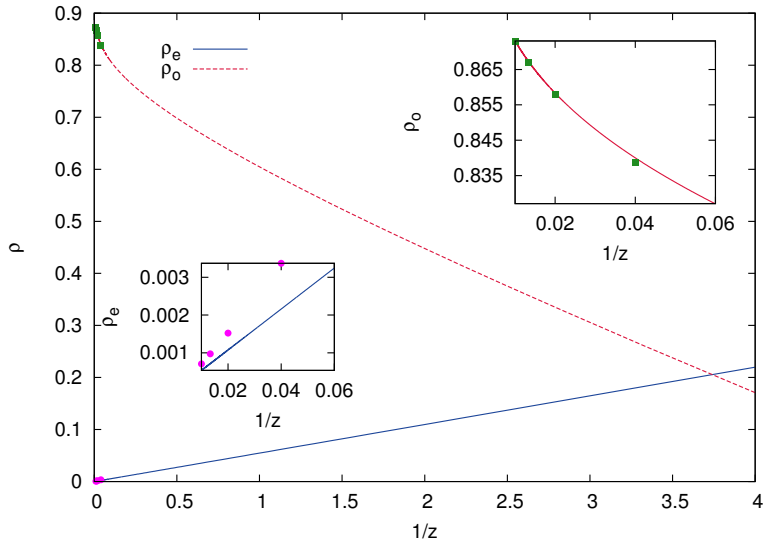

Figure 6.10: The high activity expansions Eqs. (6.66) and (6.67) for ρ_o and ρ_e truncated at order $z^{-1-1/d}$ for $m = 2$ and $d = 22$. The data points are from Monte Carlo simulations. The two curves intersect at $z_c \approx 0.267$ and $\rho_c = \rho_o + \rho_e \approx 0.411$. Right inset: Blow up of the large z region for ρ_o. Left inset: Blow up of the large z region for ρ_e.

Table 6.1: Comparison of the results for density ρ from the high-activity expansion ρ^{exp} [see Eqs. (6.66) and (6.67)] with results from Monte Carlo simulations ρ^{sim} for four different values of the activity z. The data are for a system of 2×22 rectangles.

z	ρ^{exp}	ρ^{sim}
25.0	0.8422	0.8420
50.0	0.8594	0.8593
75.0	0.8680	0.8680
100.0	0.8736	0.8736

By truncating the high-activity expansion, ρ_o is overestimated and ρ_e is underestimated. In addition, for $m > 3$, the nematic-columnar transition is first order in nature (ρ has a discontinuity), and z_c will be larger than the value of z for which $\rho_o = \rho_e$. Hence, the estimate for z_c that we obtain by setting $\rho_o = \rho_e$ in the truncated series is a lower bound to the actual z_c. For example, for 2×2 rectangles, z_c increases from 6.250 when the series are truncated at $O(z^{-1})$ to 14.859 when the series are truncated at $O(z^{-1-1/d})$ while the actual value is 97.5 [19], while for 2×22 rectangles the corresponding values are 0.253, 0.267, and 2.11 (see Fig. 6.2) respectively. We find that the increase in z_c, when terms of $O(z^{-1-1/d})$ are included, scales as k^{-2}, while the corresponding increase in ρ_c scales as k^{-1}.

We now study the dependence of the estimated z_c and ρ_c on m and d. Figure 6.11 shows the variation of z_c with k for different values of m. For large k, z_c decreases with k as a power law ck^{-1}, where $c \approx 2.78$ is independent of m. For small k, there is a crossover to a different behaviour that depends weakly on m. We could not collapse the data for different m onto a single curve by scaling k with a power of m. Hence, most likely the crossover scale increases logarithmically with m. To summarize,

$$z_c \approx \frac{2.78}{k}, \quad k \gg 1, \quad \forall m. \tag{6.68}$$

This behaviour is in qualitative agreement with the result from Monte Carlo simulation, which yields $z_c \approx 35.5k^{-1}$ (see Fig. 6.2).

The variation of the corresponding critical density $\rho_c(m, k)$ with k and m is shown in Fig. 6.12. For large k, ρ_c decreases linearly with k^{-1} for all m. This dependence is brought out more clearly by $d\rho_c/dk = \rho_c(k+1) - \rho_c(k)$ (see left inset of Fig. 6.12), which is independent of m and decreases as k^{-2} for large k. We may thus write

$$\rho_c(m, k) = \rho_c(m, \infty) + \frac{b_1}{k}, \quad k \gg 1, \tag{6.69}$$

where $\rho_c(m, \infty)$ is the m-dependent critical density for systems of rectangles of infinite

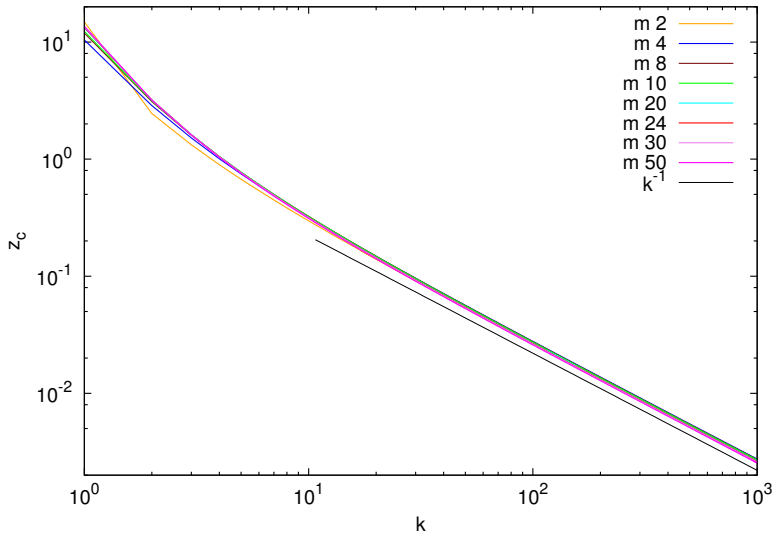

Figure 6.11: Variation of z_c with k for different m.

aspect ratio, and $b_1 \approx 0.367$ is independent of m. For the corresponding data from Monte Carlo simulation $b_1 \approx 0.226$ (see Fig. 6.2). We determine $\rho_c(m, \infty)$ by fitting the data to Eq. (6.69), and its dependence on m is shown in the right inset of Fig. 6.12. We find that the data is well-described by the form

$$\rho_c(m, \infty) \approx b_2 - \frac{b_3}{\ln(m + b_4)}, \; m \gg 1, \tag{6.70}$$

with $b_2 \approx 0.464$, $b_3 \approx 0.29$ and $b_4 \approx 13.0$.

Note that the k-dependence of $\rho_c(m, k)$ [see Eq. (6.69)] is in qualitative agreement with the results from Monte Carlo simulations for systems with $m = 2$ (see Fig. 6.2 and [21]) and those from Bethe approximation for large k [20]. Thus, though the estimates that we obtain are lower bounds (if the signs of the terms in the expansion do not oscillate) for the actual transition, we expect that the truncated expansions give the correct qualitative trends for the critical parameters.

We now study the large m behaviour of the critical density and critical activity of system of hard squares of size $m \times m$, i.e., $k = 1$. We find that z_c increases up to $m = 97$ and then decreases to a constant for large m, while $\rho_c(m, 1)$ decreases up to $m = 19$ and

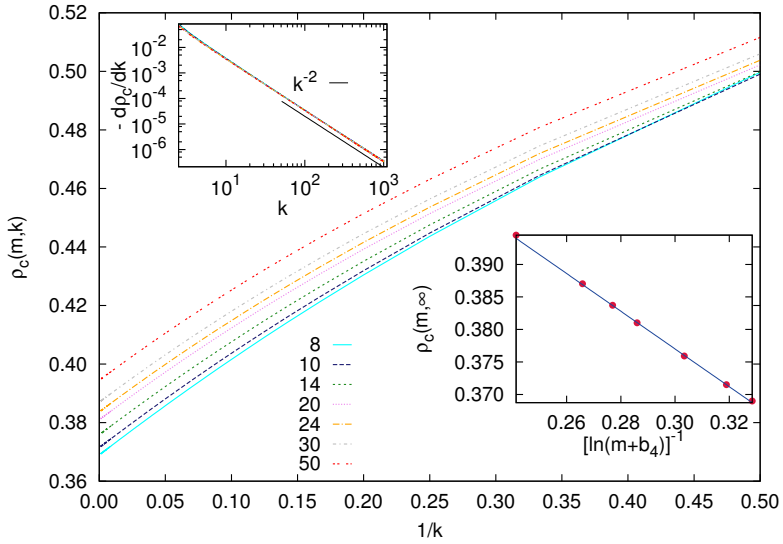

Figure 6.12: Variation of $\rho_c(m,k)$ with k for different m. Right inset: $\rho_c(m,\infty)$, the critical density for rectangles with infinite aspect ratio, is well-described by Eq. (6.70) $b_2 = 0.464$, $b_3 = 0.29$, and $b_4 = 13.0$ (fit shown by solid line). Left inset: The data for $d\rho_c/dk$ for different m collapse onto a single curve, independent of m.

then increases to a constant for large m. The asymptotic critical values are approached logarithmically as the data are best described by (see Fig. 6.13)

$$z_c(m,1) = b_5 + \frac{b_6}{\ln(m+b_7)}, \tag{6.71}$$

$$\rho_c(m,1) = b_8 - \frac{b_9}{\ln(m+b_{10})}, \tag{6.72}$$

with $b_5 = 12.085$, $b_6 = 9.54$, $b_7 = 228.56$, $b_8 = 0.669$, $b_9 = 0.44$, and $b_{10} = 121.24$.

6.5 Discussion

In this chapter, we derived the high-activity expansion for the free energy and density of the columnar phase of $m \times d$ rectangles in a model where the rectangles were restricted to be horizontal. The expansion is in inverse powers of $z^{-1/d}$, where z is the activity. We explicitly computed the first $d+2$ terms in this expansion. As in the case for hard squares ($m = 2, d = 2$) [19], the expansion is not in terms of single defects, but in terms of clusters

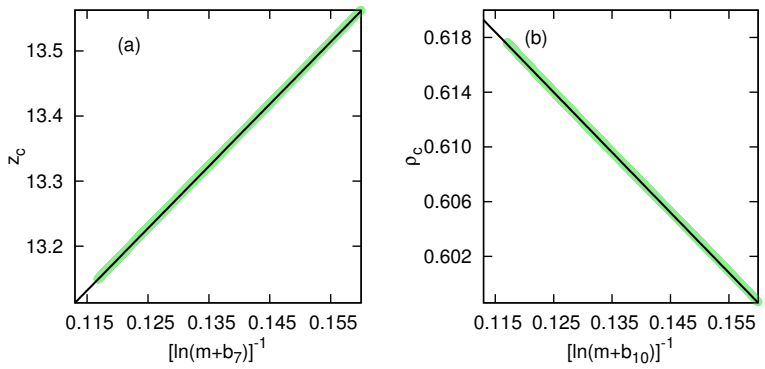

Figure 6.13: Critical (a) activity z_c, and (b) density ρ_c, for a system of $m \times m$ hard squares. The straight lines correspond to (a) Eq. (6.71) with $b_5 = 12.085$, $b_6 = 9.54$ and $b_7 = 228.56$, and (b) Eq. (6.72) with $b_8 = 0.669$, $b_9 = 0.44$ and $b_{10} = 121.24$.

of defects.

From the high-activity expansions for the densities of rectangles with heads on rows of different labels, truncated at $O(z^{-1-1/d})$, we estimate the transition points z_c and ρ_c. We find that $z_c \approx ck^{-1}$, $\rho_c(m,k) \approx \rho_c(m,\infty) + b_1 k^{-1}$ for $k \gg 1$, where $c > 0$, and $b_1 > 0$, are m-independent constants, and $\rho_c(m,\infty)$ tends to a constant for large m with deviations decreasing as some inverse power of $\ln m$. For hard squares with $d = m$, or equivalently $k = 1$, we obtain that the critical density increases logarithmically to a constant when $m \gg 1$.

For $m = 2$, from the truncated series, we estimate $\rho_c(2,\infty) \approx 0.38$. This should be compared with the estimates from Monte Carlo simulations of $\rho_c(2,\infty) \approx 0.73$ [21], which are much larger than the series expansion results. In the next chapter, we will show that $\rho_c(\infty) = 3/4$ for $m = 2$ by determining the interfacial tension between two ordered phases [193].

The high-density series being truncated at $O(z^{-1-1/d})$, the estimates for the critical parameters are lower bounds for the actual values. However, we note that the dependence of $\rho_c(m,k)$ and $z_c(m,k)$ on k matches qualitatively with the results obtained from Monte Carlo simulations for $m = 2$ (see Fig. 6.2 and [21]) and Bethe approximation [20] for large k. This leads us to conjecture that the trends for the critical parameters obtained from the

truncated series expansion are qualitatively correct. If that is true, the limit $m \to \infty$ keeping the aspect ratio k fixed, corresponding to the limit of oriented rectangles in the continuum may be studied. When $m \to \infty$, our results show that z_c decreases to a finite constant for all k. If this feature carries over to the actual system, then, it would imply that ρ_c for large m is less than one, implying that the nematic-columnar transition exists when $m \to \infty$. Likewise, there should be a isotropic-columnar transition for hard squares ($k = 1$) in the continuum at a finite density. These conjectures should be verifiable using Monte Carlo for systems in the continuum.

The high density expansion derived in this chapter was for a model where all the rectangles were horizontal. This is a special case ($z_v = 0$) of the more general model where rectangles of horizontal and vertical orientations occur with activity z_h and z_v respectively. We argued, from Monte Carlo simulations, that setting $z_v = 0$ does not affect the nematic-columnar transition for large aspect ratio k. However, the two models may differ for small k. For $k < 7$, the nematic phase does not exist when $z_v = z_h$ [20]. However, when $z_v = 0$, we have verified numerically that the nematic-columnar transition exists even for a system of 2×3 rectangles. For 2×3 rectangles, when $z_v = z_h$, there are no density-driven phase transitions. Thus, in the two-dimensional z_v–z_h phase diagram, the phase boundary that originates at $z_v = 0$ must terminate on the line $z_h > z_v$, $z_v, z_h \to \infty$. This leads to the interesting possibility that in the fully packed limit, as the ratio z_h/z_v is increased, the system should undergo a nematic-columnar transition. This conjecture should be verifiable for systems like 2×3 rectangles using Monte Carlo algorithms of the kind recently implemented in Ref. [92] where the fully packed limit of mixtures of dimers and squares could be efficiently simulated and shown to undergo a Berezinskii-Kosterlitz-Thouless transition.

The high-activity expansion presented in the chapter may be generalized to systems of polydispersed rods on lattices [169, 194] with same m and different d. Suppose the rod-lengths are denoted by d_i. The calculation of f_0 requires the knowledge of only λ [see

Eq. (6.16)]. The recursion relations Eqs. (6.13), (6.14) and (6.15) obeyed by the one-dimensional partition functions will now be modified to

$$\Omega_p(\{z_i\}, L) = \sum_i d_i z_i \Omega_o(\{z_i\}, L - d_i) + \Omega_o(\{z_i\}, L - 1), \; L \geq \max[\{d_i\}], \tag{6.73}$$

$$\Omega_o(\{z_i\}, \ell) = \sum_i z_i \Omega_o(\{z_i\}, \ell - d_i)\theta(\ell - d_i) + \Omega_o(\{z_i\}, \ell - 1),$$

$$\ell \geq \min[\{d_i\}], \tag{6.74}$$

$$\Omega_o(\{z_i\}, \ell) = 1, \; 0 \leq \ell < \min[\{d_i\}], \tag{6.75}$$

where z_i is the activity of a rod of length d_i, and $\theta(x)$ is the usual theta function. The corresponding polynomial equation (6.16) is then modified to

$$1 - \lambda^{-1} - \sum_i z_i \lambda^{-d_i} = 0, \tag{6.76}$$

making it possible to calculate the high-activity expansion for f_0. The calculation of the contribution from configurations with a single cluster of defects is also generalizable to the case of polydispersed rods. A defect cluster now consists of rods of different lengths. The associated weight now depends not just on the length of the cluster but also on the detailed structure of the cluster. Though more complicated, it is still possible to write an exact expression for the contribution from single defect-clusters.

Another possible extension of the derivation presented in this chapter is to find higher order correction terms. For example, suppose we consider the $O(z^{-1-2/d})$ term. If $d \geq 4$, then there is no contribution at this order from W_2^y that accounts for defect clusters with overlap along the y-direction. The contribution to $O(z^{-1-2/d})$ term from configurations with two or more defect-clusters is only from W^x that accounts for defect-clusters with overlap in the x-direction. This includes the $\Delta = 2$ term in Eq. (6.34), and contribution from configurations with three defect-clusters, where each cluster is misaligned from the

bottom cluster by ±1. The corresponding term for three defect-clusters is

$$\frac{4N}{m}\sum_{\{n_i\}} H\left[\sum_i n_i\right]\left[\frac{\Omega_o(z_o, L-d)z_e}{\Omega_p(z_o, L)}\right]^{\sum_i n_i - 1} z_e\left[\frac{\Omega_o(z_o, L-d-1)}{\Omega_p(z_o, L)}\right]^2, \tag{6.77}$$

where n_i is the number of rectangles in defect-cluster i. It is straightforward to check that the above expression contributes at $O(z^{-1-2/d})$. Similarly, one can calculate the higher order terms up to $O(z^{2-2/d})$ by considering only W^x.

Finally, it would be important to find an upper bound for the critical parameters z_c and ρ_c. This would amount to showing that the high-activity expansion derived in this chapter has a finite radius of convergence. However, this may not be easy as up till now, there exists no rigorous proof for the existence of a columnar phase in any lattice model.

Chapter 7

Stability of columnar order in assemblies of hard rectangles or squares

7.1 Introduction

For large d, the estimates from Monte Carlo simulations for the the critical parameters of the nematic-columnar transition are $z_c(d) \approx 71.0d^{-1} + O(d^{-2})$ and $\rho_c(d) \approx 0.73 + 0.46d^{-1} + O(d^{-2})$ [21]. As in the case of hard squares, standard approximation techniques give poor theoretical estimates. In the previous chapter we obtain estimates from the singular high-density expansion in powers of $z^{-1/d}$ as $z_c(d) = 5.56d^{-1} + O(d^{-2})$ and $\rho_c(d) = 0.357 + 0.73d^{-1} + O(d^{-2})$ whereas a Bethe approximation gives $\rho_c(d) = 0.59 + 0.29d^{-1} + O(d^{-2})$ [20]. However, the estimates were still off. Details of the earlier findings are elaborated in Sec. 1.3.2 and the estimates are compared in Tables 1.1 and 1.3.

We study the transition between the nematic and columnar phases of $2 \times d$ rectangles on a square lattice, under the simplifying restriction that all rectangles are fully aligned (all horizontal). For large d, for most densities in the nematic/columnar range, this approximation is very good (for $d = 18$ and $\rho = 0.75$, the deviation from perfect orientational

order is $\approx 0.15\%$). Whenever a nematic phase exists (only when $d \geq 14$), the critical threshold for the nematic-columnar transition with all rectangles oriented in one direction was shown numerically to not change much if they are allowed to have arbitrary orientations [174]. Also, it is not an approximation when $d = 2$, as there is no distinction between horizontal and vertical squares. However, restricting to only horizontal rectangles has the important consequence that we obtain a phase transition for all $d \geq 2$, while if we allow rectangles of both orientations, then systems with odd d and $d \leq 9$ have no phase transitions [182].

We estimate the interfacial tension between two phases with different columnar order, and setting this to zero, we obtain a condition for the limit of stability of the columnar ordered phase. We have done our calculation in two different approximations. In the first, we work out the high-density expansion for the interfacial tension as a perturbation series in the defect density, and estimate the critical point by truncating this expansion at first order. The formal power series in powers of defect density is a singular perturbation series in the activity z. At the zeroth order in defect density, it is straightforward to determine the partition function per site in the bulk, and the interface is a partially directed self-avoiding walk (PDSAW). Summing over the different configurations of the walk gives us the zeroth order estimates of $z_c(d)$ and $\rho_c(d)$. We then calculate the first order correction to this result due to the presence of defects in the bulk phases. In the second method, we ignore defects in the bulk, but take into account a subset of configurations of the interface with overhangs to improve the estimate of the interfacial tension. Both these approximations give values [see Eqs. (7.74), (7.75), (7.89) and (7.90)] that are quite close to the Monte Carlo estimates, and are a significant improvement over earlier methods. The content of this chapter is published in Ref. [193].

7.2 Model and methodology

Consider hard rectangles of size $2 \times d$ ($d \geq 2$), whose long edges are aligned along the horizontal x-direction, on a square lattice of size $N \times M$, interacting through only excluded volume interactions (two rectangles may not overlap). An activity z is associated with each rectangle. The system is disordered at low densities and shows columnar order at high densities [174]. We call the phase odd (even) in which the majority of heads (bottom left corner) of the rectangles are in odd (even) rows.

The critical density for the nematic-columnar transition is finite because, for large d, we can rescale the x-axis by a factor d, and the problem becomes equivalent to a model of 1×1 oriented hard squares in a space where x is continuous, but y is discrete. Two squares cannot overlap or have a common boundary. In this continuum problem, the space between two lines $y = n$ and $y = n + 1$ is like a continuum hard-core gas [195, 196], and the transition would be expected to occur at a finite density. The fractional area covered is unaffected by rescaling of the x-axis. The activity z_{cont} in this continuum model is related to the lattice activity z by $z_{cont} = dz$.

We estimate the critical activity $z_c(d)$ and the critical density $\rho_c(d)$ at the nematic-columnar transition by calculating within an approximation scheme, the interfacial tension $\sigma(z)$ between the even and odd phases. Estimating interfacial tension has been useful in determining the phase diagrams of different lattice models. Examples include Ising [197, 198], and Potts models [199].

To compute $\sigma(z)$, we impose an interface by fixing the rectangles at the left (right) boundary to be even (odd). A typical configuration seen in a simulation of 2×4 rectangles is shown in Fig 7.1. We note that there may be some empty space between the odd and even rectangles. To define an unique position of the interface for any allowed configuration of rectangles, we adopt the convention that the boundary between the left (even) and right (odd) phase is placed as far left as possible. With this convention, there is a well-

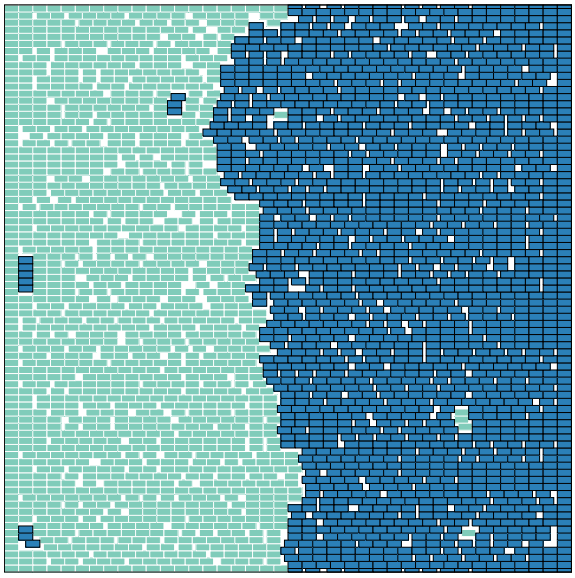

Figure 7.1: Snapshot of a typical configuration of 2×4 rectangles where the left (right) phase is constrained to be even (odd) by fixing the rectangles at the boundary. Even (odd) rectangles are shown in teal (blue). The system size is 160×160.

defined interface with the bulk phases having very few defects (rectangles of the wrong type which when removed results in a fully ordered columnar phase).

Let $\Omega_{eo}(z, z_D|I)$ be the partition function with a given interface I, where z_D is the activity of a defect, and e and o refer to even and odd respectively. Then, $\Omega_{eo}(z, z_D)$, the partition function with an interface present, is the sum of $\Omega_{eo}(z, z_D|I)$ over different interfaces I:

$$\Omega_{eo}(z, z_D) = \sum_I \Omega_{eo}(z, z_D|I). \tag{7.1}$$

Let $\Omega_{ee}(z, z_D)$ be the partition function when all rectangles at the boundaries are fixed to be even (no interface). Then,

$$\sigma(z) = \lim_{M\to\infty} \frac{-1}{M} \ln\left[\frac{\Omega_{eo}(z, z_D)}{\Omega_{ee}(z, z_D)}\right], \tag{7.2}$$

and we define the effective free energy $H_{\text{eff}}(I)$ of any interface I to be

$$H_{\text{eff}}(I) = -\ln\left[\frac{\Omega_{eo}(z, z_D|I)}{\Omega_{ee}(z, z_D)}\right]. \tag{7.3}$$

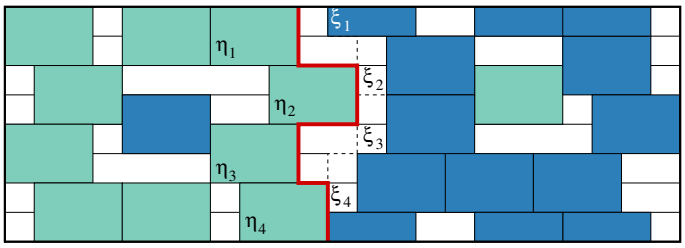

Figure 7.2: A schematic diagram of the interface (thick red line) between two phases having a defect each. Even (odd) rectangles are shown in teal (blue). η_i is the x-coordinate of the head of the rightmost non-defect rectangle in row i, and $\xi_i = \max(\eta_i, \eta_{i-1}) + d$ is the minimum allowed x-coordinate for heads of odd rectangle on the $(2i-1)$th row.

In the simplest approximation, we ignore overhangs such that the interface is a path from top to bottom with no upward steps allowed. Then, the interface I is uniquely defined by $\{\eta\}$, where η_i is the head of the right most rectangle of the even phase [see Fig 7.2]. Since the interactions are hard core, given an interface I, the left and right phases may be occupied with rectangles independent of each other, such that

$$\Omega_{eo}(z, z_D|I) = \Omega_L(z, z_D|I)\Omega_R(z, z_D|I), \tag{7.4}$$

where L (R) refers to left (right) phase.

Each of the partition functions $\Omega_{ee}(z, z_D)$, $\Omega_{eo}(z, z_D|I)$, $\Omega_L(z, z_D|I)$ and $\Omega_R(z, z_D|I)$ may be expanded as a perturbation series in z_D,

$$\Omega_{ee}(z, z_D) = \Omega^{(0)}_{ee}(z) + z_D\Omega^{(1)}_{ee}(z) + O(z_D^2), \tag{7.5}$$

$$\Omega_{eo}(z, z_D|I) = \Omega^{(0)}_{eo}(z|I) + z_D\Omega^{(1)}_{eo}(z|I) + O(z_D^2), \tag{7.6}$$

$$\Omega_{L}(z, z_D|I) = \Omega^{(0)}_{L}(z|I) + z_D\Omega^{(1)}_{L}(z|I) + O(z_D^2), \tag{7.7}$$

$$\Omega_{R}(z, z_D|I) = \Omega^{(0)}_{R}(z|I) + z_D\Omega^{(1)}_{R}(z|I) + O(z_D^2), \tag{7.8}$$

where the superscript (n) refers to the presence of n defects. Substituting Eqs. (7.6),(7.7)

and (7.8) and in Eq. (7.4), we obtain

$$\Omega^{(0)}_{eo}(z|I) = \Omega^{(0)}_{L}(z|I)\Omega^{(0)}_{R}(z|I) \tag{7.9}$$

$$\Omega^{(1)}_{eo}(z|I) = \Omega^{(0)}_{L}(z|I)\Omega^{(1)}_{R}(z|I) + \Omega^{(0)}_{R}(z|I)\Omega^{(1)}_{L}(z|I) \tag{7.10}$$

The effective free energy $H_{\rm eff}(I)$ and interfacial tension $\sigma(z)$ may also be expanded as a perturbation series in z_D as

$$H_{\rm eff}(I) = H^{(0)}_{\rm eff}(I) + z_D H^{(1)}_{\rm eff}(I) + O(z_D^2), \tag{7.11}$$

$$\sigma = \sigma^{(0)} + z_D\sigma^{(1)} + O(z_D^2). \tag{7.12}$$

Using perturbation expansions of $\Omega_{ee}(z, z_D)$ and $\Omega_{eo}(z, z_D|I)$ in Eq. (7.3), we obtain n-defect contributions to $H_{\rm eff}(I)$ as

$$H^{(0)}_{\rm eff}(I) = -\ln\frac{\Omega^{(0)}_{eo}(z|I)}{\Omega^{(0)}_{ee}(z)} \tag{7.13}$$

$$H^{(1)}_{\rm eff}(I) = -\frac{\Omega^{(1)}_{eo}(z|I)}{\Omega^{(0)}_{eo}(z|I)} + \frac{\Omega^{(1)}_{ee}(z)}{\Omega^{(0)}_{ee}(z)} \tag{7.14}$$

which can be rewritten as (see Eqs. (7.9) and (7.10)),

$$H^{(0)}_{\rm eff}(I) = -\ln\frac{\Omega^{(0)}_{L}(z|I)\Omega^{(0)}_{R}(z|I)}{\Omega^{(0)}_{ee}(z)}, \tag{7.15}$$

$$H^{(1)}_{\rm eff}(I) = \frac{\Omega^{(1)}_{ee}(z)}{\Omega^{(0)}_{ee}(z)} - \frac{\Omega^{(1)}_{L}(z|I)}{\Omega^{(0)}_{L}(z|I)} - \frac{\Omega^{(1)}_{R}(z|I)}{\Omega^{(0)}_{R}(z|I)}. \tag{7.16}$$

We can rewrite interfacial tension (Eq. (7.2)) in terms of $H_{\rm eff}(I)$,

$$\sigma(z) = \lim_{M\to\infty}\frac{-1}{M}\ln\sum_{I} e^{-H_{\rm eff}(I)}. \tag{7.17}$$

Substituting Eq. (7.11) in the above equation the perturbation expansion of interfacial

tension can be expressed in terms of zero and one-defect terms of expansion of $H_{\rm eff}$,

$$\sigma(z) = \lim_{M\to\infty}\Big[\frac{-1}{M}\ln\sum_I e^{-H^{(0)}_{\rm eff}(I)} + \frac{z_D}{M}\frac{\sum_I H^{(1)}_{\rm eff}(I)e^{-H^{(0)}_{\rm eff}(I)}}{\sum_I e^{-H^{(0)}_{\rm eff}(I)}} + O(z_D^2)\Big]. \tag{7.18}$$

Thus comparing Eq.(7.12) and Eq. (7.18), we obtain the zero defect and one defect contributions to $\sigma(z)$ in terms of $H_{\rm eff}(I)$

$$\sigma^{(0)}(z) = \lim_{M\to\infty}\frac{-1}{M}\ln\sum_I e^{-H^{(0)}_{\rm eff}(I)}, \tag{7.19}$$

$$\sigma^{(1)}(z) = \lim_{M\to\infty}\frac{1}{M}\frac{\sum_I H^{(1)}_{\rm eff}(I)e^{-H^{(0)}_{\rm eff}(I)}}{\sum_I e^{-H^{(0)}_{\rm eff}(I)}}. \tag{7.20}$$

7.3 Zero defect calculation

7.3.1 Calculation of $\sigma^{(0)}(z)$

The calculation of $\sigma^{(0)}(z)$ is quite straightforward. In the absence of defects, each phase consists of only rectangles of one kind, either even or odd. This implies that the configuration of rectangles in a row is independent of those in the other rows. Thus, the partition functions $\Omega^{(0)}_{ee}(z)$, $\Omega^{(0)}_{L}(z|I)$ and $\Omega^{(0)}_{R}(z|I)$ become products of one-dimensional partition functions, and we obtain

$$\Omega^{(0)}_{ee}(z) = [\omega_0(N)]^{M/2}, \tag{7.21}$$

$$\Omega^{(0)}_{L}(z|I) = \prod_{i=1}^{M/2}[z\omega_0(\eta_i)], \tag{7.22}$$

$$\Omega^{(0)}_{R}(z|I) = \prod_{i=1}^{M/2}\omega_0(N-\xi_i), \tag{7.23}$$

where the interface is specified by $\{\eta\}$, $\xi_i = \max(\eta_i, \eta_{i-1}) + d$ [see Fig. 7.2], and $\omega_0(N)$ is the partition function of a system of hard rods of length d on a one dimensional open

chain of length N. The factor z in Eq. (7.22) accounts for the constraint that the right most site of each even row in the even phase should be occupied. The zero defect contribution to the effective (free) energy of the interface $\{\eta\}$ is then [see Eq. (7.15)]

$$H_{\text{eff}}^{(0)} = -\sum_{i=1}^{M/2} \ln\left[\frac{z\omega_0(\eta_i)\omega_0(N-\xi_i)}{\omega_0(N)}\right], \tag{7.24}$$

It is easy to see that ω_0 obeys the recursion relation

$$\omega_0(\ell) = z\omega_0(\ell - d) + \omega_0(\ell - 1), \tag{7.25}$$

for $\ell = 1, 2, \ldots$ with $\omega_0(0) = 1$, and $\omega_0(\ell) = 0$ for $\ell < 0$. For large N, $\omega_0(N) = a\lambda^N[1 + O(\exp(-N))]$, where λ is the largest root of the equation

$$\lambda^d - \lambda^{d-1} = z. \tag{7.26}$$

This equation has d roots. Let them be denoted by λ_i, $i = 1, 2, \ldots, d$ where λ_1, the largest root, will be denoted by λ. Then for any ℓ, the one-dimensional partition function can thus be written as

$$\omega_0(\ell) = \sum_{i=1}^{d} a_i \lambda_i^{\ell}. \tag{7.27}$$

For large ℓ, we can approximate $\omega_0(\ell) \approx a\lambda^{\ell}$, where a is a_1 of Eq. (7.27).

The effective (free) energy of the interface $\{\eta\}$ is then [see Eq. (7.24)]

$$H_{\text{eff}}^{(0)} = \frac{-M}{2} \ln[a(1 - \lambda^{-1})] + \frac{1}{2} \ln \lambda \sum_i |\eta_{i+1} - \eta_i|. \tag{7.28}$$

We calculate a from the density of occupied sites. Suppose $\rho(d)$ is the density of the rectangles on the one-dimensional chain of length ℓ. Then $\rho(d)$ is given by

$$\rho(d) = \frac{d}{\ell} z \frac{d}{dz} \ln \omega_o(\ell). \tag{7.29}$$

On substitution of $\omega_0(\ell) \approx a\lambda^\ell$ we obtain

$$\rho(d) = \frac{d(\lambda-1)}{d(\lambda-1)+1}. \tag{7.30}$$

Consider a site m in the bulk of the chain. The probability that it is empty is $[\omega_0(m-1)\omega_0(1)\omega_0(\ell-m)]/\omega_0(\ell)$. It is straightforward to realize that

$$\frac{\omega_0(m-1)\omega_0(\ell-m)}{\omega_0(\ell)} = 1-\rho(d) \tag{7.31}$$

Substituting $\omega_0(\ell) \approx a\lambda^\ell$ on the left hand side of Eq. (7.31), we obtain,

$$1-\rho(d) = \frac{a}{\lambda}. \tag{7.32}$$

Substituting expression of $\rho(d)$ from Eq. (7.30) in Eq. (7.32), a is given by

$$a = \frac{\lambda}{d(\lambda-1)+1}. \tag{7.33}$$

Thus substituing expression of a in Eq.(7.28), we obtain the interfacial tension when there are no defects [see Eq. (7.19)] to be

$$\sigma^{(0)}(z) = -\frac{1}{2}\ln\left[\frac{(\sqrt{\lambda}+1)^2}{d(\lambda-1)+1}\right], \tag{7.34}$$

where λ is related to z by Eq. (7.26).

7.3.2 Calculation of PDSAW

We can also obtain the criticality condition by considering the interface $\{\eta\}$ as a PDSAW, a self avoiding walk in which steps in the upward direction are disallowed. We denote weight for vertical downward step as $\mathbb{D}$, upward step as $\mathbb{U}$, left step as $\mathbb{L}$ and right step as

$\mathbb{R}$, whereas, the steps will be denoted by D, U, L and R respectively. A PDSAW consists of an arbitrary concatenation of substrings D, DR, DR^2,..., DL, DL^2,... etc. Hence the PDSAW has a formal generating function

$$\wp = \frac{1}{1 - D - DR^* - DL^*}, \tag{7.35}$$

where

$$R^* = R + R^2 + R^3 + \ldots = \frac{R}{1 - R}. \tag{7.36}$$

and a similar equation for L^*. Correspondingly, the equation for the evaluation of this generating function is

$$G = [1 - \mathbb{D} - \mathbb{D}\mathbb{R}^* - \mathbb{D}\mathbb{L}^*]^{-1}, \tag{7.37}$$

where $\mathbb{R}^*$ and $\mathbb{L}^*$ are defined as in Eq. (7.36). From Eq. (7.28), we can identify the weights of steps in left, right and down directions to be

$$\mathbb{D} = a(1 - \lambda^{-1}), \tag{7.38}$$

$$\mathbb{R} = \mathbb{L} = \lambda^{-1/2}. \tag{7.39}$$

The phase transition occurs when the interfacial tension (see Eq. (7.34)) is zero or equivalently when the generating function G in Eq. (7.37) diverges. Setting $\sigma^{(0)}(z) = 0$ and $\mathbb{D}(1 + \mathbb{R}^* + \mathbb{L}^*) = 1$, we obtain the criticality condition to be,

$$\frac{(\lambda_c^* + 1)^2}{d(\lambda_c^* - 1) + 1} = 1. \tag{7.40}$$

Simplifying Eq. (7.40) the estimates of the critical parameters $\lambda_c^*(d)$ and $\rho_c^*(d)$ (see Eq. (7.30))

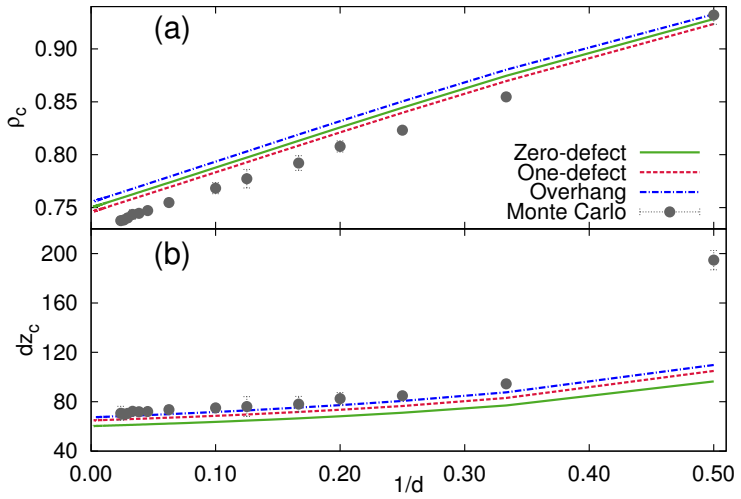

Figure 7.3: The results obtained for (a) critical density ρ_c and (b) critical activity z_c for the disordered-columnar transition with zero defect (green line), one defect (red line) and overhangs (blue line) are compared with the results from Monte Carlo simulations (data points). The Monte Carlo data for $d > 16$ is from Ref. [174], the data for $d \leq 16$ has been generated using the algorithm introduced in Refs. [90, 162], and the data for $d = 2$ is from Refs. [9, 12, 13].

are

$$\sqrt{\lambda_c^*(d)} = \frac{1 + \sqrt{1 - d + d^2}}{d - 1}, \tag{7.41}$$

$$\rho_c^*(d) = \frac{d(1 + d + 2\sqrt{1 - d + d^2})}{(d + \sqrt{1 - d + d^2})^2}, \tag{7.42}$$

and $z_c^*(d) = \lambda_c^*(d)^d - \lambda_c^*(d)^{d-1}$.

For hard-squares ($d = 2$), $\lambda_c^*(2) = (\sqrt{3}+1)^2$, $z_c^*(2) = (4+2\sqrt{3})(3+2\sqrt{3}) \approx 48.25$, $\rho_c^*(2) = (6 + 4\sqrt{3})(7 - 4\sqrt{3}) \approx 0.928$. These should be compared with numerically obtained $z_c = 97.5$ and $\rho_c = 0.932$ [9, 12, 13]. For large d limit, the solution is $\lambda_c^* = 1+3d^{-1}+O(d^{-2})$, $z_c = 60.26d^{-1} + O(d^{-2})$, and $\rho_c^* = 0.75 + 0.375d^{-1} + O(d^{-2})$. These should be compared with the numerically obtained values $z_c \approx 71.0/d$ and $\rho_c \approx 0.73 + 0.46/d$ [21, 174]. For intermediate values of d, the analytical expression is compared with the Monte Carlo results in Fig. 7.3. We note that the results of calculation with no defects are already significantly better than earlier estimates.

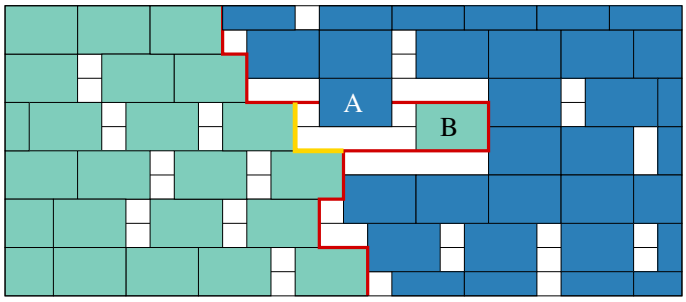

Figure 7.4: A configuration with a single defect where the interface may be drawn (red or yellow) so that the defect is an odd rectangle (A) in the even phase, or an even rectangle (B) in the odd phase.

7.4 One defect calculation

Consider now the corrections to the interfacial tension to the first order in z_D. For this, we need to compute $\Omega^{(1)}_{ee}$, $\Omega^{(1)}_{L}(z|I)$, and $\Omega^{(1)}_{R}(z|I)$, the partition functions when a single defect is present. There are configurations which may be considered as single odd defect in the even phase, or equally as a single even defect in the odd phase by repositioning the interface [see Fig. 7.4]. To avoid over-counting, we impose the constraints that a defect in the even phase should at least have two even rectangles to its right [see Fig. 7.5(b)-(c)] and a defect in the odd phase should have at least one odd rectangle to its left [see Fig. 7.5(d)-(e)]. Else, we redefine the interface locally.

In Fig. 7.5 and 7.6 examples of a single defect are shown for different cases. The defect is placed with head at x on a row which is in between the rows i and $i+1$. A defect rectangle affects the occupation of utmost the two rows adjacent to it, by splitting the row(s) into two intervals that may be occupied independent of each other. However, unlike the zero defect case, the intervals may be small instead of being extensive in N, and therefore it is necessary to know $\omega_0(\ell)$ for all ℓ and not just for large ℓ.

In Fig. 7.5(a) a defect is placed in a system without interface The defect splits the two rows i and $i+1$ into two open chains of length x and $N-x-d$. Head of the defect can be placed anywhere from 0 to $N-d$. Also the defect can be placed on any of the $M/2$ even

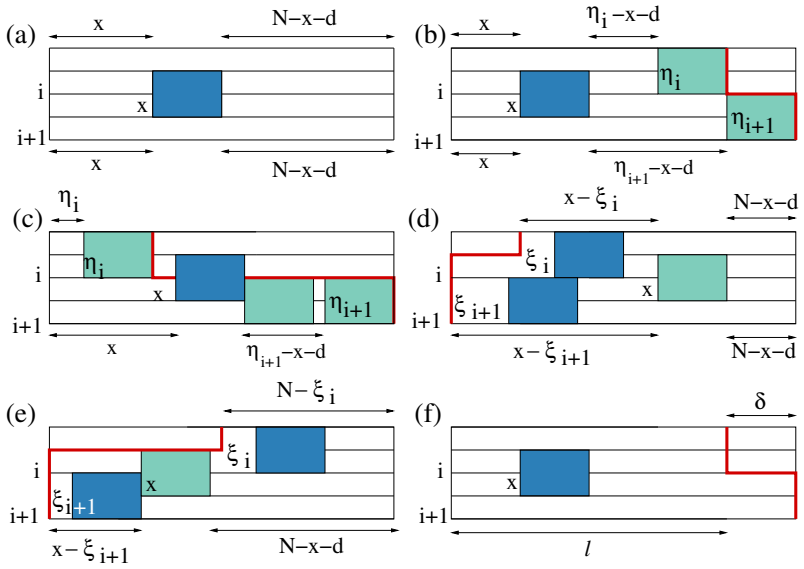

Figure 7.5: Examples of single defects for (a) $\Omega^{(1)}_{ee}$, (b)-(c) $\Omega^{(1)}_{eo,L}$ and (d)-(e) $\Omega^{(1)}_{eo,R}$. (f) A generalized two-row system with a single defect in the bulk. The red lines denote the position of the interface.

rows. Thus, we obtain

$$\frac{\Omega^{(1)}_{ee}}{\Omega^{(0)}_{ee}} = \frac{M}{2}\sum_{x=0}^{N-d}\left[\frac{\omega_0(x)\omega_0(N-x-d)}{\omega_0(N)}\right]^2. \tag{7.43}$$

We now compute partition function of the left phase with one defect. If the defect is in the bulk (see Fig. 7.5(b)), it splits i-th row into intervals x and $\eta_i - x - d$ and $i+1$-th row into x and $\eta_{i+1} - x - d$. Since the defect is in the bulk, x can vary from 0 to $\min(\eta_i, \eta_{i+1}) - d$. The defect however can be placed on the right of rightmost even rectangle on any row such that the other nearest even row has atleast two even rectangles to the right of the defect. In that case, it affects only one row. In Fig. 7.5(c) the defect thus splits $i+1$-th row into x and $\max(\eta_i, \eta_{i+1}) - x - d$ with no effect on i-th row. Since we have constraint of two even rectangles to be present on the right of the defect, we restrict

$$max(\eta_i, \eta_{i+1}) - min(\eta_i, \eta_{i+1}) \geq 3d. \tag{7.44}$$

This restriction is equivalent to $|\eta_{i+1} - \eta_i| \geq 3d$. Thus adding the two cases, we obtain,

$$\frac{\Omega^{(1)}_{eo,L}}{\Omega^{(0)}_{eo,L}} = \sum_{i=1}^{M/2} \Bigg[\sum_{x=0}^{x_L} \frac{\omega_0^2(x)\omega_0(\eta_i - x - d)\omega_0(\eta_{i+1} - x - d)}{\omega_0(\eta_i)\omega_0(\eta_{i+1})} + \sum_{x=x_L+2d}^{x'_L-2d} \frac{\omega_0(x)[\omega_0(x'_L - x - d) - 1]}{\omega_0(x'_L)} \Theta(|\Delta\eta_i| - 3d) \Bigg], \tag{7.45}$$

where $|\Delta\eta_i| = |\eta_{i+1} - \eta_i|$, $x_L = \min(\eta_i, \eta_{i+1}) - d$, $x'_L = \max(\eta_i, \eta_{i+1})$ and $\Theta(x)$ is a step function

$$\Theta(x) = \begin{cases} 1, & \text{if } x \geq 0, \\ 0, & \text{otherwise,} \end{cases} \tag{7.46}$$

and we have dropped the dependence on z, I for notational simplicity. We subtract out the null case from $\omega_0(x'_L - x - d)$ to exclude the possibility of absence of an even rectangle in between the defect and the rightmost even rectangle on $i + 1$-th row. The first and second terms of Eq. (7.45) are contributions from Fig. 7.5(b) and (c) respectively.

Consider now the defect to be in the bulk of the right phase (see Fig. 7.5(d)). The defect splits i-th row into $x - \xi_i$ and $N - x - d$ and $i + 1$-th row into $x - \xi_{i+1}$ and $N - x - d$ intervals. To incorporate the constraint of the presence of one odd rectangle to the left of the defect we subtract out the null case. Since we place the defect in the bulk, x can vary from $\max(\xi_i, \xi_{i+1})$ to $N - d$. Thus we obtain in the bulk,

$$\left.\frac{\Omega^{(1)}_{eo,R}}{\Omega^{(0)}_{eo,R}}\right|_{bulk} = \sum_{i=1}^{M/2} \sum_{x=x_R-d}^{N-d} \frac{\omega_0^2(N - x - d)[\omega_0(x - \xi_i)\omega_0(x - \xi_{i+1}) - 1]}{\omega_0(N - \xi_i)\omega_0(N - \xi_{i+1})}, \tag{7.47}$$

where $x_R = \max(\xi_i, \xi_{i+1}) + d$.

If the defect is on the left of one of the leftmost odd rectangles on any row it affects only the other nearest odd row. In Fig. 7.5(e) thus the defect affects only the $i + 1$-th row. We divide the scenario into two cases,

(1) $\min(\xi_i, \xi_{i+1}) + d \leq x \leq \max(\xi_i, \xi_{i+1}) - d$

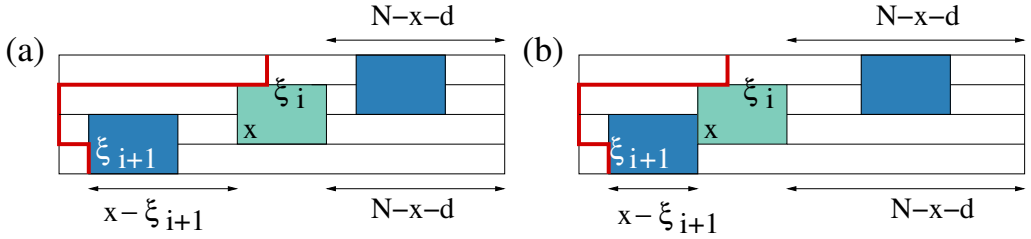

Figure 7.6: Two configurations with a single defect where the head of the defect (x) is such that $\max(\xi_i, \xi_{i+1}) - d < x < \max(\xi_i, \xi_{i+1})$. In (a) $\min(\xi_i, \xi_{i+1}) + d \leq \max(\xi_i, \xi_{i+1}) - d + 1$ and in (b) $\min(\xi_i, \xi_{i+1}) + d > \max(\xi_i, \xi_{i+1}) - d + 1$.

(2) $\max(\xi_i, \xi_{i+1}) - d < x < \max(\xi_i, \xi_{i+1})$

For the first case it is straightforward to realize that to accommodate the defect and the odd rectangles in the allowed x range, we have to impose a constraint

$$\max(\xi_i, \xi_{i+1}) - \min(\xi_i, \xi_{i+1}) \geq 2d. \tag{7.48}$$

This is equivalent to a restriction, $|\xi_{i+1} - \xi_i| \geq 2d$. The defect splits $i+1$-th row into two intervals, $x - \min(\xi_i, \xi_{i+1})$ and $N - x - d$ without affecting i-th row. Partition function of the first interval is $\omega_0(x - \min(\xi_i, \xi_{i+1}))$, from which we subtract out the null case to exclude the case of absence of an odd rectangle to the left of the defect. Thus we obtain $\Omega^{(1)}_{eo,R}$ for this aforementioned x range as,

$$\left.\frac{\Omega^{(1)}_{eo,R}}{\Omega^{(0)}_{eo,R}}\right|_{interface,(1)} = \sum_{i=1}^{M/2} \sum_{x=x'_R+d}^{x_R-2d} \frac{\omega_0(N-x-d)[\omega_0(x-x'_R)-1]\Theta(|\Delta\xi_i|-2d)}{\omega_0(N-x'_R)}, \tag{7.49}$$

where $x'_R = \min(\xi_i, \xi_{i+1})$.

For the second case there can be two scenarios

- $\min(\xi_i, \xi_{i+1}) + d \leq \max(\xi_i, \xi_{i+1}) - d + 1$ (see Fig. 7.6(a))
- $\min(\xi_i, \xi_{i+1}) + d > \max(\xi_i, \xi_{i+1}) - d + 1$ (see Fig. 7.6(b)).

Thus x can vary from $\max[\max(\xi_i, \xi_{i+1}) - d + 1, \min(\xi_i, \xi_{i+1}) + d]$ to $\max(\xi_i, \xi_{i+1}) - 1$. The

gap between ξ_i and ξ_{i+1} should be greater than or equal to $d+1$ to accommodate atleast an odd rectangle and the head of the defect,– thus $|\xi_{i+1}-\xi_i| \geq d+1$. The defect splits the $i+1$-th row into two open intervals of length $x-\min(\xi_i,\xi_{i+1})$ and $N-x-d$. We subtract out the null case from one dimensional partition function of the interval $x-\min(\xi_i,\xi_{i+1})$ to confirm the presence of atleast one odd rectangle on the left of the defect. Thus we obtain $\Omega^{(1)}_{eo,R}$ for the second x range as,

$$\left.\frac{\Omega^{(1)}_{eo,R}}{\Omega^{(0)}_{eo,R}}\right|_{interface,(2)} = \sum_{i=1}^{M/2}\sum_{x=x''_R}^{x_R-d-1} \frac{\omega_0^2(N-x-d)[\omega_0(x-x'_R)-1]\Theta(|\Delta\xi_i|-d-1)}{\omega_0(N-\xi_i)\omega_0(N-\xi_{i+1})} \tag{7.50}$$

where $x''_R = \max(x_R-2d+1, x'_R+d)$.

Thus adding these three cases (see Eqs, (7.47), (7.49) and (7.50)), we obtain,

$$\begin{aligned}\frac{\Omega^{(1)}_{eo,R}}{\Omega^{(0)}_{eo,R}} = \sum_{i=1}^{M/2}\Bigg[&\sum_{x=x_R-d}^{N-d} \frac{\omega_0^2(N-x-d)[\omega_0(x-\xi_i)\omega_0(x-\xi_{i+1})-1]}{\omega_0(N-\xi_i)\omega_0(N-\xi_{i+1})} \\ &+ \sum_{x=x''_R}^{x_R-d-1} \frac{\omega_0^2(N-x-d)[\omega_0(x-x'_R)-1]\Theta(|\Delta\xi_i|-d-1)}{\omega_0(N-\xi_i)\omega_0(N-\xi_{i+1})} \\ &+ \sum_{x=x'_R+d}^{x_R-2d} \frac{\omega_0(N-x-d)[\omega_0(x-x'_R)-1]\Theta(|\Delta\xi_i|-2d)}{\omega_0(N-x'_R)}\Bigg],\end{aligned} \tag{7.51}$$

In the sums, when x is not close to the lower or upper limits, we may substitute $\omega_0(\ell) \approx a\lambda^\ell$, else there are corrections due to the boundaries. To characterize these edge effects, we consider the partition function of a two-row system with a single defect and boundary as shown in Fig. 7.5(f). The partition function of this shape for large ℓ is

$$\sum_{x=0}^{\ell-d} \frac{\omega_0^2(x)\omega_0(\ell-x-d)\omega_0(\ell+\delta-x-d)}{\omega_0(\ell)\omega_0(\ell+\delta)} = \frac{a^2}{\lambda^{2d}}[(\ell-d+1)+f(0)+f(\delta)], \tag{7.52}$$

where $f(\delta)$ encodes the edge-effects,

$$f(\delta) = \left[2\sum_{p=2}^{d}\frac{a_p}{a}\frac{1}{1-\frac{\lambda_p}{\lambda}}\left(1+\left(\frac{\lambda_p}{\lambda}\right)^{|\delta|}\right) + \sum_{p,q=2}^{d}\frac{a_pa_q}{a^2}\frac{1}{1-\frac{\lambda_p\lambda_q}{\lambda^2}}\left(\frac{\lambda_p}{\lambda}\right)^{|\delta|}\right]. \tag{7.53}$$

Equations. (7.43), (7.45) and (7.51) may thus be simplified to

$$\frac{\Omega_{ee}^{(1)}}{\Omega_{ee}^{(0)}} = \frac{M}{2}\frac{a^2}{\lambda^{2d}}[(N-d+1)+2f(0)], \tag{7.54}$$

$$\frac{\Omega_{eo,L}^{(1)}}{\Omega_{eo,L}^{(0)}} = \frac{a^2}{\lambda^{2d}}\sum_{i=1}^{M/2}\left[x_L+1+f(0)+f(\Delta\eta_i)+p(|\Delta\eta_i|-3d)\right], \tag{7.55}$$

$$\frac{\Omega_{eo,R}^{(1)}}{\Omega_{eo,R}^{(0)}} = \frac{a^2}{\lambda^{2d}}\sum_{i=1}^{M/2}\left[N-x_R+1+f(0)+f(\Delta\xi_i)-\frac{a^{-2}\lambda^{-|\Delta\xi_i|}}{1-\lambda^{-2}}+p(|\Delta\xi_i|-2d)+q(|\Delta\xi_i|)\right], \tag{7.56}$$

where $\Delta\xi_i = \xi_{i+1}-\xi_i$, and $p(x)$ and $q(x)$ are defined as

$$p(x) = \left[\frac{\lambda^d}{a}(x+1)-\frac{1-\lambda^{-x-1}}{a^2(1-\lambda^{-1})}+\sum_{p=2}^{d}\frac{a_p\lambda_p^d}{a^2(1-\frac{\lambda_p}{\lambda})}\left(1-\left(\frac{\lambda_p}{\lambda}\right)^{x+1}\right)\right]\Theta(x), \tag{7.57}$$

$$q(x) = \frac{\Theta(x-d-1)}{a(1-\lambda^{-1})}\left[-1+\frac{\lambda^{-x}}{a(1+\lambda^{-1})}+\sqrt{\lambda}^{x-|x-2d+1|-1}-\frac{\lambda^{-|x-2d+1|-1}}{a(1+\lambda^{-1})}\right.$$
$$\left.+\sum_{p=2}^{d}\frac{a_p}{a}\frac{1-\lambda^{-1}}{1-\frac{\lambda_p}{\lambda^2}}\left(\frac{\lambda_p}{\lambda}\right)^x\left(\left(\frac{\lambda}{\lambda_p}\right)^{x-|x-2d+1|-1}-1\right)\right]. \tag{7.58}$$

The contribution from a single defect to the free energy of the interface, $H_{\text{eff}}^{(1)}(I)$ [see Eq. (7.16)] may now be evaluated from Eqs. (7.54), (7.55) and (7.56):

$$H_{\text{eff}}^{(1)}(I) = \frac{a^2}{\lambda^{2d}}\sum_{i=1}^{M/2}\left[2d-1+\frac{2|\Delta\eta_i|+|\Delta\xi_i|}{2}+\frac{a^{-2}\lambda^{-|\Delta\xi_i|}}{1-\lambda^{-2}}-f(\Delta\eta_i)-p(|\Delta\eta_i|-3d)-f(\Delta\xi_i)\right.$$
$$\left.-p(|\Delta\xi_i|-2d)-q(|\Delta\xi_i|)\right]. \tag{7.59}$$

Substituting Eq. (7.59) in Eq. (7.20) we obtain interfacial tension with one defect as

$$\sigma^{(1)}(z) = \frac{a^2}{M\lambda^{2d}}\sum_{i=1}^{M/2}\left[2d-1+\frac{\sqrt{\lambda}-1}{\sqrt{\lambda}+1}\sum_{\Delta\eta_i}(|\Delta\eta_i|-f(\Delta\eta_i)-p(|\Delta\eta_i|-3d))\sqrt{\lambda}^{-|\Delta\eta_i|}\right.$$
$$+\left(\frac{\sqrt{\lambda}-1}{\sqrt{\lambda}+1}\right)^2\sum_{\Delta\eta_i,\Delta\eta_{i+1}}\left(\frac{|\Delta\xi_i|}{2}-f(\Delta\xi_i)+\frac{a^{-2}\lambda^{-|\Delta\xi_i|}}{1-\lambda^{-2}}-p(|\Delta\xi_i|-2d)-q(|\Delta\xi_i|)\right)$$
$$\left.\times\sqrt{\lambda}^{-|\Delta\eta_i|-|\Delta\eta_{i+1}|}\right]. \tag{7.60}$$

Summing over $\Delta\eta$ and $\Delta\xi$s, each of the terms in Eq. (7.60) are evaluated to be

$$\frac{\sqrt{\lambda}-1}{\sqrt{\lambda}+1}\sum_{\Delta\eta_i}|\Delta\eta_i|\,\sqrt{\lambda}^{-|\Delta\eta_i|}=\frac{2\sqrt{\lambda}}{\lambda-1}, \tag{7.61}$$

$$\left(\frac{\sqrt{\lambda}-1}{\sqrt{\lambda}+1}\right)^2\sum_{\Delta\eta_i,\Delta\eta_{i+1}}\frac{|\tilde{\xi}_i|}{2}\,\sqrt{\lambda}^{-|\Delta\eta_i|-|\Delta\eta_{i+1}|}=\frac{\sqrt{\lambda}+\lambda+\lambda^{3/2}}{(\sqrt{\lambda}-1)(\sqrt{\lambda}+1)^3}, \tag{7.62}$$

$$\frac{a^{-2}}{1-\lambda^{-2}}\left(\frac{\sqrt{\lambda}-1}{\sqrt{\lambda}+1}\right)^2\sum_{\Delta\eta_i,\Delta\eta_{i+1}}\sqrt{\lambda}^{-2|\Delta\xi_i|-|\Delta\eta_i|-|\Delta\eta_{i+1}|}=\frac{\lambda^2}{a^2(\sqrt{\lambda}-1)(\sqrt{\lambda}+1)^3}, \tag{7.63}$$

$$\begin{aligned}\frac{\sqrt{\lambda}-1}{\sqrt{\lambda}+1}\sum_{\Delta\eta_i}f(\Delta\eta_i)\,\sqrt{\lambda}^{-|\Delta\eta_i|}&=2\sum_{p=2}^{d}\frac{a_p(\lambda^2-\lambda_p)}{a(1-\frac{\lambda_p}{\lambda})(\sqrt{\lambda}+1)(\lambda^{3/2}-\lambda_p)}\\&+\sum_{p,q=2}^{d}\frac{a_pa_q(\sqrt{\lambda}-1)(\lambda^3-\lambda_p\lambda_q)}{a^2(1-\frac{\lambda_p\lambda_q}{\lambda^2})(\sqrt{\lambda}+1)(\lambda^{3/2}-\lambda_p)(\lambda^{3/2}-\lambda_q)},\end{aligned} \tag{7.64}$$

$$\begin{aligned}&\left(\frac{\sqrt{\lambda}-1}{\sqrt{\lambda}+1}\right)^2\sum_{\Delta\eta_i,\Delta\eta_{i+1}}f(\Delta\xi_i)\,\sqrt{\lambda}^{-|\Delta\eta_i|-|\Delta\eta_{i+1}|}=2\sum_{p=2}^{d}\frac{a_p(2\lambda^2+2\lambda^{5/2}+\lambda^3-\lambda_p(1+2\sqrt{\lambda}+2\lambda))}{a(1-\frac{\lambda_p}{\lambda})(\sqrt{\lambda}+1)^3(\lambda^{3/2}-\lambda_p)}\\&+\sum_{p,q=2}^{d}\frac{a_pa_q(\lambda^3(\lambda^{3/2}+\lambda+\sqrt{\lambda}-1)-\lambda^2(\lambda_p+\lambda_q)(1+\sqrt{\lambda})+\lambda_p\lambda_q(1+\sqrt{\lambda}+\lambda-\lambda^{3/2})))}{a^2(1-\frac{\lambda_p\lambda_q}{\lambda^2})(\sqrt{\lambda}+1)^3(\lambda^{3/2}-\lambda_p)(\lambda^{3/2}-\lambda_q)},\end{aligned} \tag{7.65}$$

$$\begin{aligned}\frac{\sqrt{\lambda}-1}{\sqrt{\lambda}+1}\sum_{\Delta\eta_i}p(|\Delta\eta_i|-3d))\,\sqrt{\lambda}^{-|\Delta\eta_i|}&=\frac{2\lambda^{(1-3d)/2}(a(1-3d)\lambda^d-\frac{\lambda}{\lambda-1})}{a^2(\sqrt{\lambda}+1)}\\&+\frac{2\lambda^{(1-d)/2}(1+3d(\sqrt{\lambda}-1))}{a(\lambda-1)}+\frac{2\lambda^{-3(d-1)/2}}{a^2(\sqrt{\lambda}+1)^2(\lambda^{3/2}-1)}\\&+2\sum_{p=2}^{d}\frac{a_p\lambda^{-3(d-1)/2}\lambda_p^d}{a^2(\lambda-\lambda_p)(\sqrt{\lambda}+1)}\left(1-\frac{(\sqrt{\lambda}-1)\lambda_p}{\lambda^{3/2}-\lambda_p}\right),\end{aligned} \tag{7.66}$$

$$\left(\frac{\sqrt{\lambda}-1}{\sqrt{\lambda}+1}\right)^2 \sum_{\Delta\eta_i,\Delta\eta_{i+1}} p(|\Delta\xi_i|-2d)\,\sqrt{\lambda}^{-|\Delta\eta_i|-|\Delta\eta_{i+1}|} = \frac{2\lambda^{(1-2d)/2}(1+\sqrt{\lambda}+\lambda)(a(1-2d)\lambda^d-\frac{\lambda}{\lambda-1})}{a^2(\sqrt{\lambda}+1)^3}$$
$$+\frac{2\lambda^{(3-2d)/2}}{a^2(\sqrt{\lambda}-1)(\sqrt{\lambda}+1)^4}+\frac{2\sqrt{\lambda}(1+\sqrt{\lambda}+\lambda)(1+2d(\sqrt{\lambda}-1))}{a(\sqrt{\lambda}+1)^3(\sqrt{\lambda}-1)}$$
$$+2\sum_{p=2}^{d}\frac{a_p\lambda^{(3-2d)/2}\lambda_p^d(1+\sqrt{\lambda}+\lambda)}{a^2(\lambda-\lambda_p)(\sqrt{\lambda}+1)^3}\left(1-\frac{(\sqrt{\lambda}-1)\lambda_p}{\lambda^{3/2}-\lambda_p}\right), \qquad (7.67)$$

$$\left(\frac{\sqrt{\lambda}-1}{\sqrt{\lambda}+1}\right)^2 \sum_{\Delta\eta_i,\Delta\eta_{i+1}} q(|\Delta\xi_i|)\,\sqrt{\lambda}^{-|\Delta\eta_i|-|\Delta\eta_{i+1}|} = \frac{2\lambda^{2-\frac{3d}{2}}}{a^2\left(\sqrt{\lambda}+1\right)^3(\lambda^2-1)}-\frac{2\left(\lambda+\sqrt{\lambda}+1\right)\lambda^{1-\frac{d}{2}}}{a\left(\sqrt{\lambda}-1\right)\left(\sqrt{\lambda}+1\right)^4}$$
$$-\frac{2\lambda^{1-\frac{3d}{2}}\left(2\lambda^{\frac{d}{2}+1}+3\lambda^{\frac{d}{2}+2}+\lambda^{\frac{d}{2}+3}+\lambda^{\frac{d+1}{2}}+3\lambda^{\frac{d+3}{2}}+2\lambda^{\frac{d+5}{2}}-\lambda^{3/2}-3\lambda^{5/2}-\lambda^{7/2}-2\lambda^3-2\lambda^2\right)}{a^2\left(\sqrt{\lambda}+1\right)^4(\lambda^{3/2}+\lambda^{5/2}-\lambda-1)}$$
$$+\frac{2\left(-2\lambda^{2-\frac{d}{2}}-2\lambda^{3-\frac{d}{2}}-\lambda^{\frac{3}{2}-\frac{d}{2}}-3\lambda^{\frac{5}{2}-\frac{d}{2}}-\lambda^{\frac{7}{2}-\frac{d}{2}}+5\lambda^{3/2}+3\lambda^{5/2}+\lambda^3+5\lambda^2+3\lambda+\sqrt{\lambda}\right)}{a\left(\sqrt{\lambda}+1\right)^4(\lambda^{3/2}-1)}$$
$$-2\sum_{p=2}^{d}\frac{a_p\lambda^2}{a^2(\lambda^2-\lambda_p)}\frac{\lambda^{-3d/2}(\lambda^{\frac{3}{2}}-1)\lambda_p^{d+1}}{(\sqrt{\lambda}+1)^3(\lambda^{\frac{3}{2}}-\lambda_p)}$$
$$+2\sum_{p=2}^{d}\frac{a_p\lambda^2}{a^2(\lambda^2-\lambda_p)}\Bigg[\lambda^{-1-2d}\Bigg(\lambda^3\lambda_p(\sqrt{\lambda}\sqrt{\lambda_p})^{2d-1}-\lambda\lambda_p^{3/2}\left(\sqrt{\lambda}\sqrt{\lambda_p}\right)^{2d}-2\lambda^{\frac{d}{2}+3}\lambda_p^{d+\frac{1}{2}}$$
$$-2\lambda^{\frac{d}{2}+4}\lambda_p^{d+\frac{1}{2}}-\lambda^{d+2}\lambda_p^{d+\frac{1}{2}}+2\lambda^{d+\frac{5}{2}}\lambda_p^{d+\frac{1}{2}}+2\lambda^{d+3}\lambda_p^{d+\frac{1}{2}}+2\lambda^{d+\frac{7}{2}}\lambda_p^{d+\frac{1}{2}}$$
$$-2\lambda^{\frac{d+7}{2}}\lambda_p^{d+\frac{1}{2}}+2\lambda^{\frac{d}{2}+2}\lambda_p^{d+\frac{3}{2}}-\lambda^{d+\frac{1}{2}}\lambda_p^{d+\frac{3}{2}}-2\lambda^{d+1}\lambda_p^{d+\frac{3}{2}}-2\lambda^{d+\frac{3}{2}}\lambda_p^{d+\frac{3}{2}}$$
$$+2\lambda^{\frac{d+3}{2}}\lambda_p^{d+\frac{3}{2}}+2\lambda^{\frac{d+5}{2}}\lambda_p^{d+\frac{3}{2}}\Bigg)\Bigg/\left(\left(\sqrt{\lambda}+1\right)^3\sqrt{\lambda_p}\left(\lambda^{3/2}-\lambda_p\right)\right)\Bigg]. \qquad (7.68)$$

Substituting Eqs. (7.61), (7.62), (7.63), (7.64), (7.65), (7.66), (7.67), and (7.68) in Eq. (7.60) we obtain,

$$
\begin{aligned}
\sigma^{(1)}(z) = \frac{a^2\lambda^{-2d}}{2}\Bigg[& 2d-1+\frac{2\sqrt{\lambda}}{\lambda-1}+\frac{\sqrt{\lambda}+\lambda+\lambda^{3/2}}{(\sqrt{\lambda}-1)(\sqrt{\lambda}+1)^3}+\frac{\lambda^2}{a^2(\sqrt{\lambda}-1)(\sqrt{\lambda}+1)^3} \\
& -2\sum_{p=2}^{d}\frac{a_p(\lambda^2-\lambda_p)}{a(1-\frac{\lambda_p}{\lambda})(\sqrt{\lambda}+1)(\lambda^{3/2}-\lambda_p)}-\sum_{p,q=2}^{d}\frac{a_pa_q(\sqrt{\lambda}-1)(\lambda^3-\lambda_p\lambda_q)}{a^2(1-\frac{\lambda_p\lambda_q}{\lambda^2})(\sqrt{\lambda}+1)(\lambda^{3/2}-\lambda_p)(\lambda^{3/2}-\lambda_q)} \\
& -2\sum_{p=2}^{d}\frac{a_p(2\lambda^2+2\lambda^{5/2}+\lambda^3-\lambda_p(1+2\sqrt{\lambda}+2\lambda))}{a(1-\frac{\lambda_p}{\lambda})(\sqrt{\lambda}+1)^3(\lambda^{3/2}-\lambda_p)} \\
& -\sum_{p,q=2}^{d}\frac{a_pa_q(\lambda^3(\lambda^{3/2}+\lambda+\sqrt{\lambda}-1)-\lambda^2(\lambda_p+\lambda_q)(1+\sqrt{\lambda})+\lambda_p\lambda_q(1+\sqrt{\lambda}+\lambda-\lambda^{3/2})))}{a^2(1-\frac{\lambda_p\lambda_q}{\lambda^2})(\sqrt{\lambda}+1)^3(\lambda^{3/2}-\lambda_p)(\lambda^{3/2}-\lambda_q)} \\
& -\frac{2\lambda^{(1-3d)/2}(a(1-3d)\lambda^d-\frac{\lambda}{\lambda-1})}{a^2(\sqrt{\lambda}+1)}-\frac{2\lambda^{(1-d)/2}(1+3d(\sqrt{\lambda}-1))}{a(\lambda-1)}-\frac{2\lambda^{-3(d-1)/2}}{a^2(\sqrt{\lambda}+1)^2(\lambda^{3/2}-1)} \\
& -2\sum_{p=2}^{d}\frac{a_p\lambda^{-3(d-1)/2}\lambda_p^d}{a^2(\lambda-\lambda_p)(\sqrt{\lambda}+1)}\left(1-\frac{(\sqrt{\lambda}-1)\lambda_p}{\lambda^{3/2}-\lambda_p}\right) \\
& -\frac{2\lambda^{(3-2d)/2}}{a^2(\sqrt{\lambda}-1)(\sqrt{\lambda}+1)^4}-\frac{2\sqrt{\lambda}(1+\sqrt{\lambda}+\lambda)(1+2d(\sqrt{\lambda}-1))}{a(\sqrt{\lambda}+1)^3(\sqrt{\lambda}-1)} \\
& -2\sum_{p=2}^{d}\frac{a_p\lambda^{(3-2d)/2}\lambda_p^d(1+\sqrt{\lambda}+\lambda)}{a^2(\lambda-\lambda_p)(\sqrt{\lambda}+1)^3}\left(1-\frac{(\sqrt{\lambda}-1)\lambda_p}{\lambda^{3/2}-\lambda_p}\right)-\frac{2\lambda^{2-\frac{3d}{2}}}{a^2\left(\sqrt{\lambda}+1\right)^3(\lambda^2-1)} \\
& +\frac{2\left(\lambda+\sqrt{\lambda}+1\right)\lambda^{1-\frac{d}{2}}}{a\left(\sqrt{\lambda}-1\right)\left(\sqrt{\lambda}+1\right)^4}-\frac{2\lambda^{(1-2d)/2}(1+\sqrt{\lambda}+\lambda)(a(1-2d)\lambda^d-\frac{\lambda}{\lambda-1})}{a^2(\sqrt{\lambda}+1)^3} \\
& -\frac{2\left(-2\lambda^{2-\frac{d}{2}}-2\lambda^{3-\frac{d}{2}}-\lambda^{\frac{3}{2}-\frac{d}{2}}-3\lambda^{\frac{5}{2}-\frac{d}{2}}-\lambda^{\frac{7}{2}-\frac{d}{2}}+5\lambda^{3/2}+3\lambda^{5/2}+\lambda^3+5\lambda^2+3\lambda+\sqrt{\lambda}\right)}{a\left(\sqrt{\lambda}+1\right)^4(\lambda^{3/2}-1)} \\
& +\frac{2\lambda^{1-\frac{3d}{2}}\left(2\lambda^{\frac{d}{2}+1}+3\lambda^{\frac{d}{2}+2}+\lambda^{\frac{d}{2}+3}+\lambda^{\frac{d+1}{2}}+3\lambda^{\frac{d+3}{2}}+2\lambda^{\frac{d+5}{2}}-\lambda^{3/2}-3\lambda^{5/2}-\lambda^{7/2}-2\lambda^3-2\lambda^2\right)}{a^2\left(\sqrt{\lambda}+1\right)^4(\lambda^{3/2}+\lambda^{5/2}-\lambda-1)} \\
& -2\sum_{p=2}^{d}\frac{a_p\lambda^2}{a^2(\lambda^2-\lambda_p)}\Bigg[\lambda^{-1-2d}\Bigg(\lambda^3\lambda_p(\sqrt{\lambda}\sqrt{\lambda_p})^{2d-1}-\lambda\lambda_p^{3/2}\left(\sqrt{\lambda}\sqrt{\lambda_p}\right)^{2d}-2\lambda^{\frac{d}{2}+3}\lambda_p^{d+\frac{1}{2}}-\lambda^{d+2}\lambda_p^{d+\frac{1}{2}} \\
& -2\lambda^{\frac{d}{2}+4}\lambda_p^{d+\frac{1}{2}}+2\lambda^{d+\frac{5}{2}}\lambda_p^{d+\frac{1}{2}}+2\lambda^{d+3}\lambda_p^{d+\frac{1}{2}}+2\lambda^{d+\frac{7}{2}}\lambda_p^{d+\frac{1}{2}}-2\lambda^{\frac{d+7}{2}}\lambda_p^{d+\frac{1}{2}}+2\lambda^{\frac{d}{2}+2}\lambda_p^{d+\frac{3}{2}}-\lambda^{d+\frac{1}{2}}\lambda_p^{d+\frac{3}{2}} \\
& -2\lambda^{d+1}\lambda_p^{d+\frac{3}{2}}-2\lambda^{d+\frac{3}{2}}\lambda_p^{d+\frac{3}{2}}+2\lambda^{\frac{d+3}{2}}\lambda_p^{d+\frac{3}{2}}+2\lambda^{\frac{d+5}{2}}\lambda_p^{d+\frac{3}{2}}\Bigg)\Bigg/\left(\left(\sqrt{\lambda}+1\right)^3\sqrt{\lambda_p}\left(\lambda^{3/2}-\lambda_p\right)\right)\Bigg] \\
& +2\sum_{p=2}^{d}\frac{a_p\lambda^2}{a^2(\lambda^2-\lambda_p)}\frac{\lambda^{-3d/2}(\lambda^{\frac{3}{2}}-1)\lambda_p^{d+1}}{(\sqrt{\lambda}+1)^3(\lambda^{\frac{3}{2}}-\lambda_p)}\Bigg].
\end{aligned}
\tag{7.69}
$$

The variation interfacial tension, $\sigma(z) = \sigma^{(0)}(z) + z_D\sigma^{(1)}(z)$, with z is shown in Fig. 7.7.

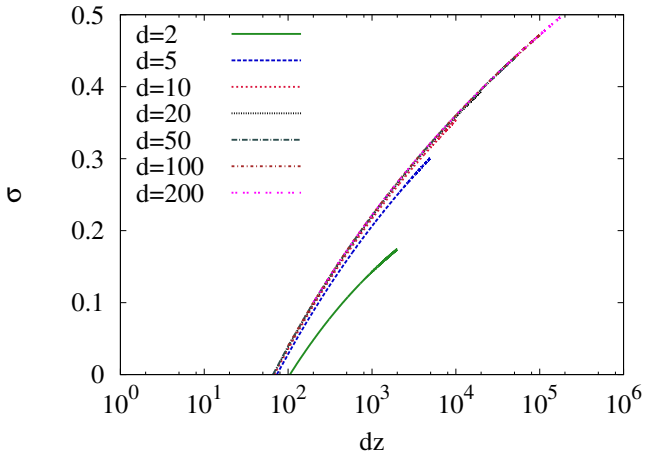

Figure 7.7: Variation of interfacial tension $\sigma(z)$ truncated at order z_D with dz

The function decreases monotonically with decreasing z till it becomes zero at z_c. Near z_c, it varies as $|z - z_c|$.

The bulk density may be calculated from Ω_{ee} (Eq. (7.54)),

$$\Omega_{ee} = [\omega_0(N)]^{M/2}\left(1 + z_D\frac{M}{2}\frac{a^2}{\lambda^{2d}}[(N-d+1) + 2f(0)] + O(z_D^2)\right). \tag{7.70}$$

At thermodynamic limit, free energy per site is thus given by,

$$f = -\frac{1}{2}\left[\ln\lambda + z_D a^2\lambda^{-2d}\right] + O(z_D^2). \tag{7.71}$$

Density of rectangles, $\rho(d)$ is defined as

$$\rho(d) = -dz\frac{d}{dz}f, \tag{7.72}$$

which may be simplified to

$$\rho(d) = 1 - \frac{a}{\lambda} + z_D a^2\lambda^{-1-2d}\left[2a(d(a+1)-1) - \lambda(d(2a+1)-2)\right] + O(z_D^2). \tag{7.73}$$

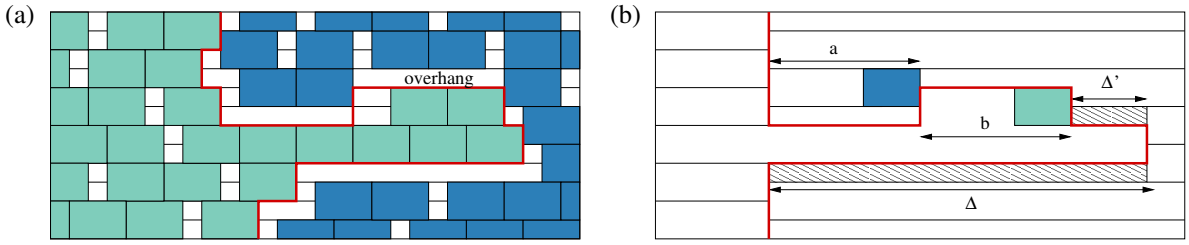

Figure 7.8: (a) A configuration in which the interface has one overhang. (b) A schematic configuration with one overhang of height one and otherwise flat interface.

By equating $\sigma(z) = \sigma^{(0)}(z) + z_D\sigma^{(1)}(z)$ to zero we obtain

$$z_c^*(d) = 65.23d^{-1} + O(d^{-2}), \tag{7.74}$$

$$\rho_c^*(d) = 0.746 + 0.374d^{-1} + O(d^{-2}). \tag{7.75}$$

For hard squares, we obtain $z_c^*(2) = 52.49$ and $\rho_c^*(2) = 0.923$. These results and those for general d are compared with the Monte Carlo results as well as the contribution from zero defects in Fig. 7.3. The one defect calculation improves the estimates for $z_c(d)$ and $\rho_c(d)$ for all $d > 2$. For $d = 2$, while $z_c(2)$ increases towards the Monte Carlo results, $\rho_c(2)$ decreases slightly away from the Monte Carlo results.

7.5 Calculation including overhangs

Another improvement over the zero defect calculation would be to include in the sum over interfaces, interfaces with overhangs. In this calculation, we assume perfect columnar order in each of the phases to the left or right of interface. We consider all interfaces in which the overhangs have height at most 1. These interfaces may be defined as self-avoiding walks such that if the walk once reaches the layer y it never goes to the layer $y-4$ any time later, but may go back to $y-2$, a single vertical step of the walk being of length two lattice spacings. An interface with one overhang of height 1 is shown in Fig. 7.8.

Consider a configuration with overhangs in one row on the right of the interface and

otherwise flat interface (see Fig. 7.8(b)). We define the left boundary of each overhang positioning the odd rectangle as far right as possible in the depression region preceding the overhang. To avoid overlap between the interface and overhangs, we impose the constraint that on the left of the depression region, either equal number of left and right steps or only right steps should be present. Similarly on the right of the overhang only right steps are allowed. Thus it is easily seen that an overhang configuration consists of sequence of steps of the type $R^a U R^b D$, where $a, b > d$. Define

$$W_R = \sum_{a,b\geq d}^{\infty} R^a U R^b D, \tag{7.76}$$

$$W_R^* = W_R + W_R W_R + W_R W_R W_R + \ldots, \tag{7.77}$$

and a similar definition for sum over overhang configurations to the left W_L^*. W_R^* and W_L^* generate overhangs of height 1.

Weight of a configuration with a given values of a and b (see Fig. 7.8(b)) is given by,

$$\Omega_{ov} = [za\lambda^{-d}]^{M/2} z^2 \lambda^{-\Delta-a-b} \omega_0(a-d)\omega_0(b-d). \tag{7.78}$$

Since weight of each vertical step is $za\lambda^{-d}$ and the two hatched wasted spaces are not due to the overhang, weight of the overhang is

$$u = z^2 \lambda^{-\Delta-a-b} \omega_0(a-d)\omega_0(b-d)\sqrt{\lambda}^{\Delta+\Delta'} = z^2 \lambda^{-\frac{3}{2}(a+b)} \omega_0(a-d)\omega_0(b-d). \tag{7.79}$$

Then summing over a, and b, we get weight of all possible overhangs of height 1,

$$\mathbb{W}_R = \sum_{a=d}^{\infty} \sum_{b=d}^{\infty} z^2 \lambda^{-\frac{3}{2}(a+b)} \omega_0(a-d)\omega_0(b-d). \tag{7.80}$$

The generating function of partition function of a system of hard rods of length d on a one

dimensional open chain ω_0 is given by

$$\sum_j \omega_0(j)x^j = \frac{1}{1-x-zx^d}. \tag{7.81}$$

Substituting the generating function, Eq. (7.80) can be simplified to

$$\mathbb{W}_R = [z\lambda^{-\frac{3d}{2}}]^2 \left[\sum_{n=0}^{\infty} \omega_0(n)\lambda^{-\frac{3n}{2}}\right]^2, \tag{7.82}$$

$$= \left[\frac{z\lambda^{-\frac{3d}{2}}}{1-\lambda^{-3/2}-(1-\lambda^{-1})\lambda^{-d/2}}\right]^2. \tag{7.83}$$

A general configuration with overhangs of height at most 1 is an arbitrary concatenation of subsequences D, DR^*, DL^*, X_L and X_R, where

$$X_R = D\left(\left(\sum_{n\geq 0} L^n D R^n\right) + R^* D\right) W_R^*(1+R^*), \tag{7.84}$$

$$X_L = D\left(\left(\sum_{n\geq 0} R^n D L^n\right) + L^* D\right) W_L^*(1+L^*). \tag{7.85}$$

$$\tag{7.86}$$

Thus the criterion for divergence of the generating function gets modified to

$$\mathbb{D}\left(1+2\mathbb{R}^*+2\left(\frac{1}{1-\mathbb{L}\mathbb{R}}+\mathbb{R}^*\right)\frac{\mathbb{D}\mathbb{W}_R(1+\mathbb{R}^*)}{(1-\mathbb{W}_R)}\right)=1, \tag{7.87}$$

which can be simplified to

$$\frac{\lambda-1}{d(\lambda-1)+1}\left(\frac{\sqrt{\lambda}+1}{\sqrt{\lambda}-1}+\frac{2\sqrt{\lambda}(1+\sqrt{\lambda}+\lambda)\mathbb{W}_R}{(d(\lambda-1)+1)(\sqrt{\lambda}-1)(1-\mathbb{W}_R)}\right)=1. \tag{7.88}$$

From the divergence condition, we obtain the estimates of the critical parameters as,

$$z_c^{**}(d) = 67.78d^{-1}+O(d^{-2}), \tag{7.89}$$

$$\rho_c^{**}(d) = 0.755+0.382d^{-1}+O(d^{-2}), \tag{7.90}$$

and $z_c^{**}(2) = 54.87$ and $\rho_c^{**}(2) = 0.9326$. These are an improvement over the estimates of $z_c(d)$ from the one defect calculations [see Fig. 7.3 for comparison]. However, the calculation of overhangs does not affect the bulk quantities, and therefore the estimates for critical density $\rho_c(d)$ increase. While the estimates for $\rho_c(d)$ matches with the Monte Carlo result for $d = 2$, it increases away from the Monte Carlo results for $d > 2$.

7.6 Discussion

In this chapter, we determined the critical activity and critical density of transition between the nematic and columnar phases in the problem of $2 \times d$ oriented rectangles on a square lattice approximately, by estimating the interfacial tension between two differently ordered columnar phases. This was done in two ways: first in terms of a perturbation series in number of defects, and second by including a subset of overhangs in the interface. Keeping only the first order terms in the expansion in the first case and overhangs of height 1 in the second case, we obtain estimates that are in fair agreement with Monte Carlo results and an improvement over earlier estimates. For example, when $d = 2$, Monte Carlo estimates are $z_c(2) \approx 97.5$, and $\rho_c(2) \approx 0.932$, while we obtain $z_c(2) = 52.49$ and 54.87, and $\rho_c(2) = 0.923$ and 0.932. These should be compared with estimates from high density expansion ($z_c(2) = 14.86$) [11, 19], a lattice version of density functional theory ($z_c(2) = 11.09$) [23, 24] an approximate counting method using transfer matrices ($z_c(2) = 11.09$) [25], a Flory type mean-field theory (with similar prediction) [26], and cluster variational method ($z_c(2) = 17.22$) [11]. A calculation of interfacial tension in the next nearest neighbour Ising antiferromagnet, gives a better estimate $z_c(2) = 135.9$ [22], still off by about 40%. For the critical density, the high density expansion gives $\rho_c(2) = 0.75$, cluster variation method gives $\rho_c(2) = 0.80$, and the transfer matrix calculations $\rho_c(2) = 0.76$. Likewise, we obtain significantly better estimates for the critical parameters for the hard rectangle gas also. These may be systematically improved by including more defects or overhangs. The effect of multiple defects in the calculation

of the interfacial tension may be incorporated within certain approximations. In a recent study, by approximating the partition function as a product of partition functions of tracks of width 4, we obtained an improved estimate of $z_c(2) = 105.35$ for the critical activity, and an estimate of $\rho_c(2) = 0.947$ for the critical density [200]. The calculations may be extended to a system of rectangles of same width and different lengths. In this case, the zero defect calculation gives $\rho_c^{(i)}/d_i + 2\sqrt{1 - \sum_i \rho_c^{(i)}} = 1$, where d_i are the different lengths. Similar results may be derived for mixtures of squares and dimers [92].

The interfacial tension was calculated for a system with only horizontal rectangles. However, it is straightforward to show that for large d, adding vertical rectangles introduces only exponentially small (in d) corrections to the critical density. For $d = 2$, this approximation is irrelevant. However, for small $d > 2$, the effects are not negligible [20, 182].

On general grounds, the nematic-columnar transition is expected to be in the Ising universality class [20, 182]. In our calculation, the interfacial tension varies as $|z - z_c|$ near the transition point, consistent with the behaviour in the Ising universality class [201].

Bibliography

[1] P. N. Pusey and W. van Megan *Nature*, vol. 320, no. 6060, p. 340, 1986.

[2] B. J. Alder and T. E. Wainwright *J. Chem. Phys.*, vol. 27, no. 5, pp. 1208–1209, 1957.

[3] P. de Gennes and J. Prost, *The physics of liquid crystals*, vol. 23 of *International series of monographs on physics*. Oxford University Press, 1995.

[4] D. E. Taylor, E. D. Williams, R. L. Park, N. C. Bartelt, and T. L. Einstein *Phys. Rev. B*, vol. 32, no. 7, pp. 4653–4659, 1985.

[5] L. K. Runnels, *Phase Transitions and Critical Phenomena, Vol. 2, edited by C. Domb and MS Green*. Academic Press, London, 1972.

[6] L. Onsager *Ann. N.Y. Acad. Sci.*, vol. 51, no. 4, pp. 627–659, 1949.

[7] R. J. Baxter *J. Phys. A*, vol. 13, no. 3, p. L61, 1980.

[8] J. Bouttier, P. D. Francesco, and E. Guitter *J. Phys. A*, vol. 35, no. 17, pp. 3821–3854, 2002.

[9] H. C. M. Fernandes, J. J. Arenzon, and Y. Levin *J. Chem. Phys.*, vol. 126, no. 11, p. 114508, 2007.

[10] D. S. Gaunt and M. E. Fisher *J. Chem. Phys.*, vol. 43, no. 8, pp. 2840–2863, 1965.

[11] A. Bellemans and R. K. Nigam *J. Chem. Phys.*, vol. 46, no. 8, pp. 2922–2935, 1967.

[12] X. Feng, H. W. J. Blöte, and B. Nienhuis *Phys. Rev. E*, vol. 83, no. 6, p. 061153, 2011.

[13] M. E. Zhitomirsky and H. Tsunetsugu *Phys. Rev. B*, vol. 75, no. 22, p. 224416, 2007.

[14] R. M. Nisbet and I. E. Farquhar *Physica*, vol. 73, no. 2, pp. 351–367, 1974.

[15] Z. Rotman and E. Eisenberg *Phys. Rev. E*, vol. 80, no. 3, p. 031126, 2009.

[16] E. P. Bernard and W. Krauth *Phys. Rev. Lett.*, vol. 107, no. 15, p. 155704, 2011.

[17] O. J. Heilmann and E. Praestgaard *J. Phys. A*, vol. 7, no. 15, pp. 1913–1917, 1974.

[18] M. Disertori and A. Giuliani *Commun. Math. Phys.*, vol. 323, no. 1, pp. 143–175, 2013.

[19] K. Ramola and D. Dhar *Phys. Rev. E*, vol. 86, no. 3, p. 031135, 2012.

[20] J. Kundu and R. Rajesh *Phys. Rev. E*, vol. 89, no. 5, p. 052124, 2014.

[21] J. Kundu and R. Rajesh *Phys. Rev. E*, vol. 91, no. 1, p. 012105, 2015.

[22] P. A. Slotte *J. Phys. C*, vol. 16, no. 15, pp. 2935–2951, 1983.

[23] L. Lafuente and J. A. Cuesta *J. Chem. Phys.*, vol. 119, no. 20, pp. 10832–10843, 2003.

[24] L. Lafuente and J. A. Cuesta *J. Phys.*, vol. 14, no. 46, pp. 12079–12097, 2002.

[25] H. Temperley *Proc. Phys. Soc.*, vol. 77, no. 3, pp. 630–642, 1961.

[26] H. C. M. Fernandes, Y. Levin, and J. J. Arenzon *Phys. Rev. E*, vol. 75, no. 5, p. 052101, 2007.

[27] D. Frenkel *Physica A*, vol. 263, no. 1, pp. 26–38, 1999.

[28] A. Patrykiejew, S. Sokołowski, and K. Binder *Surf. Sci. Rep.*, vol. 37, no. 6–8, pp. 207–344, 2000.

[29] S. Asakura and F. Oosawa *J. Polym. Sci.*, vol. 33, no. 126, pp. 183–192, 1958.

[30] D. Frenkel and A. A. Louis *Phys. Rev. Lett.*, vol. 68, no. 22, pp. 3363–3365, 1992.

[31] W. G. Hoover and F. H. Ree *J. Chem. Phys.*, vol. 49, no. 8, pp. 3609–3617, 1968.

[32] S. Mitchell, G. Brown, and P. Rikvold *Surf. Sci.*, vol. 471, no. 1–3, pp. 125–142, 2001.

[33] M. T. M. Koper, *Statistical Mechanics and Kinetic Modeling of Electrochemical Reactions on Single-Crystal Electrodes Using the Lattice-Gas Approximation*, pp. 75–98. Wiley-VCH Verlag GmbH & Co. KGaA, 2013.

[34] M. T. Koper *J. Electroanal. Chem.*, vol. 450, no. 2, pp. 189 – 201, 1998.

[35] P. Bak, P. Kleban, W. N. Unertl, J. Ochab, G. Akinci, N. C. Bartelt, and T. L. Einstein *Phys. Rev. Lett.*, vol. 54, no. 14, pp. 1539–1542, 1985.

[36] Y. Zhang, V. Blum, and K. Reuter *Phys. Rev. B*, vol. 75, no. 23, p. 235406, 2007.

[37] N. Bartelt, L. Roelofs, and T. Einstein *Surf. Sci. Lett.*, vol. 221, no. 3, pp. L750 – L758, 1989.

[38] K. Zhao, R. Bruinsma, and T. G. Mason *Proc. Natl. Acad. Sci.*, vol. 108, no. 7, pp. 2684–2687, 2011.

[39] K. Zhao, C. Harrison, D. Huse, W. B. Russel, and P. M. Chaikin *Phys. Rev. E*, vol. 76, no. 4, p. 040401, 2007.

[40] A. Donev, J. Burton, F. H. Stillinger, and S. Torquato *Phys. Rev. B*, vol. 73, no. 5, p. 054109, 2006.

[41] C. Avendaño and F. A. Escobedo *Soft Matter*, vol. 8, no. 17, pp. 4675–4681, 2012.

[42] P. Bolhuis and D. Frenkel *J. Chem. Phys.*, vol. 106, no. 2, pp. 666–687, 1997.

[43] M. A. Bates and D. Frenkel *J. Chem. Phys*, vol. 109, no. 14, pp. 6193–6199, 1998.

[44] E. Frezza, A. Ferrarini, H. B. Kolli, A. Giacometti, and G. Cinacchi *J. Chem. Phys.*, vol. 138, no. 16, p. 164906, 2013.

[45] T. Schilling, S. Pronk, B. Mulder, and D. Frenkel *Phys. Rev. E*, vol. 71, no. 3, p. 036138, 2005.

[46] K. Zhao and T. G. Mason *Phys. Rev. Lett.*, vol. 103, no. 20, p. 208302, 2009.

[47] M. P. Allen, G. T. Evans, D. Frenkel, and B. M. Mulder, *Hard Convex Body Fluids*, pp. 1–166. John Wiley & Sons, Inc., 2007.

[48] M. Marechal, R. J. Kortschot, A. F. Demirörs, A. Imhof, and M. Dijkstra *Nano letters*, vol. 10, no. 5, pp. 1907–1911, 2010.

[49] W. Qi, J. de Graaf, F. Qiao, S. Marras, L. Manna, and M. Dijkstra *J. Chem. Phys.*, vol. 138, no. 15, p. 154504, 2013.

[50] S. Atkinson, Y. Jiao, and S. Torquato *Phys. Rev. E*, vol. 86, no. 3, p. 031302, 2012.

[51] M. Marechal and M. Dijkstra *Soft matter*, vol. 7, no. 4, pp. 1397–1408, 2010.

[52] M. Marechal and H. Löwen *Phys. Rev. Lett.*, vol. 110, no. 13, p. 137801, 2013.

[53] J. A. Martínez-González, S. Varga, P. Gurin, and J. Quintana-H. *Europhys. Lett.*, vol. 97, no. 2, p. 26004, 2012.

[54] S. Varga, P. Gurin, J. C. Armas-Pérez, and J. Quintana-H *J. Chem. Phys.*, vol. 131, no. 18, p. 184901, 2009.

[55] R. Tavarone, P. Charbonneau, and H. Stark *J. Chem. Phys.*, vol. 143, no. 11, p. 114505, 2015.

[56] J. A. C. Veerman and D. Frenkel *Phys. Rev. A*, vol. 45, no. 8, pp. 5632–5648, 1992.

[57] Y. Han, J. Lee, S. Q. Choi, M. C. Choi, and M. W. Kim *Phys. Rev. E*, vol. 88, no. 4, p. 042202, 2013.

[58] D. de las Heras, Y. Martínez-Ratón, and E. Velasco *Phys. Rev. E*, vol. 76, no. 3, p. 031704, 2007.

[59] G. J. Vroege and H. N. W. Lekkerkerker *J. Phys. Chem.*, vol. 97, no. 14, pp. 3601–3605, 1993.

[60] R. van Roij and B. Mulder *Phys. Rev. E*, vol. 54, no. 6, pp. 6430–6440, 1996.

[61] R. van Roij, B. Mulder, and M. Dijkstra *Phys. A*, vol. 261, no. 3–4, pp. 374–390, 1998.

[62] H. N. W. Lekkerkerker, P. Buining, J. Buitenhuis, G. J. Vroege, and A. Stroobants, ch. Liquid Crystal Phase Transitions in Dispersions of Rodlike Colloidal Particles, pp. 53–112. Dordrecht: Springer Netherlands, 1995.

[63] S. Fraden, G. Maret, D. L. D. Caspar, and R. B. Meyer *Phys. Rev. Lett.*, vol. 63, no. 19, p. 2068, 1989.

[64] X. Wen, R. B. Meyer, and D. L. D. Caspar *Phys. Rev. Lett.*, vol. 63, no. 25, p. 2760, 1989.

[65] Z. Dogic and S. Fraden, *Phase Behavior of Rod-Like Viruses and Virus–Sphere Mixtures*, pp. 1–86. Wiley-VCH Verlag GmbH & Co. KGaA, 2007.

[66] E. Grelet *Phys. Rev. Lett.*, vol. 100, no. 16, p. 168301, 2008.

[67] A. Kuijk, A. v. Blaaderen, and A. Imhof *J. Am. Chem. Soc.*, vol. 133, no. 8, pp. 2346–2349, 2011.

[68] A. Kuijk, D. V. Byelov, A. V. Petukhov, A. v. Blaaderen, and A. Imhof *Faraday Discuss.*, vol. 159, pp. 181–199, 2012.

[69] H. Zocher *Zeitschrift für anorganische und allgemeine Chemie*, vol. 147, no. 1, pp. 91–110, 1925.

[70] M. P. B. van Bruggen, F. M. van der Kooij, and H. N. W. Lekkerkerker *J. Phys.*, vol. 8, no. 47, pp. 9451–9456, 1996.

[71] W. Qi, J. de Graaf, F. Qiao, S. Marras, L. Manna, and M. Dijkstra *Nano Letters*, vol. 12, no. 10, pp. 5299–5303, 2012.

[72] K. Zhao and T. G. Mason *J. Phys.*, vol. 26, no. 15, p. 152101, 2014.

[73] Y. Maeda, T. Niori, J. Yamamoto, and H. Yokoyama *Thermochim. Acta*, vol. 431, no. 1–2, pp. 87–93, 2005.

[74] B. J. Alder and T. E. Wainwright *Phys. Rev.*, vol. 127, no. 2, pp. 359–361, 1962.

[75] D. Dhar *Phys. Rev. Lett.*, vol. 49, no. 14, pp. 959–962, 1982.

[76] D. Dhar *Phys. Rev. Lett.*, vol. 51, no. 10, pp. 853–856, 1983.

[77] D. C. Brydges and J. Z. Imbrie *J. Stat. Phys.*, vol. 110, no. 3-6, pp. 503–518, 2003.

[78] G. Parisi and N. Sourlas *Phys. Rev. Lett.*, vol. 46, no. 14, pp. 871–874, 1981.

[79] P. A. Pearce and K. A. Seaton *J. Stat. Phys.*, vol. 53, no. 5-6, pp. 1061–1072, 1988.

[80] R. Dickman *J. Chem. Phys.*, vol. 136, no. 17, p. 174105, 2012.

[81] F. Alet, Y. Ikhlef, J. L. Jacobsen, G. Misguich, and V. Pasquier *Phys. Rev. E*, vol. 74, no. 4, p. 041124, 2006.

[82] O. J. Heilmann and E. Lieb *Commun. Math. Phys.*, vol. 25, no. 3, pp. 190–232, 1972.

[83] H. Kunz *Phys. Lett. A*, vol. 32, no. 5, pp. 311–312, 1970.

[84] O. J. Heilmann and E. H. Lieb *Phys. Rev. Lett.*, vol. 24, no. 25, pp. 1412–1414, 1970.

[85] P. W. Kasteleyn *Physica*, vol. 27, no. 12, pp. 1209–1225, 1961.

[86] A. Verberkmoes and B. Nienhuis *Phys. Rev. Lett.*, vol. 83, no. 20, p. 3986, 1999.

[87] B. C. Barnes, D. W. Siderius, and L. D. Gelb *Langmuir*, vol. 25, no. 12, pp. 6702–6716, 2009.

[88] A. A. Díaz-Sánchez, A. de Candia, and A. Coniglio *J. Phys. A*, vol. 35, no. 15, pp. 3359–3368, 2002.

[89] A. Ghosh and D. Dhar *Europhys. Lett.*, vol. 78, no. 2, p. 20003, 2007.

[90] J. Kundu, R. Rajesh, D. Dhar, and J. F. Stilck *Phys. Rev. E*, vol. 87, no. 3, p. 032103, 2013.

[91] D. Ruth, R. Toral, D. Holz, J. Rickman, and J. Gunton *Thin Solid Films*, vol. 597, pp. 188–192, 2015.

[92] K. Ramola, K. Damle, and D. Dhar *Phys. Rev. Lett.*, vol. 114, no. 19, p. 190601, 2015.

[93] J. Kirkwood, R. Smoluchowski, J. Mayer, and W. Weyl, *Phase Transformations in Solids*, p. 6. Wiley, New York, 1951.

[94] R. Peierls *Ann. Inst. Henri Poincaré*, vol. 5, no. 3, pp. 177–222, 1935.

[95] N. D. Mermin and H. Wagner *Phys. Rev. Lett.*, vol. 17, no. 22, pp. 1133–1136, 1966.

[96] J. M. Kosterlitz and D. J. Thouless *J. Phys. C*, vol. 6, no. 7, pp. 1181–1203, 1973.

[97] D. R. Nelson and B. I. Halperin *Phys. Rev. B*, vol. 19, no. 5, pp. 2457–2484, 1979.

[98] A. P. Young *Phys. Rev. B*, vol. 19, no. 4, pp. 1855–1866, 1979.

[99] K. Wierschem and E. Manousakis *Phys. Rev. B*, vol. 83, no. 21, p. 214108, 2011.

[100] W. Qi, A. P. Gantapara, and M. Dijkstra *Soft Matter*, vol. 10, no. 30, pp. 5449–5457, 2014.

[101] S. C. Kapfer and W. Krauth *Phys. Rev. Lett.*, vol. 114, no. 3, p. 035702, 2015.

[102] D. E. Dudalov, E. N. Tsiok, Y. D. Fomin, and V. N. Ryzhov

[103] U. Gasser, C. Eisenmann, G. Maret, and P. Keim *ChemPhysChem*, vol. 11, no. 5, pp. 963–970, 2010.

[104] C. Domb *Il Nuovo Cimento (1955-1965)*, vol. 9, pp. 9–26, 1958.

[105] D. M. Burley *Proc. Phys. Soc.*, vol. 75, no. 2, pp. 262–274, 1960.

[106] D. Burley *Proc. Phys. Soc.*, vol. 77, no. 2, pp. 451–458, 1961.

[107] J. Amar, K. Kaski, and J. D. Gunton *Phys. Rev. B*, vol. 29, no. 3, pp. 1462–1464, 1984.

[108] K. Binder and D. P. Landau *Phys. Rev. B*, vol. 21, no. 5, pp. 1941–1962, 1980.

[109] D. P. Landau and K. Binder *Phys. Rev. B*, vol. 31, no. 9, pp. 5946–5953, 1985.

[110] O. Derzhko and J. Richter *Phys. Rev. B*, vol. 70, no. 10, p. 104415, 2004.

[111] E. Eisenberg and A. Baram *J. Phys. A*, vol. 33, no. 9, pp. 1729–1734, 2000.

[112] E. Eisenberg and A. Baram *Europhys. Lett.*, vol. 71, no. 6, p. 900, 2005.

[113] M. Weigt and A. K. Hartmann *Europhys. Lett.*, vol. 62, no. 4, p. 533, 2003.

[114] S. Ji, C. Ates, and I. Lesanovsky *Phys. Rev. Lett.*, vol. 107, no. 6, p. 060406, 2011.

[115] R. Baxter *Ann. Comb.*, vol. 3, no. 2-4, pp. 191–203, 1999.

[116] K. Georgiou, E. Kranakis, and D. Krizanc *Discrete Math.*, vol. 309, no. 16, pp. 5120 – 5129, 2009.

[117] A. D. Scott and A. D. Sokal *J. Stat. Phys.*, vol. 118, no. 5-6, pp. 1151–1261, 2005.

[118] Y. Suhov and U. Rozikov *Queueing Syst.*, vol. 46, no. 1-2, pp. 197–212, 2004.

[119] A. D. Sokal *arXiv preprint cond-mat/0004231*, 2000.

[120] N. Bhatnagar, A. Sly, and P. Tetali, "Reconstruction threshold for the hardcore model," in *Approximation, Randomization, and Combinatorial Optimization. Algorithms and Techniques*, pp. 434–447, Springer, 2010.

[121] A. Baram and M. Fixman *J. Chem. Phys.*, vol. 101, no. 4, pp. 3172–3178, 1994.

[122] L. K. Runnels *Phys. Rev. Lett.*, vol. 15, no. 14, pp. 581–584, 1965.

[123] L. K. Runnels and L. L. Combs *J. Chem. Phys.*, vol. 45, no. 7, pp. 2482–2492, 1966.

[124] F. H. Ree and D. A. Chesnut *J. Chem. Phys.*, vol. 45, no. 11, pp. 3983–4003, 1966.

[125] R. Nisbet and I. Farquhar *Physica*, vol. 76, no. 2, pp. 259 – 282, 1974.

[126] W. Guo and H. W. J. Blöte *Phys. Rev. E*, vol. 66, no. 4, p. 046140, 2002.

[127] Y. ban Chan *J. Phys. A*, vol. 45, no. 8, p. 085001, 2012.

[128] I. Jensen *J. Phys. A*, vol. 45, no. 50, p. 508001, 2012.

[129] M. Assis, J. L. Jacobsen, I. Jensen, J.-M. Maillard, and B. M. McCoy *J. Phys. A*, vol. 47, no. 44, p. 445001, 2014.

[130] R. J. Baxter, I. G. Enting, and S. K. Tsang *J. Stat. Phys.*, vol. 22, no. 4, pp. 465–489, 1980.

[131] Z. Ràcz *Phys. Rev. B*, vol. 21, no. 9, pp. 4012–4016, 1980.

[132] C.-K. Hu and C.-N. Chen *Phys. Rev. B*, vol. 43, no. 7, pp. 6184–6185, 1991.

[133] L. Lafuente and J. A. Cuesta *Phys. Rev. E*, vol. 68, no. 6, p. 066120, 2003.

[134] H. N. V. Temperley *Proc. Phys. Soc.*, vol. 80, no. 4, pp. 823–829, 1962.

[135] H. Meirovitch *J. Stat. Phys.*, vol. 30, no. 3, pp. 681–698, 1983.

[136] C.-K. Hu and K.-S. Mak *Phys. Rev. B*, vol. 39, no. 4, pp. 2948–2951, 1989.

[137] D.-J. Liu and J. W. Evans *Phys. Rev. B*, vol. 62, no. 3, pp. 2134–2145, 2000.

[138] E. Aksenenko and Y. V. Shulepov *J. Phys. A*, vol. 15, no. 8, pp. 2515–2522, 1982.

[139] W. Kinzel and M. Schick *Phys. Rev. B*, vol. 24, no. 1, pp. 324–328, 1981.

[140] A. Bellemans and R. K. Nigam *Phys. Rev. Lett.*, vol. 16, no. 23, pp. 1038–1039, 1966.

[141] F. H. Ree and D. A. Chesnut *Phys. Rev. Lett.*, vol. 18, no. 1, pp. 5–8, 1967.

[142] K. Ramola. PhD thesis, Tata Institute of Fundamental Research, Mumbai, 2012.

[143] E. Domany, M. Schick, J. S. Walker, and R. B. Griffiths *Phys. Rev. B*, vol. 18, no. 5, pp. 2209–2217, 1978.

[144] A. Bellemans and J. Orban *Phys. Rev. Lett.*, vol. 17, no. 17, pp. 908–910, 1966.

[145] J. Orban and D. Van Belle *J. Phys. A*, vol. 15, no. 9, pp. L501–L505, 1982.

[146] R. Nisbet and I. Farquhar *Physica*, vol. 76, no. 2, pp. 283 – 294, 1974.

[147] C. E. Fiore and M. G. E. da Luz *J. Chem. Phys.*, vol. 138, no. 1, p. 014105, 2013.

[148] D.-J. Liu *J. Chem. Phys.*, vol. 121, no. 9, pp. 4352–4357, 2004.

[149] P. J. Flory *Proc. R. Soc.*, vol. 234, no. 1196, pp. 73–89, 1956.

[150] R. Zwanzig *J. Chem. Phys.*, vol. 39, no. 7, pp. 1714–1721, 1963.

[151] G. J. Vroege and H. N. W. Lekkerkerker *Rep. Prog. Phys.*, vol. 55, no. 8, pp. 1241–1309, 1992.

[152] D. Frenkel, H. Lekkerkerker, and A. Stroobants *Nature*, vol. 332, no. 6167, pp. 822–823, 1988.

[153] V. L. Berezinskii *Sov. Phys. JETP*, vol. 32, no. 3, pp. 493–500, 1971.

[154] V. L. Berezinskii *Sov. Phys. JETP*, vol. 34, no. 3, pp. 610–616, 1972.

[155] J. P. Straley *Phys. Rev. A*, vol. 4, no. 2, pp. 675–681, 1971.

[156] D. Frenkel and R. Eppenga *Phys. Rev. A*, vol. 31, no. 3, pp. 1776–1787, 1985.

[157] M. D. Khandkar and M. Barma *Phys. Rev. E*, vol. 72, no. 5, p. 051717, 2005.

[158] R. L. C. Vink *Euro. Phys. J. B*, vol. 72, no. 2, pp. 225–231, 2009.

[159] V. Narayan, N. Menon, and S. Ramaswamy *J. Stat. Mech. Theor. Exp.*, vol. 2006, no. 01, p. P01005, 2006.

[160] K. Wojciechowski and D. Frenkel *Comp. Met. Sci. Technol.*, vol. 10, no. 2, pp. 235–255, 2004.

[161] L. Walsh and N. Menon *arXiv preprint arXiv:1510.00656*, 2015.

[162] J. Kundu, R. Rajesh, D. Dhar, and J. F. Stilck *AIP Conf. Proc.*, vol. 1447, no. 1, pp. 113–114, 2012.

[163] D. A. Matoz-Fernandez, D. H. Linares, and A. J. Ramirez-Pastor *Europhys. Lett*, vol. 82, no. 5, p. 50007, 2008.

[164] D. A. Matoz-Fernandez, D. H. Linares, and A. J. Ramirez-Pastor *Physica A*, vol. 387, no. 26, pp. 6513–6525, 2008.

[165] D. A. Matoz-Fernandez, D. H. Linares, and A. J. Ramirez-Pastor *J. Chem. Phys.*, vol. 128, no. 21, p. 214902, 2008.

[166] D. H. Linares, F. Romá, and A. J. Ramirez-Pastor *J. Stat. Mech. Theor. Exp.*, vol. 2008, no. 03, p. P03013, 2008.

[167] T. Fischer and R. L. C. Vink *Europhys. Lett.*, vol. 85, no. 5, p. 56003, 2009.

[168] J. Kundu, J. F. Stilck, and R. Rajesh *Europhys. Lett.*, vol. 112, no. 6, p. 66002, 2016.

[169] J. F. Stilck and R. Rajesh *Phys. Rev. E*, vol. 91, no. 1, p. 012106, 2015.

[170] D. Dhar, R. Rajesh, and J. F. Stilck *Phys. Rev. E*, vol. 84, no. 1, p. 011140, 2011.

[171] J. Kundu and R. Rajesh *Phys. Rev. E*, vol. 88, no. 1, p. 012134, 2013.

[172] C. Gruber and H. Kunz *Commun. Math. Phys.*, vol. 22, no. 2, pp. 133–161, 1971.

[173] M. Schmidt, L. Lafuente, and J. A. Cuesta *J. Phys.*, vol. 15, no. 27, pp. 4695–4708, 2003.

[174] T. Nath, J. Kundu, and R. Rajesh *J. Stat. Phys.*, vol. 160, no. 5, pp. 1173–1197, 2015.

[175] E. Edlund and M. N. Jacobi *Phys. Rev. Lett.*, vol. 105, no. 13, p. 137203, 2010.

[176] S. Jin, A. Sen, and A. W. Sandvik *Phys. Rev. Lett.*, vol. 108, no. 4, p. 045702, 2012.

[177] S. Papanikolaou, E. Luijten, and E. Fradkin *Phys. Rev. B*, vol. 76, no. 13, p. 134514, 2007.

[178] S. Wenzel, T. Coletta, S. E. Korshunov, and F. Mila *Phys. Rev. Lett.*, vol. 109, no. 18, p. 187202, 2012.

[179] T. Nath and R. Rajesh *Phys. Rev. E*, vol. 90, no. 1, p. 012120, 2014.

[180] R. Peierls *Math. Proc. Cambridge Philos. Soc.*, vol. 32, no. 03, pp. 477–481, 1936.

[181] R. Dobrushin *Funct. Anal. Appl.*, vol. 2, no. 4, pp. 302–312, 1968.

[182] J. Kundu and R. Rajesh *Euro. Phys. J. B*, vol. 88, no. 5, p. 133, 2015.

[183] A. M. Ferrenberg and R. H. Swendsen *Phys. Rev. Lett.*, vol. 61, no. 23, pp. 2635–2638, 1988.

[184] F. Smallenburg, L. Filion, M. Marechal, and M. Dijkstra *Proc. Natl. Acad. Sci.*, vol. 109, no. 44, pp. 17886–17890, 2012.

[185] S. P. Carmichael and M. S. Shell *J Chem. Phys.*, vol. 139, no. 16, p. 164705, 2013.

[186] R. J. Baxter, *Exactly Solved Models in Statistical Mechanics*. London: Academic Press, 1982.

[187] F. Wang and D. P. Landau *Phys. Rev. Lett.*, vol. 86, no. 10, p. 2050, 2001.

[188] F. Wang and D. P. Landau *Phys. Rev. E*, vol. 64, no. 5, p. 056101, 2001.

[189] R. Dickman and A. G. Cunha-Netto *Phys. Rev. E*, vol. 84, no. 2, p. 026701, 2011.

[190] R. E. Belardinelli, V. D. Pereyra, R. Dickman, and B. J. Lourenço *J. Stat. Mech. Theor. Exp.*, vol. 2014, no. 7, p. P07007, 2014.

[191] L. K. Runnels *J. Math. Phys.*, vol. 8, no. 10, pp. 2081–2087, 1967.

[192] T. Nath and R. Rajesh *J. Stat. Mech. Theor. Exp.*, no. 7, p. 073203, 2016.

[193] T. Nath, D. Dhar, and R. Rajesh *Europhys. Lett.*, vol. 114, no. 1, p. 10003, 2016.

[194] D. Ioffe, Y. Velenik, and M. Zahradnik *J. Stat. Phys.*, vol. 122, no. 4, pp. 761–786, 2006.

[195] L. Tonks *Phys. Rev.*, vol. 50, no. 10, pp. 955–963, 1936.

[196] H. Takahashi, "A simple method for treating the statistical mechanics of one-dimensional substances," in *Proc. Phys.-Math. Soc. Japan*, vol. 24, p. 60, 1942.

[197] E. Müller-Hartmann and J. Zittartz *Z. Phys. B Condens Matter*, vol. 27, no. 3, pp. 261–266, 1977.

[198] D. Abraham and P. Reed *Phys. Rev. Lett.*, vol. 33, no. 6, pp. 377–379, 1974.

[199] W. Selke and W. Pesch *Z. Phys. B Condens Matter*, vol. 47, no. 4, pp. 335–340, 1982.

[200] D. Mandal, T. Nath, and R. Rajesh *arXiv preprint arXiv:1702.02332*, 2017s.

[201] B. M. McCoy and T. T. Wu, *The two-dimensional Ising model*. Courier Corporation, 2014.